

# Atomistic modelling and simulations of magnetic transition metals



Dissertation

zur

Erlangung des Grades

Doktor-Ingenieur

der

Fakultät für Maschinenbau

der Ruhr-Universität Bochum

von

Ning Wang

aus Shandong, China

Bochum 2019

Dissertation eingereicht am: 06.11.2019  
Tag der mündlichen Prüfung: 16.12.2019  
Erster Referent: Prof. Dr. rer. nat. Ralf Drautz  
Zweiter Referent: Prof. Dr. rer. nat. Jörg Neugebauer

*“If, in some cataclysm, all of scientific knowledge were to be destroyed, and only one sentence passed on to the next generation of creatures, what statement would contain the most information in the fewest words? I believe it is the atomic hypothesis that all things are made of atoms.”*

Richard Feynman



## Acknowledgements

I am so lucky and grateful to have many interactions with five excellent scientists during my Ph.D study, Prof. Dr. Ralf Drautz, Dr. Thomas Hammerschmidt, Dr. Tilmann Hickel, Dr. Jutta Rogal, and Prof. Dr. Jörg Neugebauer. My Ph.D work could not have been done without their generous supports and help.

First of all, I would like to express my sincere gratitude to my first supervisor, Prof. Dr. Ralf Drautz, for his continuous support throughout the whole course of my Ph.D study. His attitude towards science, his patience, tolerance, and consistent encouragement for ignorant students like me, his insistence on what he believes to be right, and so on, influenced me unconsciously and has already become the treasure I will value in my remaining life. My sincere thanks to my group leader, Dr. Thomas Hammeschmidt! It was one of my most beautiful times to have worked in his group. He is the most patient and nicest person I have ever met. My special thanks to Dr. Tilmann Hickel! When I started my work, I almost knew nothing about the quantum theory of magnetism, which is unfortunately highly involved in my project. I am really grateful for Dr. Tilmann Hickel's tolerance of my ignorance and being so patient to teach me step by step. My sincere thanks to Dr. Jutta Rogal! Dr. Jutta Rogal is an expert on sampling of the high-dimensional energy surface, and it was so enjoyable to talk with her about the ideas of sampling. Besides, I would like to thank Prof. Dr. Jörg Neugebauer for being willing to be my second supervisor. He is leading a fantastic research group in which I am working now. I am grateful to have such an intelligent director with great leadership, wisdom, and deep insight into science.

I would like to thank the colleagues at ICAMS, Dr. Jingliang Wang, Dr. Grisell Díaz Leines, Dr. Yury Lysogorskiy, Dr. Matous Mrovec, Martin

Stadt, Dr. Tao Wang, and Dr. Carlos Teijeiro, and the colleagues at MPIE, Dr. Fritz Körmann, Dr. Yuji Ikeda, and Dr. Xie Zhang, for their stimulating discussions and generous supports during my Ph.D study. Besides, I want to thank the friends in the ICAMS beer session on Fridays, Dr. Miroslav Čák, Dr. Suzana G. Fries, Ashish Chauniyal, Sarath Menon, Abril Azócar Guzmán, Abhishek Biswas, Matteo Rinaldi, Denise Reimann, Maximilian Grabowski, and so on, which has become a beautiful memory in my mind.

Finally, I would like to take this opportunity to express my heartfelt gratitude to my parents, my brother and his family, and my girlfriend for their continuous love, which supports me to overcome the obstacles one by one.

# Abstract

Atomistic simulation has become an important tool to understand and predict the behavior of materials, and the last several decades have evidenced remarkable progress in this field. Although atomistic methods have been becoming more and more mature for non-magnetic materials, we are still lacking proper approaches to perform large-scale atomistic simulations of magnetic transition metals including the important industrial materials iron, nickel, and cobalt.

The atomistic simulation of magnetic transition metals requires two aspects, the atomistic modelling of microscopic interactions and finite-temperature excitations of magnetic and atomic degrees of freedom and the numerical schemes to calculate the collective behavior that determines macroscopic properties. We propose a finite-temperature magnetic tight-binding model to tackle the first obstacle (chapter 3) and develop Hamiltonian Monte Carlo algorithms to tackle the second obstacle (chapter 4). We show a benchmark test of our methods by calculating the magnon-phonon coupling in bcc iron and obtain excellent agreement between our result and experimental data (chapter 5). After that, we apply our methods to explore the effect of longitudinal spin fluctuations on the magnetic and structural phase transitions and the microscopic origin of the temperature-induced  $\alpha$  (bcc) -  $\gamma$  (fcc) -  $\delta$  (bcc) phase transitions in iron (chapter 5). We observe interesting competition between the electronic (magnetic) and vibrational contributions to the free-energy difference between bcc and fcc iron, and find that the magnon-phonon coupling plays a crucial role in fcc iron transforming back to bcc iron at 1670 K.

As a further extension of our methods, we develop in chapter 6 a machine-learning based perturbation approach to accelerate thermodynamic calculations of magnetic materials. Our preliminary test with

250 spins shows that the first-order correction together with a good machine-learning model is capable to give an accuracy of 1 meV/atom.

We believe that this work paves the way to atomistic simulations of magnetic transition metals and look forward to applications of our methods in calculations of other materials and their alloys besides iron.



## Kurzfassung

Atomistische Simulation hat sich zu einem wichtigen Instrument für das Verständnis und die Vorhersage des Verhaltens von Materialien entwickelt und die letzten Jahrzehnte haben bemerkenswerte Fortschritte in diesem Bereich gezeigt. Obwohl atomistische Methoden immer ausgereifter geworden sind für nichtmagnetische Materialien, fehlen geeignete Zugänge zu atomistischen Grovsimulationen von magnetischen Übergangsmetallen, einschließlich der industriell wichtigen Materialien Eisen, Nickel und Kobalt.

Die atomistische Simulation von magnetischen Übergangsmetallen beinhaltet zwei Aspekte: die atomistische Modellierung mikroskopischer Wechselwirkungen und die thermische Anregung von magnetischen und atomaren Freiheitsgraden, sowie die numerischen Verfahren um das kollektive Verhalten zu berechnen, das die makroskopischen Eigenschaften bestimmt. Wir schlagen ein magnetisches Tight-Binding Modell mit endlicher Temperatur vor, um das erste Hindernis zu überwinden (Kapitel 3) und entwickeln Hamilton Monte-Carlo Algorithmen um das zweite Hindernis zu überwinden (Kapitel 4). Wir zeigen einen Benchmark unserer Methoden anhand der Berechnung der Magnon-Phonon-Kopplung in bcc Eisen und erhalten exzellente Übereinstimmung mit experimentellen Daten (Kapitel 5). Anschließend wenden wir unsere Methoden an, um die Auswirkungen von longitudinalen Spinfluktuationen auf die magnetischen und strukturellen Phasenübergänge und den mikroskopischen Ursprung der temperaturabhängigen Phasenübergänge  $\alpha$  (bcc) -  $\gamma$  (fcc) -  $\delta$  (bcc) in Eisen zu untersuchen (Kapitel 5). Wir beobachten interessante Konkurrenz zwischen den elektronischen (magnetischen) und Vibrationsbeiträgen zum Unterschied der freien Energie von bcc und fcc Eisen, und da die Magnon-Phonon-Kopplung eine

Schlsselrolle fr die Umwandlung von fcc Eisen zu bcc Eisen bei 1670 K spielt.

Als Erweiterung unserer Methoden entwickeln wir in Kapitel 6 einen auf maschinellem Lernen basierende Strungsansatz zur Beschleunigung thermodynamischer Berechnungen magnetischer Materialien. Erste Rechnungen mit 250 Spins zeigen, dass die Korrektur erster Ordnung in Kombination mit einem guten maschinellen Lernmodell eine Genauigkeit von 1 meV/Atom erreichen kann.

Wir glauben, dass diese Arbeit den Weg fr atomistische Simulationen magnetischer bergangsmetalle ebnet und freuen uns auf Anwendungen von unserer Berechnungsmethoden fr andere Werkstoffe und deren Legierungen als Eisen.

# Contents

<b>1</b>	<b>Motivation</b>	<b>1</b>
<b>2</b>	<b>Theoretical background</b>	<b>4</b>
2.1	Magnetic tight binding . . . . .	4
2.1.1	Spin density-functional theory . . . . .	5
2.1.2	From SDFT to magnetic tight binding . . . . .	6
2.2	Bond-order potentials . . . . .	9
2.3	Hamiltonian Monte Carlo . . . . .	12
2.4	Free-energy calculations . . . . .	16
2.4.1	Lattice vibrations within harmonic approximation . . . . .	16
2.4.2	Thermodynamic integration . . . . .	20
2.5	Machine learning . . . . .	20
<b>3</b>	<b>Finite-temperature magnetic tight binding</b>	<b>22</b>
3.1	Introduction . . . . .	22
3.2	Methodology . . . . .	24
3.3	Transverse spin fluctuations . . . . .	28
3.4	Derivation of the quantized magnetic Hamiltonian . . . . .	29
3.5	Comparison with the constrained magnetic tight binding . . . . .	31
3.6	Summary . . . . .	33
<b>4</b>	<b>Accelerated spin-space sampling</b>	<b>35</b>
4.1	Introduction . . . . .	37
4.2	Methodology . . . . .	39
4.3	Results and Discussion . . . . .	44
4.3.1	Application to the classical Heisenberg model . . . . .	44
4.3.2	Application to electronic-structure based models . . . . .	45

4.4	Conclusion . . . . .	53
<b>5</b>	<b>Application to magnetic iron</b>	<b>55</b>
5.1	Magnetic phase transition in bcc and fcc iron . . . . .	56
5.2	Interplay between spin fluctuations and atomic vibrations . . . . .	57
5.3	Effect of longitudinal spin fluctuations . . . . .	63
5.4	$\alpha$ (bcc) - $\gamma$ (fcc) - $\delta$ (bcc) phase transitions . . . . .	72
5.5	Summary and conclusion . . . . .	83
<b>6</b>	<b>Machine learning for magnetic materials</b>	<b>85</b>
6.1	Introduction . . . . .	85
6.2	Methodology . . . . .	86
6.2.1	Neural-network potential . . . . .	86
6.2.2	Perturbation expansion . . . . .	86
6.3	Result . . . . .	91
6.4	Conclusion . . . . .	95
<b>7</b>	<b>Conclusion and outlook</b>	<b>96</b>
7.1	Conclusion . . . . .	96
7.2	Outlook . . . . .	97
	<b>Bibliography</b>	<b>99</b>

# List of Figures

1.1	The three paradigms of science: empirical, theoretical, and computational. . . . .	2
2.1	A schematic diagram for artificial neural networks . . . . .	21
2.2	The basic element of artificial neural networks . . . . .	21
4.1	Magnetization-energy plot for spin configurations of a $6 \times 6 \times 6$ simple cubic lattice at different temperatures. The classical ferromagnetic Heisenberg model is employed in this test. $T_C$ is its Curie temperature. The exchange parameter $J$ is chosen to be 1 eV. . . . .	43
4.2	Evolution of the magnetization of a $6 \times 6 \times 6$ simple cubic lattice for the classical Heisenberg model in the warm-up phase. Orange line: the initial state is the ferromagnetic ground state and the temperature is $2 T_C$ . Blue line: the initial state is a random-spin state and the temperature is $0.1 T_C$ . . . . .	45
4.3	Log-log plot of the relaxation time for the magnetization in units of gradient calls. $L$ represents the side length of the cubic simulation cell and $\tau$ represents the relaxation time. The error bars of the relaxation time are smaller than the symbol size. The classical Heisenberg model on the simple cubic lattice is used here. . . . .	46
4.4	Root-mean-squared (RMS) error of the spin-cluster expansion model plotted as a function of neighbour shells for pair-wise and three-spin interactions. The RMS error per cell is in the unit of $k_B T_C$ , where $T_C$ is the experimental Curie temperature of iron (1043 K). The spin-cluster expansion model is fitted for the potential energy of a magnetic BOP for $5 \times 5 \times 5$ bcc lattice of iron. . . . .	47

4.5	Average acceptance probability in the warm-up and the sampling phases. The temperature-independent spin cluster expansion is used in the warm-up phase while the temperature-dependent one used in the sampling phase. The magnetic BOP of iron is the target model in this test, with $5 \times 5 \times 5$ bcc lattice of 250 spins. . . . .	48
4.6	Binning analysis for potential energies of $5 \times 5 \times 5$ bcc lattice at different temperatures. . . . .	49
4.7	Running errors in the estimation of thermal averages of potential energies at different temperatures. . . . .	50
4.8	Thermal-average potential energy as a function of temperature for $5 \times 5 \times 5$ bcc lattice of iron obtained with a magnetic bond-order potential. . . . .	51
4.9	Magnetization as a function of temperature for $5 \times 5 \times 5$ bcc lattice of iron obtained with a magnetic bond-order potential. The images are snapshots of spin configurations at 500 K, 1200 K, and 2000 K, respectively, which are generated with the code V_sim [2]. The spin directions are indicated by the arrows and the coloration. We see the collapse of the long- and short-range magnetic orders with increasing temperatures. . . . .	52
4.10	Magnetic contribution to the specific heat as a function of temperatures for $5 \times 5 \times 5$ bcc lattice of iron for magnetic bond-order potentials. . . . .	53
5.1	Order parameter of bcc and fcc iron plotted as function of temperature. The bcc supercell contains 250 atoms, and the fcc supercell contains 300 atoms. . . . .	56
5.2	Calculated phonon spectra of fcc iron in the ferromagnetic state (dashed line) and at the magnetic temperature of 1573 K (full line). Dots: experimental phonons at 1573 K from Neuhaus et al. [100] .	59
5.3	Calculated phonon spectra of bcc iron at magnetic temperatures of 773 K, 1043 K, 1173 K and 1743 K, respectively. Lines: calculated results in this work. Dots: experimental data from Neuhaus et al. [100]. . . . .	60
5.4	Calculated force constants for the first and second neighbours as function of magnetic temperature. . . . .	61

5.5	Calculated magnetization as function of temperatures. Orange dots: magnetization of a perfect $5 \times 5 \times 5$ bcc supercell of iron with atomic positions fixed. Blue dots: atomic vibrations are included in the $5 \times 5 \times 5$ bcc supercell of iron. . . . .	63
5.6	The schematic pressure-temperature phase diagram of pure iron taken from [81] and reused under the license number RNP/19/OCT/019548. . . . .	64
5.7	Average potential energy plotted as function of temperature. . . . .	65
5.8	Magnetization plotted as function of temperature. . . . .	66
5.9	Histogram of magnitudes of atomic magnetic moments at 100 K and 1300 K. . . . .	67
5.10	Unit cells of the body-centered tetragonal (bct), body-centered cubic (bcc) and face-centered cubic (fcc) lattices . . . . .	68
5.11	Magnetic free-energy profiles along bain transformation at different temperature. . . . .	69
5.12	The magnetic free-energy difference of bcc and fcc iron as a function of temperature. . . . .	70
5.13	Magnetic free-energy barrier as a function of temperature. . . . .	71
5.14	Calculated electronic free-energy difference between $\alpha$ (bcc) and $\gamma$ (fcc) iron. . . . .	75
5.15	The two-dimensional histograms of electronic density of states of bcc and fcc iron at different magnetic temperatures. 1000 magnetic configurations are employed at each temperature. . . . .	76
5.16	Calculated vibrational-entropy difference between fcc and bcc phases of iron as function of temperature. . . . .	77
5.17	Calculated vibrational free-energy difference between fcc and bcc phases of iron as function of temperature. . . . .	78
5.18	Phonon density of states (DOS) of bcc and fcc iron at finite magnetic temperature. The shaded area indicates the gain of low-frequency (less than 4 THz) phonon modes from 300 K to 1700 K. . . . .	79
5.19	Phonon density of states (DOS) of bcc and fcc iron at magnetic temperature of 300 K and 1700 K. The green (red) shaded region indicates low-frequency (less than 4 THz) phonon modes at which fcc iron has higher (lower) phonon DOS. . . . .	80

5.20	The electronic, vibrational and total free-energy differences between bcc and fcc iron plotted as function of temperature (shown as colored dots) in comparison with CALPHAD data [1] (shown as black line). . . . .	81
5.21	The zoomed plot of the grey box in Fig. 5.20. . . . .	83
6.1	Neural-network architecture. Input layer: spin orientations of all atoms. Output layer: total energy as a sum of atomic energies. . .	87
6.2	Errors between the training and predicted potential energies of the samples in the training data set. . . . .	92
6.3	Running average of the correction terms in the second-order approximation for the thermal average of potential energy at 500 K, 900 K, 1200 K, and 1600 K. $\langle \Delta E \rangle_{\text{MLM}}$ and $\text{cov}(E_{\text{MLM}}, \chi)$ are the two first-order correction terms. The second-order correction terms are grouped into $\Delta_{\text{corr}}^{(2)}$ . . . . .	93
6.4	Error of thermal-average potential energies at different temperatures for the zeroth-order, first-order, and second-order approximation. . . . .	94
6.5	Running average of the first-order and second-order correction terms for the free-energy difference between MSM and ELM. . . . .	95



# Chapter 1

## Motivation

Computational science has become an important paradigm of materials science, as shown in Fig. 1.1. The first paradigm of materials science was based on empirical observations and trial-and-error experiments, and the Chinese blue and white pottery is a good example of the achievements in this period. After that, the paradigm of theoretical materials science came, which is labelled by physical laws described in the mathematical language. A good example is Boltzmann's equation for entropy  $S = k_B \ln \Omega$ , where  $k_B$  is the Boltzmann constant and  $\Omega$  is the number of microstates. In around 1940s, the paradigm of computational materials science appeared with the advent of fast computers, which makes it possible to understand and predict materials properties without lengthy and expensive lab experiments. One of the representative works of this period is the density-functional theory (DFT) [59, 67], and with it many new materials have been found first in computers and then in labs. The third paradigm is still a fast-growing field and many open problems need to be resolved.

At the atomic and electronic level, the computer simulation of materials requires two aspects, the mathematical modelling of interactions between particles, i.e., structure-energy relationship, and the simulation of collective behaviors of these particles, which determines the materials properties at the macroscopic scale. To tackle the first problem, empirical and analytical models have been developed, which may be as simple as the Lennard-Jones potential or as complex as DFT. To tackle the second problem, many numerical methods have been developed, e.g., classical Markov chain Monte Carlo, molecular dynamics, and quantum Monte Carlo. These methods have been becoming more and more mature for non-magnetic materials. However, for magnetic materials especially magnetic transi-

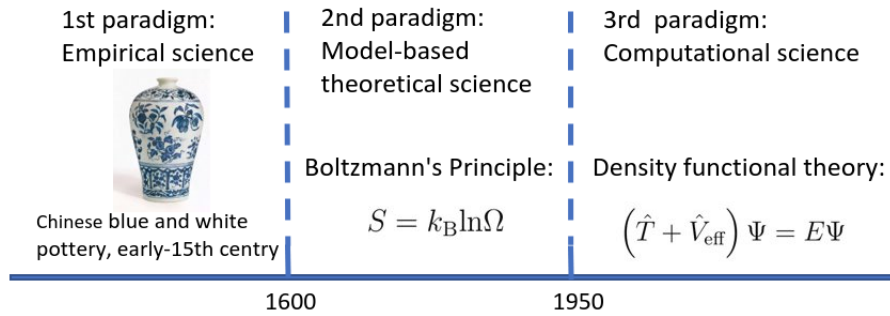


Figure 1.1: The three paradigms of science: empirical, theoretical, and computational.

tion metals, the computer simulation still faces big obstacles. As to the modelling aspect, it is more complex to model the interactions in magnetic materials than in non-magnetic materials as the magnetic interactions and the coupling between the magnetic and atomic DOFs should be described properly. For magnetic transition metals, it is even more complex as the atomic magnetic moments are not localized and the magnetic interactions can not be well described by simple models such as the Heisenberg model [94]. This also leads to complicated couplings between magnetic and atomic DOFs [51, 73, 83]. As a key characteristic, the longitudinal spin fluctuations play an important role in magnetic transition metals [28]. As to the aspect of simulations of collective behaviors, we can not employ directly the numerical methods developed for non-magnetic materials to magnetic materials as magnetic DOFs are involved. The sampling of the spin space encounters critical slowing down as a second-order magnetic phase transition exists. The Hamiltonians for magnetic interactions in magnetic transition metals are usually computationally expensive as the electronic structure is involved, which puts more challenge in the corresponding simulations. In summary, for magnetic transition metals, we still lack a consistent and computationally affordable model to describe the atomic, magnetic, and mutual interactions, and a numerical method that is efficient enough to explore the collective behaviors. The two problems are the motivation for the work in chapter 3 and 4.

The two problems we listed in the last paragraph are not only interesting and challenging from the scientific point of view, but also of significant industrial importance. As a good example, iron and steel are the most widely-used magnetic

transition metals, and their manufacturing process heavily relies on controlling the formation of the microstructure due to phase transformations. This is the motivation for the work in chapter 5 where we apply our methods to investigate phase transformations in magnetic iron.

The last issue we want to explore in this thesis is to develop a machine learning-based approach to accelerate thermodynamic calculations based on complex magnetic Hamiltonians. Both computational materials science and machine learning are based on statistics, and this intrinsic correlation leads us to apply the machine-learning methods to solve the challenging problems in computational materials science. We put our idea and some preliminary tests in chapter 6 and further work needs to be done in the future.

We summarize the four issues that we want to explore in this thesis.

- The modelling of microscopic interactions in magnetic transition metals. We aim to obtain in chapter 3 a tight-binding model that can describe properly the microscopic interactions of atomic and magnetic degrees of freedom (DFT) and is affordable for the state-of-the-art computational resources to solve.
- The efficient Monte Carlo samplers for extracting thermodynamic properties of magnetic transition metals from a microscopic model. We aim to obtain in chapter 4 efficient sampling algorithms that work for transverse and longitudinal magnetic DOFs.
- The benchmark test of our methods and the new insight into phase transitions of iron. In chapter 5, we first calculate the magnon-phonon coupling in iron as a benchmark test of our methods and then show our insight into longitudinal spin fluctuations and  $\alpha$  (bcc) -  $\gamma$  (fcc) -  $\delta$  (bcc) phase transitions in iron.
- A machine learning-based approach to accelerate thermodynamic calculations with complex magnetic Hamiltonians, which is put in chapter 6.

# Chapter 2

## Theoretical background

We present in this chapter the fundamental theories needed for this thesis. We first give a brief summary of magnetic tight binding and point out that it works as a magnetic ground-state theory and cannot be used straightforwardly for thermodynamic calculations of magnets. This model should be recovered at the magnetic-ground state by the finite-temperature model that we propose in chapter 3. After that, we give a brief introduction to a linear-scaling electronic-structure method, the bond-order potentials [32, 33]. As our work in chapter 4 is based on Hamiltonian Monte Carlo, we give a discussion of it in section 2.3. We review in section 2.4 the phonon theory within the harmonic approximation and the thermodynamic integration as we need them for thermodynamic calculations in chapter 5. The last section of this chapter is devoted to an introduction to machine learning, which we need for the work in chapter 6.

### 2.1 Magnetic tight binding

As pointed out by Finnis [39], there is no unique tight-binding theory as different approximations might be involved. We discuss two magnetic tight binding models in this section, the one of Paxton and Finnis [102] for collinear magnetism and the one of Drautz and Pettifor [33] for non-collinear magnetism. Both models can be obtained by coarse-graining from spin-density-functional theory.

### 2.1.1 Spin density-functional theory

We neglect relativistic effects in the discussion of spin-density-functional theory (SDFT) [59, 67, 130]. The effective one-particle eigenstate  $\psi_n(\mathbf{r})$  consists of two components

$$\boldsymbol{\psi}_n(\mathbf{r}) = \begin{pmatrix} \psi_{n\uparrow}(\mathbf{r}) \\ \psi_{n\downarrow}(\mathbf{r}) \end{pmatrix}. \quad (2.1)$$

The spin density  $\boldsymbol{\rho}(\mathbf{r})$  is a  $2 \times 2$  matrix and computed from eigenfunctions

$$\rho_{\mu\nu}(\mathbf{r}) = \sum_n^{\text{occ}} \psi_{n\mu}^*(\mathbf{r}) \psi_{n\nu}(\mathbf{r}). \quad (2.2)$$

The spin-density matrix can be decomposed as a charge density  $n(\mathbf{r})$  and a magnetization density  $\mathbf{m}(\mathbf{r})$ , which can be obtained from the eigenfunctions according to

$$n(\mathbf{r}) = \sum_n^{\text{occ}} \boldsymbol{\psi}_n^\dagger(\mathbf{r}) \mathbf{I} \boldsymbol{\psi}_n(\mathbf{r}), \quad (2.3)$$

and

$$m_\alpha(\mathbf{r}) = \sum_n^{\text{occ}} \boldsymbol{\psi}_n^\dagger(\mathbf{r}) \boldsymbol{\sigma}_\alpha \boldsymbol{\psi}_n(\mathbf{r}), \quad (2.4)$$

where  $\boldsymbol{\sigma}_\alpha$  are Pauli matrices.

The single-electron effective Hamiltonian is given as

$$\mathcal{H}_{\text{SDFT}} = -\frac{\hbar^2}{2m} \Delta + \mathbf{W}_{\text{eff}}(\mathbf{r}) \quad (2.5)$$

where the effective potential matrix is given as

$$\mathbf{W}_{\text{eff}}(\mathbf{r}) = V_{\text{H}}(\mathbf{r})\mathbf{I} + \mathbf{W}_{\text{XC}}(\mathbf{r}) + \mathbf{W}_{\text{ext}}(\mathbf{r}). \quad (2.6)$$

The total energy is given as

$$U[\boldsymbol{\rho}] = \sum_\mu \sum_n^{\text{occ}} \langle \psi_{n\mu} | -\frac{\hbar^2}{2m} | \psi_{n\mu} \rangle + U_{\text{H}}[n] + U_{\text{XC}}[\boldsymbol{\rho}] + U_{\text{ext}} + U_{\text{nuc}}. \quad (2.7)$$

$U_{\text{H}}[n]$  is the Hartree energy which only depends on the charge density  $n(\mathbf{r})$ , and  $U_{\text{XC}}[\boldsymbol{\rho}]$  is the exchange-correlation energy which depends on both the charge density  $n(\mathbf{r})$  and the magnetization density  $\mathbf{m}(\mathbf{r})$ .

In the local-spin-density approximation, the exchange-correlation energy is defined by [57]

$$U_{\text{XC}}[\boldsymbol{\rho}] = \int n(\mathbf{r}) \epsilon_{\text{xc}}[n(\mathbf{r}), |\mathbf{m}(\mathbf{r})|] d\mathbf{r}, \quad (2.8)$$

where the energy density  $\epsilon_{\text{xc}}$  may be parametrized with the local-density approximation (LDA) or the generalized gradient approximation (GGA).

The exchange-correlation potential  $\mathbf{W}_{\text{XC}}(\mathbf{r})$  corresponding to Eq. 2.8 is a  $2 \times 2$  matrix given by [57]

$$\mathbf{W}_{\text{XC}}(\mathbf{r}) = v_{\text{xc}}[\boldsymbol{\rho}](\mathbf{r}) \mathbf{I} + \mathbf{b}_{\text{xc}}[\boldsymbol{\rho}](\mathbf{r}) \cdot \boldsymbol{\sigma} \quad (2.9)$$

where  $\boldsymbol{\sigma}$  is a three-dimensional vector formed by the Pauli matrices. The exchange-correlation field  $\mathbf{b}_{\text{xc}}[\boldsymbol{\rho}](\mathbf{r})$  is parallel to the magnetization  $\mathbf{m}(\mathbf{r})$  in the local-spin-density approximation.

### 2.1.2 From SDFT to magnetic tight binding

In this subsection, we aim at giving a brief summary of the coarse-graining procedure from SDFT to magnetic tight binding. We base our discussion on an orthogonal basis set of atomic orbitals  $\{|i\alpha\mu\rangle\}$ , where we use  $i$  to label atomic sites,  $\alpha$  to label orbitals, and  $\mu$  to label electron spins. We follow the convention in the last subsection and use  $\psi_n$  to denote the eigenstates. The element of the spin-density matrix in tight binding is given as

$$\rho_{i\alpha\mu, j\beta\nu} = \sum_{\xi} \sum_n^{\text{occ}} \langle i\alpha\mu | \psi_{n\xi} \rangle \langle \psi_{n\xi} | j\beta\nu \rangle, \quad (2.10)$$

where we introduce new symbols  $\xi$  and  $\nu$  to label electron spins,  $j$  to label atomic sites, and  $\beta$  to label orbitals. One crucial step from SDFT to magnetic tight binding is the second-order expansion of the exchange-correlation energy  $U_{\text{XC}}[\boldsymbol{\rho}]$ . As shown by Drautz and Pettifor [33], the second-order approximation that is invariant with respect to the spin rotation and contains no gradient terms is given by

$$U_{\text{XC}}^2[\boldsymbol{\rho}] = \int K^{\text{XC}}(\mathbf{r}) n(\mathbf{r}) d\mathbf{r} + \frac{1}{2} \int \int J^{\text{XC}}(\mathbf{r}, \mathbf{r}') n(\mathbf{r}) n(\mathbf{r}') d\mathbf{r} d\mathbf{r}' - \frac{1}{4} \int \int I^{\text{XC}}(\mathbf{r}, \mathbf{r}') \mathbf{m}(\mathbf{r}) \mathbf{m}(\mathbf{r}') d\mathbf{r} d\mathbf{r}'. \quad (2.11)$$

In tight binding, as we work with local atomic orbitals, it is more convenient to further approximate the exchange-correlation energy as a function of atomic charge  $n_i$  and magnetic moment  $\mathbf{m}_i$ , which are defined as

$$\begin{aligned} n_i &= \sum_{\alpha} \sum_{\mu} \rho_{i\alpha\mu, i\alpha\mu}, \\ \mathbf{m}_i &= \sum_{\alpha} \sum_{\mu} \sum_{\nu} \rho_{i\alpha\mu, i\alpha\nu} \boldsymbol{\sigma}_{\mu\nu}. \end{aligned} \quad (2.12)$$

If we only consider onsite electron-electron interactions, the exchange-correlation energy can be further approximated as

$$U_{\text{XC}}^2 = \sum_i K_i^{\text{XC}} n_i + \frac{1}{2} \sum_i J_i^{\text{XC}} n_i^2 - \frac{1}{4} \sum_i I_i^{\text{XC}} \mathbf{m}_i^2. \quad (2.13)$$

We first leave the coefficient of the first-order term aside and give a discussion of coefficients of the second-order terms. Intuitively,  $J_i^{\text{XC}}$  and  $I_i^{\text{XC}}$  measure the strength of onsite Coulomb and exchange interactions of electrons and seem to have similar meaning with those of the Hubbard parameter  $U_i$  and the (Hund's-rule) exchange parameter  $J_i$ . Actually, their relationship for collinear magnetism has already been discussed by Paxton and Finnis [102] based on the interpretation of the Hubbard parameter and the exchange parameter

$$\begin{aligned} \frac{\partial}{\partial \rho_{i\downarrow}} \frac{\partial U_{\text{XC}}^2}{\partial \rho_{i\uparrow}} &= \frac{\partial}{\partial \rho_{i\uparrow}} \frac{\partial U_{\text{XC}}^2}{\partial \rho_{i\downarrow}} \equiv U_i, \\ \frac{\partial}{\partial \rho_{i\downarrow}} \frac{\partial U_{\text{XC}}^2}{\partial \rho_{i\downarrow}} &= \frac{\partial}{\partial \rho_{i\uparrow}} \frac{\partial U_{\text{XC}}^2}{\partial \rho_{i\uparrow}} \equiv U_i - J_i, \end{aligned} \quad (2.14)$$

and  $J_i^{\text{XC}}$  and  $I_i^{\text{XC}}$  can be simply expressed in terms of  $U_i$  and  $J_i$ ,

$$\begin{aligned} J_i^{\text{XC}} &= U_i - \frac{1}{2} J_i, \\ I_i^{\text{XC}} &= J_i. \end{aligned} \quad (2.15)$$

The two relations Eq. 2.15 also hold for non-collinear magnetism within local-spin-density approximation (LSDA) simply because the exchange-correlation field is parallel to the direction of the local magnetization and the exchange parameter  $I_i^{\text{XC}}$  is a scalar. We next replace  $J_i^{\text{XC}}$  and  $I_i^{\text{XC}}$  by  $\bar{U}_i$  and  $J_i$  in the remaining of this thesis in order to follow the general convention.

The next step from SDFT to magnetic tight binding is to expand the total energy with respect to a non-spin-polarized reference density [33]

$$U_{\text{pot}} = \sum_{i\alpha j\beta} H_{i\alpha,j\beta}^{(0)} \sum_{\mu} \rho_{i\alpha\mu,j\beta\mu} + \frac{1}{2} \sum_i \bar{U}_i q_i^2 - \frac{1}{4} \sum_i J_i \mathbf{m}_i^2 - \frac{1}{2} \sum_i \bar{U}_i \left[ N_i^{(0)} \right]^2 \quad (2.16)$$

The second term in Eq. (2.18) is a quadratic function of the atomic charge  $q_i$  instead of  $n_i$  in Eq. (2.11) due to the expansion w.r.t. the reference density.  $N_i^{(0)}$  is the number of electrons of atom  $i$  corresponding to the reference charge density.  $H_{i\alpha,j\beta}^{(0)}$  in Eq. (2.18) is the Hamiltonian-matrix element for the reference density, and intuitively, the offsite term describes the hopping of electrons between orbital  $\alpha$  of atom  $i$  and orbital  $\beta$  of atom  $j$  in the potential of the reference charge density. We rephrase the offsite term  $H_{i\alpha,j\beta}^{(0)}$  as the hopping integral  $t_{i\alpha,j\beta}$  and the onsite term  $H_{i\alpha}^{(0)}$  as the reference onsite level  $E_{i\alpha}^{(0)}$  and introduce the bond charge  $n_{i\alpha,j\beta}$  between atomic orbital  $\alpha$  of atom  $i$  and atomic orbital  $\beta$  of atom  $j$ , which is defined as

$$n_{i\alpha,j\beta} = \sum_{\mu} \rho_{i\alpha\mu,j\beta\mu}, \quad (2.17)$$

and the potential energy can be rewritten as

$$U_{\text{pot}} = \sum_{i\alpha j\beta, i\alpha \neq j\beta} t_{i\alpha,j\beta} n_{i\alpha,j\beta} + \sum_{i\alpha} E_{i\alpha}^{(0)} n_{i\alpha} + \frac{1}{2} \sum_i \bar{U}_i q_i^2 - \frac{1}{4} \sum_i J_i \mathbf{m}_i^2 - \frac{1}{2} \sum_i \bar{U}_i \left[ N_i^{(0)} \right]^2. \quad (2.18)$$

We next introduce the two key approximations in tight binding.

- The two-center approximation for the hopping integral [116],
- the pair-wise approximation for the remaining contributions to the total energy.

With the first approximation, the hopping integral  $t_{i\alpha,j\beta}$  can be parametrized as a function of distance between atom  $i$  and  $j$ ,  $t_{i,\alpha,j\beta}(|\mathbf{r}_i - \mathbf{r}_j|)$ . With the second approximation, a pair-wise function of atomic distance  $E_{\text{pair}}(\{\mathbf{r}_i\})$  is added into Eq. (2.18) to account for all the remaining contributions such as the ion-ion interactions and so on. As the last term in Eq. (2.18) contributes a constant energy shift, it can be grouped into  $E_{\text{pair}}(\{\mathbf{r}_i\})$  without losing any consistency. We finally obtain



the total energy in magnetic tight binding,

$$\begin{aligned}
U_{\text{pot}}(\{\mathbf{r}_i\}) = & \sum_{i\alpha j\beta, i\alpha \neq j\beta} t_{i\alpha, j\beta}(|\mathbf{r}_i - \mathbf{r}_j|) n_{i\alpha, j\beta} + \sum_{i\alpha} E_{i\alpha}^{(0)} n_{i\alpha} \\
& + \frac{1}{2} \sum_i \bar{U}_i q_i^2 - \frac{1}{4} \sum_i J_i \mathbf{m}_i^2 + E_{\text{pair}}(\{\mathbf{r}_i\}).
\end{aligned} \tag{2.19}$$

In Eq. (2.18), we write the potential energy in magnetic tight binding as a function of atomic positions. At first glance, it seems that the potential energy is also a function of atomic magnetic moments  $\mathbf{m}_i$  and atomic charges  $q_i$ . This observation is actually not true because  $\mathbf{m}_i$  and  $q_i$  are not free variables and should be determined in a self-consistent manner, as will be shown later. Fundamentally, it indicates that the magnetic tight binding is coarse-grained from SDFT which is a ground-state theory for non-collinear magnetism.

We next derive the single-electron effective Hamiltonian matrix and the self-consistency criterions from Eq. (2.19). The derivative of the total energy Eq. (2.19) with respect to the spin-density matrix gives the the Hamiltonian matrix

$$\begin{aligned}
H_{i\alpha\mu, j\beta\nu} = & \frac{\partial U_{\text{pot}}}{\rho_{i\alpha\mu, j\beta\nu}} \\
= & t_{i\alpha, j\beta} \delta_{\mu\nu} + \left( E_{i\alpha}^{(0)} + \bar{U}_i q_i \delta_{\mu\nu} - \frac{1}{2} J_i \mathbf{m}_i \boldsymbol{\sigma}_{\mu\nu} \right) \delta_{ij} \delta_{\alpha\beta}.
\end{aligned} \tag{2.20}$$

As the Hamiltonian matrix Eq. (2.20) depends on the atomic charge  $q_i$  and the atomic magnetic moment  $\mathbf{m}_i$  which in turn depends on the Hamiltonian matrix, this model should be solved in a self-consistent manner. The self-consistency criterions are given by the onsite elements of the Hamiltonian matrix

$$E_{i\alpha\mu\nu} = E_{i\alpha\mu\nu}^{(0)} + \bar{U}_i q_i \delta_{\mu\nu} - \frac{1}{2} J_i \mathbf{m}_i \boldsymbol{\sigma}_{\mu\nu}, \tag{2.21}$$

which are denoted as the onsite-level matrix in literature.

## 2.2 Bond-order potentials

The tight-binding model can be directly solved by diagonalizing the Hamiltonian matrix. However, the diagonalization method has a cubic scaling of computational cost with the number of atoms, which restricts its application to simulations of

medium-size supercells only. The bond-order potentials [32, 33] bypass the diagonalization by employing the moments theorem [27] to coarse-grain the local density of states. This method is linear-scaling with the number of atoms and has the potential to go to large-scale simulations. To illustrate how bond-order potentials work, we take the approximate evaluation of the band energy as an example. The other terms in the potential energy might be approximated in a similar way, and more details of the formalism can be found in [31–33].

We first introduce the onsite-representation of the band energy [32]

$$\begin{aligned} U_{\text{band}} &= \sum_{i\alpha\nu} \int^{E_{\text{F}}} E n_{i\alpha\nu}(E) dE, \\ &= \sum_{i\alpha\nu} \int^{\epsilon_{\text{F}}} \left( 2b_{i\alpha\nu}^{(\infty)} \cdot \epsilon + a_{i\alpha\nu}^{(\infty)} \right) n_{i\alpha\nu}(\epsilon) d\epsilon, \end{aligned} \quad (2.22)$$

where  $n_{i\alpha\nu}(E)$  is the local density of states for the spin- $\nu$  channel at orbital  $\alpha$  and atom  $i$ . We introduced from the first to the second line on the right-hand side of Eq. (2.22) the scaled energy  $\epsilon$  defined as

$$\epsilon = \frac{E - a_{i\alpha\nu}^{(\infty)}}{2b_{i\alpha\nu}^{(\infty)}}, \quad (2.23)$$

where  $a_{i\alpha\nu}^{(\infty)}$  and  $b_{i\alpha\nu}^{(\infty)}$  are the recursion coefficients at the infinite recursion level and defined by the terminators in practice [32].

We see in Eq. (2.22) that the local density of states contains sufficient information to evaluate the band energy. In the conventional approach, the local density of states is obtained by diagonalizing the Hamiltonian matrix. In bond-order potentials, it is evaluated approximately based on the moments theorem with the moments defined as

$$\begin{aligned} \mu_{i\alpha\nu}^{(n)} &= \int E^n n_{i\alpha\nu}(E) dE, \\ \hat{\mu}_{i\alpha\nu}^{(n)} &= \int \epsilon^n n_{i\alpha\nu}(\epsilon) d\epsilon. \end{aligned} \quad (2.24)$$

The moments represent the geometric feature of the local density of states. For example, the first moment  $\mu_{i\alpha\nu}^{(1)}$  measures the center of gravity of the local density of states  $n_{i\alpha\nu}(E)$ , the second moment  $\mu_{i\alpha\nu}^{(2)}$  defines its mean square width, the third moment  $\mu_{i\alpha\nu}^{(3)}$  its skewness, and the fourth moment  $\mu_{i\alpha\nu}^{(4)}$  its bimodality. We may exactly reconstruct the local density of states if we know all its moments. The

reconstruction method adapted in bond-order potentials is based on the Chebyshev polynomials of the second kind and given as [32]

$$n_{i\alpha\nu}(\epsilon) = \frac{2}{\pi} \sqrt{1 - \epsilon^2} \sum_{m=0}^{\infty} \sum_{n=0}^m p_{mn} \hat{\mu}_{i\alpha\nu}^{(n)} P_m(\epsilon). \quad (2.25)$$

where  $P_m(\epsilon) = \sum_{n=0}^m p_{mn} \epsilon^n$  is the Chebyshev polynomial. If we include all Chebyshev polynomials by taking  $m$  to infinity, the local density of states is reconstructed exactly. In practice, we terminate the polynomial expansion to a finite  $n_{\max}$  and represent the local density of states approximately,

$$\begin{aligned} n_{i\alpha\nu}(\epsilon) &\approx n_{i\alpha\nu}^{(n_{\max})}(\epsilon) \\ &= \frac{2}{\pi} \sqrt{1 - \epsilon^2} \sum_{m=0}^{n_{\max}} \sum_{n=0}^m p_{mn} \hat{\mu}_{i\alpha\nu}^{(n)} P_m(\epsilon). \end{aligned} \quad (2.26)$$

We expect that the termination converges at a reasonable order as the low-order terms constitute the main contribution to the local density of states. 4, 9, or 12 moments are frequently used in literature [21, 22, 32, 33, 42, 44].

We have already shown in Eq. (2.26) and Eq. (2.22) that we may approximately evaluate the local density of states and the band energy once we know the moments. However, the definition of the moments Eq. (2.24) depends on the local density of states and cannot be used to evaluate them. One crucial step towards bond-order potentials is the observation that these moments may be evaluated with the self-returning hopping paths instead of using the definition Eq. (2.24) explicitly,

$$\hat{\mu}_{i\alpha\nu} = \frac{1}{(2b_{i\alpha\nu}^{(\infty)})^n} \sum_{l=0}^n \binom{n}{l} (-1)^l (a_{i\alpha\nu}^{(\infty)})^l \mu_{i\alpha\nu}^{(n-l)}, \quad (2.27)$$

with

$$\begin{aligned} \mu_{i\alpha\nu}^{(n)} &= \sum_{i_1\alpha_1\nu_1 i_2\alpha_2\nu_2, \dots, i_{n-1}\alpha_{n-1}\nu_{n-1}} \langle i\alpha\nu | \hat{\mathcal{H}} | i_1\alpha_1\nu_1 \rangle \langle i_1\alpha_1\nu_1 | \hat{\mathcal{H}} | i_2\alpha_2\nu_2 \rangle \\ &\quad \cdot \dots \langle i_{n-1}\alpha_{n-1}\nu_{n-1} | \hat{\mathcal{H}} | i\alpha\nu \rangle. \end{aligned} \quad (2.28)$$

in which each term  $\langle i_1\alpha_1\nu_1 | \hat{\mathcal{H}} | i_2\alpha_2\nu_2 \rangle$  connects two spin channels of the same or neighbouring atoms. The self-returning paths explore the local atomic environment, and their maximum length defines the cutoff of the local atomic neighbourhood included to recover the local density of states. By choosing a suitable cutoff,

we obtain a linear-scaling method to solve the tight binding model with a reasonable accuracy. We use the magnetic bond-order potential of iron [95] to test the Monte Carlo algorithm in Chapter 4 and to generate training data for neural networks in Chapter 6.

## 2.3 Hamiltonian Monte Carlo

In the last section, we showed how to construct mutual atomic interactions in magnetic materials using quantum mechanics. These models describe materials with high-dimensional energy landscapes which then determine their physical and mechanical properties. The bridge from these energy landscapes to the material properties may be built via statistical mechanics.

If classical statistical mechanics is used to study finite-temperature materials properties, it is convenient for discussion to first introduce the canonical partition function for a system of  $N$  identical particles [128]

$$\begin{aligned} Q(N, V, T) &= \frac{1}{N!h^{3N}} \int d^N \mathbf{p} \int_{D(V)} d^N \mathbf{r} \exp \left\{ -\beta \left[ \sum_{i=1}^N \frac{\mathbf{p}_i^2}{2m_i} + U(\mathbf{r}_1, \dots, \mathbf{r}_N) \right] \right\} \\ &= \frac{1}{N!h^{3N}} \int d^N \mathbf{p} \int_{D(V)} d^N \mathbf{r} \exp \{ -\beta H(\mathbf{p}_1, \dots, \mathbf{p}_N, \mathbf{r}_1, \dots, \mathbf{r}_N) \}, \end{aligned} \quad (2.29)$$

where  $\mathbf{p}_i$  and  $\mathbf{r}_i$  are the momentum and the position of atom  $i$ ,  $m_i$  is the mass of atom  $i$ ,  $U$  is the potential energy as a function of atomic positions, and  $D(V)$  is the range of integration of each position variable defined by the containing volume  $V$ . The classical Hamiltonian  $H(\{\mathbf{p}_i, \mathbf{r}_i\})$  is defined as the sum of the kinetic energy and the potential energy.

The canonical distribution density is given as

$$\rho(\mathbf{p}_1, \dots, \mathbf{p}_N, \mathbf{r}_1, \dots, \mathbf{r}_N) = \frac{1}{Q} \exp \{ -\beta H(\mathbf{p}_1, \dots, \mathbf{p}_N, \mathbf{r}_1, \dots, \mathbf{r}_N) \}. \quad (2.30)$$

For a given observable  $O$ , its thermal average value can be evaluated via

$$\langle O \rangle = \int d^N \mathbf{p} \int_{D(V)} d^N \mathbf{r} O(\mathbf{p}_1, \dots, \mathbf{p}_N, \mathbf{r}_1, \dots, \mathbf{r}_N) \rho(\mathbf{p}_1, \dots, \mathbf{p}_N, \mathbf{r}_1, \dots, \mathbf{r}_N). \quad (2.31)$$

Clearly, the thermal average Eq. (2.31) is defined as a high-dimensional integral, and the analytic result is not available for most cases. The Markov chain Monte

Carlo (MCMC) is one of the most widely used methods to deal with this problem numerically. The aim of MCMC is to draw a series of samples  $\{X_1, X_2, \dots, X_M\}$  according to the canonical distribution function, where  $X_i$  represents the  $i$ th sample and contains all microscopic variables at this state. These samples can then be used to estimate the thermal average of any observable,

$$\langle O \rangle \approx \frac{1}{M} \sum_{I=1}^M O(X_I) \quad (2.32)$$

The left-hand side is not exactly equal to the right-hand side as only a limited number of samples can be drawn in practice, implying an estimation error. This estimation error decreases with the increasing number of samples, and the right-hand side of Eq. (2.32) converges to the exact value when the number of samples goes to infinity.

For the application of MCMC, the key point is to construct an update method that generates each new state directly from the preceding state and leaves the canonical distribution function invariant. In Hamiltonian (hybrid) MC [34], Hamiltonian dynamics is employed as an efficient Metropolis [93] update. It does the following:

- When the current state is  $X_I$ , perform a Gibbs sampling for the momentum variables and generate a new state  $\bar{X}_I$ . In other words, randomly choose new values of the momentum variables according to their Gaussian distribution,

$$\rho(\mathbf{p}_1, \dots, \mathbf{p}_N) = \prod_{i=1}^N \left( \frac{\beta}{2\pi m_i} \right)^{3/2} \exp \left\{ -\beta \sum_{i=1}^N \frac{\mathbf{p}_i^2}{2m_i} \right\}, \quad (2.33)$$

and assign them to the new state  $\bar{X}_I$ .

- Run Hamiltonian dynamics for a specific trajectory length  $L$  with the initial state  $X^{\text{HD}}(0)$  chosen as  $\bar{X}_I$ . The equations of motion for Hamiltonian dynamics are given as

$$\begin{aligned} \frac{d\mathbf{q}_i}{dt} &= \frac{\mathbf{p}_i}{m_i} \\ \frac{d\mathbf{p}_i}{dt} &= -\frac{\partial U}{\partial \mathbf{q}_i}. \end{aligned} \quad (2.34)$$

The final state of the Hamiltonian-dynamics trajectory is denoted as  $X^{\text{HD}}(L)$ .

- Negate the momentum variables of  $X^{\text{HD}}(L)$  to obtain the proposed state  $\bar{X}_{I+1}$  for a Metropolis update. The negation makes it deterministic that the proposal state is  $\bar{X}_I$  if the current state is  $\bar{X}_{I+1}$ , and is necessary to make the proposal symmetric.
- Calculate the Metropolis acceptance ratio

$$p^{\text{accp}}(\bar{X}_I \rightarrow \bar{X}_{I+1}) = \min \{1, \exp[\beta H(\bar{X}_I) - \beta H(\bar{X}_{I+1})]\}. \quad (2.35)$$

- Accept the proposed state  $\bar{X}_{I+1}$  as the next state  $X_{I+1}$  of the Markov chain with the probability  $p^{\text{accp}}$ .
- Repeat the steps above to generate a Markov chain.

We next discuss why Hamiltonian MC works, and this will offer us some guidelines to construct Hamiltonian MC algorithms for the spin system in chapter 4. The canonical distribution is correctly sampled by Hamiltonian MC if it is ergodic and if it leaves the canonical distribution invariant [98]. The ergodicity requirement means that the samples generated by MC can not be trapped in some specific areas in phase space and all states can be visited within finite steps. The ergodicity of Hamiltonian MC is guaranteed by the random noise introduced in the Gibbs sampling as we draw randomly the momentum variables from Gaussian distributions. We next prove that Hamiltonian MC leaves the canonical distribution invariant. There are two types of update in Hamiltonian MC, the Gibbs sampling and the Metropolis update based on Hamiltonian dynamics, and we need to show that both preserve the canonical distribution. The Gibbs sampling leaves the canonical distribution invariant as we draw the momentum variables from their conditional distribution directly. For the Metropolis update, the canonical distribution is preserved via the detailed balance [98]

$$\begin{aligned} \rho(\bar{X}_I) dV^I T(\bar{X}_I \rightarrow \bar{X}_{I+1}) \\ = \rho(\bar{X}_{I+1}) dV^{I+1} T(\bar{X}_{I+1} \rightarrow \bar{X}_I), \end{aligned} \quad (2.36)$$

where  $\rho(\bar{X}_I)$  and  $\rho(\bar{X}_{I+1})$  are the canonical distribution density at states  $\bar{X}_I$  and  $\bar{X}_{I+1}$ .  $dV^I$  is the volume element at state  $\bar{X}(I)$ , and it is transformed to  $dV^{I+1}$  at state  $\bar{X}(I+1)$  by Hamiltonian dynamics.  $T(\bar{X}_I \rightarrow \bar{X}_{I+1})$  and  $T(\bar{X}_{I+1} \rightarrow \bar{X}_I)$  are

the forward and backward transition probabilities, which can be calculated as the product of the corresponding proposal probability and acceptance probability,

$$\begin{aligned} T(\bar{X}_I \rightarrow \bar{X}_{I+1}) &= p^{\text{prop}}(\bar{X}_I \rightarrow \bar{X}_{I+1}) p^{\text{accp}}(\bar{X}_I \rightarrow \bar{X}_{I+1}), \\ T(\bar{X}_{I+1} \rightarrow \bar{X}_I) &= p^{\text{prop}}(\bar{X}_{I+1} \rightarrow \bar{X}_I) p^{\text{accp}}(\bar{X}_{I+1} \rightarrow \bar{X}_I). \end{aligned} \quad (2.37)$$

As Hamiltonian dynamics is deterministic and time-reversible, the forward and backward proposal probabilities are both equal to one. The transition probability is then simply given by the Metropolis acceptance ratio Eq. (2.35),

$$\begin{aligned} T(\bar{X}_I \rightarrow \bar{X}_{I+1}) &= p^{\text{accp}}(\bar{X}_I \rightarrow \bar{X}_{I+1}) \\ &= \min \{1, \exp[\beta H(\bar{X}_I) - \beta H(\bar{X}_{I+1})]\}, \end{aligned} \quad (2.38)$$

$$\begin{aligned} T(\bar{X}_{I+1} \rightarrow \bar{X}_I) &= p^{\text{accp}}(\bar{X}_{I+1} \rightarrow \bar{X}_I) \\ &= \min \{1, \exp[\beta H(\bar{X}_{I+1}) - \beta H(\bar{X}_I)]\}. \end{aligned} \quad (2.39)$$

Substituting Eq. (2.38), (2.39) and (2.30) into Eq. (2.36), we obtain

$$\begin{aligned} &\frac{dV^I}{Q} \exp(-\beta H(\bar{X}_I)) \min \{1, \exp[\beta H(\bar{X}_I) - \beta H(\bar{X}_{I+1})]\} \\ &= \frac{dV^{I+1}}{Q} \exp(-\beta H(\bar{X}_{I+1})) \min \{1, \exp[\beta H(\bar{X}_{I+1}) - \beta H(\bar{X}_I)]\}. \end{aligned} \quad (2.40)$$

Clearly, the detailed balance holds only when the two volume elements  $dV^I$  and  $dV^{I+1}$  are identical, which is true as Hamiltonian dynamics preserves the volume [98]. We thus draw the conclusion that Hamiltonian MC leaves the canonical distribution invariant.

In the proof of the validation of Hamiltonian MC above, we employed two properties of Hamiltonian dynamics, time-reversibility and area preservation. In the computer implementation of Hamiltonian MC, the analytic solution of Hamiltonian dynamics are normally not available, and the equations of motion must be solved approximately with numerical integration schemes. As the time-reversibility and the area preservation are necessary to leave the canonical distribution invariant, we also require numerical integration schemes to be time-reversible and area-preserving in order to guarantee correct sampling. A frequently used scheme is the velocity Verlet method [125],

$$\mathbf{p}_i(t + \epsilon/2) = \mathbf{p}_i(t) - (\epsilon/2) \frac{\partial U}{\partial \mathbf{q}_i}(\{\mathbf{q}_i(t)\}), \quad (2.41)$$

$$\mathbf{q}_i(t + \epsilon) = \mathbf{q}_i(t) + \frac{\epsilon}{m_i} \mathbf{p}_i(t + \epsilon/2), \quad (2.42)$$

$$\mathbf{p}_i(t + \epsilon) = \mathbf{p}_i(t + \epsilon/2) - (\epsilon/2) \frac{\partial U}{\partial \mathbf{q}_i}(\{\mathbf{q}_i(t + \epsilon)\}), \quad (2.43)$$

where  $\epsilon$  is the time step. It can be shown that this scheme preserves the volume in phase space and is time-reversible. We will combine this scheme with spin rotation for the auxiliary spin dynamics in chapter 4.

## 2.4 Free-energy calculations

In the last section, we introduced methods to evaluate thermal averages in the canonical ensemble. However, these methods cannot be directly employed to calculate the free energy, which is one of the key thermodynamic quantities. The reason is that the free energy is not defined via a thermal average

$$F = -\frac{1}{\beta} \ln Q, \quad (2.44)$$

where  $Q$  is the partition function introduced in the last section. We devote this section to discuss two methods for free-energy calculations, the lattice-vibration theory within the harmonic approximation and the thermodynamic integration.

### 2.4.1 Lattice vibrations within harmonic approximation

In harmonic approximation, the potential energy for nuclei can be written as

$$U_{\text{pot}}(\{\boldsymbol{\mu}_i\}) = U_0 + \frac{1}{2} \sum_{i\zeta j\eta} \Phi_{ij}^{\zeta\eta} u_i^\zeta u_j^\eta, \quad (2.45)$$

where we use  $\zeta$  and  $\eta$  to denote Cartesian components.

In this thesis, we only deal with lattices containing one in-equivalent atom. By using the periodicity of the monatomic crystal, we may rewrite the potential energy above into

$$U_{\text{pot}}(\{\boldsymbol{\mu}_i\}) = U_0 + \frac{1}{2} \sum_{i\zeta j\eta} \Phi^{\zeta\eta}(\mathbf{R}_i - \mathbf{R}_j) u_i^\zeta u_j^\eta, \quad (2.46)$$

where  $\mathbf{R}_i$  is the position of cell  $i$ . Clearly, the position of atom  $i$  is  $\mathbf{R}_i + \boldsymbol{\mu}_i$ .



The classical equation of motion for atomic vibrations is given as

$$M \frac{\partial \mu_i^\zeta}{\partial t} = - \sum_{j\eta} \Phi^{\zeta\eta}(\mathbf{R}_i - \mathbf{R}_j) u_j^\eta \quad (2.47)$$

We next exploit the translational symmetry of the crystal by applying the Fourier transformation. We substitute the expression below to the equation of motion Eq. (2.47),

$$\mu_l = \frac{1}{C} \sum_{\mathbf{q}} \mu_{\mathbf{q}} e^{-i\mathbf{R}_l \cdot \mathbf{q}}, \quad (2.48)$$

and obtain the equation,

$$M \frac{\partial \mu_{\mathbf{q}}^\zeta}{\partial t} = - \sum_{\eta} \mu_{\mathbf{q}}^\zeta \Phi_{\mathbf{q}}^{\zeta\eta}, \quad (2.49)$$

where  $\Phi_{\mathbf{q}}^{\zeta\eta}$  is given as

$$\Phi_{\mathbf{q}}^{\zeta\eta} = \sum_j e^{i\mathbf{q} \cdot (\mathbf{R}_i - \mathbf{R}_j)} \Phi^{\zeta\eta}(\mathbf{R}_i - \mathbf{R}_j). \quad (2.50)$$

The intratomic force constant can be expressed in terms of interatomic force constants due to the translational invariance of the crystal,

$$\Phi^{\zeta\eta}(\mathbf{0}) = - \sum_{j \neq i} \Phi^{\zeta\eta}(\mathbf{R}_i - \mathbf{R}_j). \quad (2.51)$$

Substituting the expression above and Euler's formula into Eq. (2.50), we obtain the expression for force constants in  $\mathbf{q}$  space in terms of interatomic force constants,

$$\begin{aligned} \Phi_{\mathbf{q}}^{\zeta\eta} &= - \sum_{j \neq i} \Phi^{\zeta\eta}(\mathbf{R}_i - \mathbf{R}_j) \{1 - \cos[\mathbf{q} \cdot (\mathbf{R}_i - \mathbf{R}_j)]\} \\ &= - \sum_{j \neq 0} \Phi^{\zeta\eta}(\mathbf{R}_j) [1 - \cos(\mathbf{q} \cdot \mathbf{R}_j)]. \end{aligned} \quad (2.52)$$

For an arbitrary  $\mathbf{q}$  point, we need to diagonalize a  $3 \times 3$  matrix  $|\Phi_{\mathbf{q}}^{\zeta\eta}|$  in order to find vibrational normal modes. For some high-symmetry points, the square of the phonon frequency can be written as a linear combination of force constants [136]. Here we take the  $N$  point of a bcc lattice as an example, and a general expression is given in [136]. This point is softened the most by the spin fluctuations, as will be shown in chapter 5. At the  $N$  point, the  $\mathbf{q}$  vector is  $(\frac{\pi}{a}, \frac{\pi}{a}, 0)$ , where  $a$  is the lattice constant. In this example, we only consider interatomic force constants

within second-nearest neighbours. We first simplify the force constant matrix by using the crystal symmetry of the bcc lattice. The first-nearest-neighbour force constant matrix at  $(a/2, a/2, a/2)$  can be written as

$$\bar{\bar{\Phi}}(a/2, a/2, a/2) = \begin{pmatrix} -\alpha_1 & -\beta_1 & -\beta_1 \\ -\beta_1 & -\alpha_1 & -\beta_1 \\ -\beta_1 & -\beta_1 & -\alpha_1 \end{pmatrix}, \quad (2.53)$$

and the second-nearest-neighbour force constant matrix at  $(a, 0, 0)$  can be written as

$$\bar{\bar{\Phi}}(a, 0, 0) = \begin{pmatrix} -\alpha_2 & 0 & 0 \\ 0 & -\beta_2 & 0 \\ 0 & 0 & -\beta_2 \end{pmatrix}. \quad (2.54)$$

We follow the convention in [136] to choose small Greek letters and subscripts. We can write out straightforwardly the force constant matrices at the other first- and second-nearest-neighbour sites by using the crystal symmetry.

After substituting Eq. (2.53), (2.54) and the other force constant matrices into Eq. (2.52) and Eq. (2.49), we obtain

$$\begin{aligned} 4\pi^2 M \nu_L^2 &= 8\alpha_1 + 8\beta_1 + 4\alpha_2 + 4\beta_2, \\ 4\pi^2 M \nu_{T_1}^2 &= 8\alpha_1 - 8\beta_1 + 4\alpha_2 + 4\beta_2, \\ 4\pi^2 M \nu_{T_2}^2 &= 8\alpha_1 + 8\beta_2, \end{aligned} \quad (2.55)$$

where  $\nu_L$ ,  $\nu_{T_1}$  and  $\nu_{T_2}$  are the vibrational frequencies of the longitudinal and transverse phonon modes at  $N$  point.

In the tight-binding model, it is convenient to use the local coordinate frame whose  $z$ -axis is along the chemical bond. The force-constant matrix in the local coordinate frame can be obtained with some simple algebra once the one in the global coordinate frame has been computed,

$$\Phi^{\zeta\eta(l)}(\mathbf{R}_i - \mathbf{R}_j) = \sum_{mn} \Phi^{\zeta\eta(g)}(\mathbf{R}_i - \mathbf{R}_j) \cdot \frac{\partial \mu_m^{(g)}}{\partial \mu_\zeta^{(l)}} \cdot \frac{\partial \mu_n^{(g)}}{\partial \mu_\eta^{(l)}}, \quad (2.56)$$

where we use the superscripts  $l$  and  $g$  to denote the local and coordinate coordinate frames.  $[\frac{\partial \mu_m^{(g)}}{\partial \mu_\zeta^{(l)}}]$  is a  $3 \times 3$  matrix that links the differentials in the two coordinate frames. For example,  $[\frac{\partial \mu_m^{(g)}}{\partial \mu_\zeta^{(l)}}]$  for the local coordinate frame for the first-nearest

neighbours in perfect bcc lattices is given as,

$$\begin{pmatrix} -\frac{1}{\sqrt{2}} & -\frac{1}{\sqrt{6}} & \frac{1}{\sqrt{3}} \\ \frac{1}{\sqrt{2}} & -\frac{1}{\sqrt{6}} & \frac{1}{\sqrt{3}} \\ 0 & \frac{2}{\sqrt{6}} & \frac{1}{\sqrt{3}} \end{pmatrix}. \quad (2.57)$$

We will use this result in chapter 5.

Once we obtain the vibrational normal modes, we are ready to decouple the system into independent harmonic oscillators and calculate the vibrational thermodynamics. For a single harmonic oscillator of frequency  $\omega_i = \frac{\varepsilon_i}{\hbar}$ , the partition function is given as

$$\begin{aligned} Z_i &= \sum_m^{\infty} \exp[-\beta(m + 1/2)\varepsilon_i] \\ &= \frac{\exp(-\beta\frac{\varepsilon_i}{2})}{1 - \exp(-\beta\varepsilon_i)}. \end{aligned} \quad (2.58)$$

With the partition function Eq. (2.58) in hand, we can calculate the phonon free energy at a given temperature  $T$  according to

$$F_i(\varepsilon_i, T) = -\frac{1}{\beta} \ln Z_i, \quad (2.59)$$

and then calculate the vibrational entropy through the negative of the derivative of the free energy Eq. (2.59) with respect to temperature,

$$\begin{aligned} S_i(\varepsilon_i, T) &= -\frac{\partial F_i}{\partial T} \\ &= k_B \left\{ -\ln [1 - \exp(-\beta\varepsilon_i)] + \frac{\beta\varepsilon_i}{\exp(\beta\varepsilon_i) - 1} \right\}. \end{aligned} \quad (2.60)$$

For the 3-dimensional solid, the phonon density of states (DOS) can be first obtained by integrating over the first Brillouin zone (1st B.Z.) in the reciprocal space

$$g(\varepsilon) = \frac{V}{(2\pi)^3} \sum_s \int_{\text{1st B.Z.}} d\mathbf{q} \delta(\varepsilon - h\nu_{\mathbf{q}s}), \quad (2.61)$$

where  $h$  is the Planck constant,  $\delta$  is the Kronecker delta function,  $s$  labels the phonon branch, and  $\nu_{\mathbf{q}s}$  represents the vibrational normal mode of phonon branch  $s$  at  $\mathbf{q}$  point.

There are  $g(\varepsilon)d\varepsilon$  phonon modes in the energy range from  $\varepsilon$  to  $\varepsilon + d\varepsilon$ , and their phonon entropy is  $S_i(\varepsilon)g(\varepsilon)d\varepsilon$ . The total vibrational entropy can be obtained by summing up the phonon entropy of all phonon modes

$$S_{\text{vib}}(T) = \int_0^\infty S_i(\varepsilon, T)g(\varepsilon)d\varepsilon. \quad (2.62)$$

Likewise, we can compute the phonon free energy of the 3-dimensional solid according to,

$$F_{\text{vib}}(T) = \int_0^\infty F_i(\varepsilon, T)g(\varepsilon)d\varepsilon. \quad (2.63)$$

## 2.4.2 Thermodynamic integration

The thermodynamic-integration approach aims to calculate the free-energy difference instead of the absolute value. In this method, the free-energy difference is evaluated according to [24]

$$F(\xi_1) - F(\xi_0) = \int_{\xi_0}^{\xi_1} \frac{dF}{d\xi} d\xi. \quad (2.64)$$

where  $\xi$  is a reaction coordinate and specifies a point on the free-energy surface. The key observation in the thermodynamic integration is that the derivative of the free energy with respect to the reaction coordinate,  $\frac{dF}{d\xi}$ , can be calculated through an ensemble average [24]

$$\frac{dF}{d\xi} = \left\langle \frac{\partial \mathcal{H}}{\partial \xi} \right\rangle_\xi. \quad (2.65)$$

In classical statistical mechanics, the contribution of the kinetic energy is cancelled out in the free-energy difference, and we only need to consider the contribution of the potential energy

$$\frac{dF}{d\xi} = \left\langle \frac{\partial U_{\text{pot}}}{\partial \xi} \right\rangle_\xi. \quad (2.66)$$

## 2.5 Machine learning

Artificial neural networks are inspired by the mechanism of our brains and have been a research topic since 1960s. In around 2006, The training of deep architectures, known as deep learning, became successful [16, 56], which leads to the

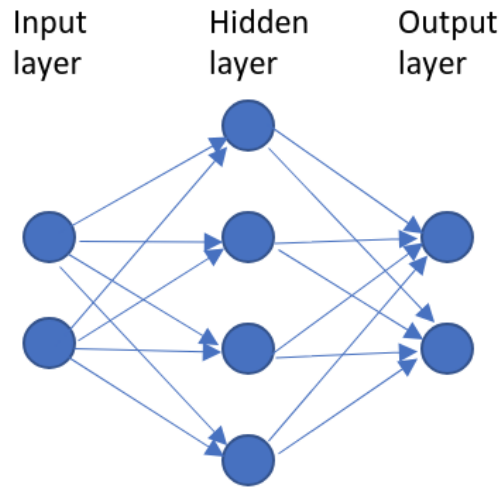


Figure 2.1: A schematic diagram for artificial neural networks

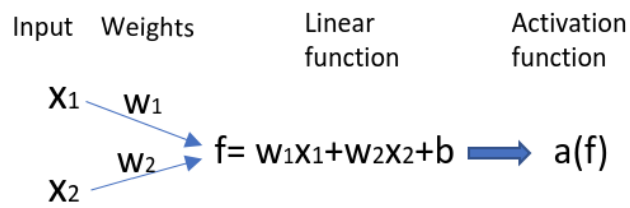


Figure 2.2: The basic element of artificial neural networks

flourish of the artificial intelligence till today. The basic architecture of an artificial network is shown in Fig. 2.1. The input layer encodes the initial data into the neural network, which are then processed by one or more hidden layers. The output layer produces the final processed data and transfer information from the neural network to the outside world.

We show in Fig. 2.2 the mathematical model for the basic element or the single neuron of an artificial neural network. It is composed of a linear function which sums up linearly the contributions of all inputs and an activation function which introduces non-linearity into the neural network. The frequently-used activation functions include the sigmoid function, the tanh function, and the rectified linear unit.

# Chapter 3

## Finite-temperature magnetic tight binding

### 3.1 Introduction

The inclusion of thermal excitations into materials simulation is one of the main challenges in computer-aided materials design. For magnetic transition metals, the thermal excitations of both the spin and the atomic degrees of freedom and more importantly, their coupling (magnon-phonon coupling), should be taken into account [5, 73], which makes the situation even more complex. The widely-used adiabatic decoupling of different degrees of freedom [69, 74] neglects the coupling between the spin and atomic excitations based on the consideration that they have very different time scales, and becomes problematic especially at high temperatures (see detailed discussion e.g., in Arbikosov et al. [5]).

Recent years have evidenced heated efforts and great progress to go beyond the adiabatic decoupling, and there are mainly two branches in the development of the new methods. The starting point of the first branch builds on the success of the Finnis-Sinclair potential [41] for non-magnetic metals. As the first step, Dudarev and Derlet proposed the 'magnetic' interatomic potential by adding a new term to account for the energy gain due to the broken symmetry in the ferromagnetic ground state [35]. The missing of collective magnetic excitations in this model is then completed by adding a classical Heisenberg model and the coupling between the spin and atomic degrees of freedom is treated through an empirical coordinate-dependent exchange function [89]. This model may be solved with a classical spin-lattice dynamics approach [89, 127], and as a success, both the

bcc-fcc and the fcc-bcc phase transitions in iron are successfully simulated with a careful parametrization of the model [88]. The starting point of the second branch builds on the success of the density-functional theory [59, 65, 67]. The disordered-local-moment (DLM) method which is either implemented with coherent-potential-approximation [49] or ab initio molecular dynamics [7, 118, 119] makes it possible to simulate the spin-excitation effect in first-principles calculations. A more accurate method, the combination of DFT and the dynamical mean-field theory (DMFT) [45] is developed to treat the strong electronic correlations at finite temperatures, and the simulations for real materials are performed to study magnetic [63, 84] and structural phase transitions [81–83]. However, both DLM and DMFT methods neglect the magnetic short-range order or non-collinearity of magnetism, and hence only work for magnetically disordered structures. This leads to the development of the non-collinear magnetism in DFT [57, 77, 78, 87, 105, 121] together with ab initio spin dynamics [9, 10], which makes it possible to simulate the transverse spin-wave excitations at the first-principles level. To summarize, the main advantage of the former branch is the affordability to perform large-scale simulations, while the disadvantage is the missing of a proper description of electronic structures, which is crucial for complex spin interactions [79] and magnon-phonon couplings [73] in magnetic transition metals. The latter branch has a better accuracy, but its computational cost limits the exploration of many important real-life material-science problems, e.g., to our knowledge, there is no successful direct simulations of structural phase transitions of iron with it.

Our approach is based on the semi-empirical tight binding model, which has been shown to successfully simulate a wide range of non-magnetic materials [40, 108, 109, 113] and also ferromagnetic metals at ground states [102]. In order to treat the longitudinal and transverse spin fluctuations in magnetic transition metals at finite temperature, we extend magnetic tight binding [33, 102] by quantizing the exchange interaction and performing the Hubbard-Stratonovich transformation within the static approximation [62]. We show a successful application of our model to iron in chapter 5.

## 3.2 Methodology

The potential energy in magnetic tight binding [11, 33, 102] is expressed as

$$U_{\text{MTB}}(\{\mathbf{r}_i\}) = \text{Tr}(\hat{\mathcal{H}}^{(0)}(\{\mathbf{r}_i\})\hat{\rho}) + \frac{1}{2} \sum_i \bar{U}_i q_i^2 - \frac{1}{4} \sum_i J_i |\mathbf{m}_i|^2 + E_{\text{pair}}(\{\mathbf{r}_i\}), \quad (3.1)$$

where  $\hat{\mathcal{H}}^{(0)}$  is the Hamiltonian of the reference state composed of non-magnetic free atoms,  $\hat{\rho}$  is the charge-density operator,  $q_i$  is the Mulliken charge with respect to the population of free atoms,  $q_i = n_i - n_i^{(0)}$ ,  $\mathbf{m}_i$  is the atomic magnetic moment.  $q_i$  and  $\mathbf{m}_i$  are not free variables and should be determined in a self-consistent manner. The first term in Eq. (3.1) describes the energy associated with the reference state, the second and the third terms are the Coulomb energy and the exchange energy, and the last term is the empirical pair-wise interaction to account for the remaining contributions. A more detailed discussion of Eq. (3.1) is referred to Section 2.1.2 in the last chapter.

In order to add collective magnetic excitations to magnetic tight binding, we first put aside the Coulomb interaction (the second term in Eq. (3.1)) and the empirical pair-wise interaction (the last term in Eq. (3.1)) and quantize the exchange interaction (the third term in Eq. (3.1)) to obtain the Hamiltonian to describe the electronic system

$$\hat{\mathcal{H}} = \hat{\mathcal{H}}^{(0)} - \sum_i J_i (\mathbf{e}_i \hat{\mathbf{S}}_i)^2, \quad (3.2)$$

where we introduced the spin operator  $\hat{\mathbf{S}}_i$  and the spin quantization axis  $\mathbf{e}_i$  at site  $i$ . The Hamiltonian Eq. (3.2) is denoted as the quantized magnetic Hamiltonian in this thesis. The corresponding partition function can be formally written as

$$Q = \text{Tr}(e^{-\beta\hat{\mathcal{H}}}). \quad (3.3)$$

We aim at obtaining a model that describes atomic and magnetic degrees of freedom on the equal footing, and this can be realized by treating the partition function Eq. (3.3) with the Hubbard-Stratonovich transformation and the static approximation. The Hubbard-Stratonovich transformation [61, 122] is defined via the integral identity

$$\exp\left(\frac{a}{2}x^2\right) = \sqrt{\frac{1}{2\pi a}} \int_{-\infty}^{\infty} \exp\left(-\frac{y^2}{2a} - xy\right) dy, \quad (3.4)$$



where the real constant  $a > 0$ . To apply the Hubbard-Stratonovich transformation to the partition function of the many-electron system, it is convenient to use the identity below [62]

$$\begin{aligned} & \text{Tr exp} \left\{ -\beta \hat{\mathcal{H}}^{(0)} + \beta \frac{a}{2} \sum_i (\hat{X}_i)^2 \right\} \\ &= \left( \frac{1}{2\pi a} \right)^{N/2} \int \prod_i [D\nu_i(t)] \exp \left\{ -\frac{1}{2a} \sum_i \int_0^\beta [\nu_i(t)]^2 dt \right\} \cdot \\ & \quad \text{Tr exp}_+ \left\{ -\int_0^\beta \hat{\mathcal{H}}^{(0)}(t) dt - \sum_i \int_0^\beta \nu_i(t) \hat{X}_i(t) dt \right\}, \end{aligned} \quad (3.5)$$

where  $t$  is the imaginary time and varies from 0 to  $\beta$ .  $\nu_i(t)$  is a time-dependent fluctuating field at site  $i$ . The subscript  $+$  means that the operator is time-ordered. The prefactor  $\left(\frac{1}{2\pi a}\right)^{N/2}$  will be cancelled out when we calculate the free-energy difference between two phases. We simply omit it from now on.

We may employ the identity Eq. (3.5) to reformulate the partition function Eq. (3.3) into a path integral, which is still difficult to handle. A further simplification is to drop out the time-fluctuating part in the path integral using the static approximation [62], and Eq. (3.5) can be simplified to be

$$\begin{aligned} & \text{Tr exp} \left[ -\beta \hat{\mathcal{H}}^{(0)} + \beta \frac{a}{2} \sum_i (\hat{X}_i)^2 \right] \\ & \approx \int \prod_i d\nu_i \exp \left[ -\frac{1}{2a} \sum_i \nu_i^2 \right] \cdot \text{Tr exp} \left[ -\beta \hat{\mathcal{H}}^{(0)} - \beta \sum_i \nu_i \hat{X}_i \right]. \end{aligned} \quad (3.6)$$

We are now ready to simplify the partition function Eq. (3.3) into a form that is easy to handle. We employ Eq. (3.6) and transform Eq. (3.3) to

$$\begin{aligned} Q & \approx \int \prod_i dh_i \exp \left[ -\beta \sum_i \frac{1}{J_i} h_i^2 \right] \\ & \quad \cdot \text{Tr} \left\{ \exp \left[ -\beta \left( \hat{\mathcal{H}}^{(0)} + 2 \sum_i h_i \mathbf{e}_i \hat{\mathbf{S}}_i \right) \right] \right\}, \end{aligned} \quad (3.7)$$

where  $h_i$  is the scalar (auxiliary) exchange field at atom  $i$ . As discussed by Hubbard [62], this partition function is not rotational invariant, and the rotational invariance

can be restored by averaging over the quantization axis  $\{\mathbf{e}_i\}$ ,

$$\begin{aligned}
Q &\approx \int \prod_i d\mathbf{h}_i \exp \left[ -\beta \left( \sum_i \frac{1}{J_i} \mathbf{h}_i^2 \right) \right] \\
&\quad \text{Tr} \exp \left[ -\beta \left( \hat{\mathcal{H}}^{(0)} + 2 \sum_i \mathbf{h}_i \hat{\mathbf{S}}_i \right) \right] \\
&\equiv \int \prod_i d\mathbf{h}_i \exp \left[ -\beta \left( \sum_i \frac{1}{J_i} \mathbf{h}_i^2 + \Omega(\{\mathbf{h}_i\}) \right) \right]
\end{aligned} \tag{3.8}$$

where we introduced the vector exchange field,  $\mathbf{h}_i = \mathbf{e}_i h_i$ , and the electronic free energy

$$\begin{aligned}
\Omega(\{\mathbf{h}_i\}) &= -\frac{1}{\beta} \ln \text{Tr} \exp \left[ -\beta \left( \hat{\mathcal{H}}^{(0)} + 2 \sum_i \mathbf{h}_i \hat{\mathbf{S}}_i \right) \right] \\
&\equiv -\frac{1}{\beta} \ln \text{Tr} \exp \left[ -\beta \hat{\mathcal{H}}_{\text{eff}} \right].
\end{aligned} \tag{3.9}$$

The single-electron effective Hamiltonian is defined as  $\hat{\mathcal{H}}_{\text{eff}} = \hat{\mathcal{H}}_0 + 2 \sum_i \mathbf{h}_i \hat{\mathbf{S}}_i$ , in which the direct electron-electron interactions are replaced by the interactions between exchange fields  $\mathbf{h}_i$  and spin operators  $\hat{\mathbf{S}}_i$ . The temperature in Eq. (3.9) describes the free-electron excitations. As we are only interested in the collective magnetic excitations, we quench the free-electron excitations by replacing the electronic free energy  $\Omega$  by the band energy  $E_{\text{band}}$

$$\begin{aligned}
E_{\text{band}} &= \Omega_{T=0K} \\
&= \sum_n^{\text{occ}} \epsilon_n,
\end{aligned} \tag{3.10}$$

with  $\epsilon_n$  the  $n$ th eigenvalues of  $\hat{\mathcal{H}}_{\text{eff}}$ , and obtain the magnetic partition function

$$\begin{aligned}
Z^{\text{mag}} &\approx \int \prod_i d\mathbf{h}_i \exp \left[ -\beta \left( \sum_i \frac{1}{J_i} \mathbf{h}_i^2 + E_{\text{band}} \right) \right] \\
&\equiv \int \prod_i d\mathbf{h}_i \exp [-\beta U_{\text{pot}}],
\end{aligned} \tag{3.11}$$

where we defined the potential energy

$$U_{\text{pot}} = \sum_i \frac{1}{J_i} \mathbf{h}_i^2 + E_{\text{band}}. \tag{3.12}$$

Now we are ready to add the Coulomb interaction and the empirical pair-wise interaction into the potential energy above,

$$U_{\text{pot}}(\{\mathbf{r}_i, \mathbf{h}_i\}) = E_{\text{band}} - \frac{1}{2} \sum_i \bar{U}_i q_i^2 + \sum_i \frac{1}{J_i} \mathbf{h}_i^2 + E_{\text{pair}}, \quad (3.13)$$

which is now a function of atomic positions  $\{\mathbf{r}_i\}$  and exchange fields  $\{\mathbf{h}_i\}$ . The sign of the second term in Eq. (3.13) is different from that in Eq. (3.1) simply because there is double counting in the band energy in Eq. (3.13). A Coulomb term should also be added into the single-electron effective Hamiltonian as a consequence of the optimization treatment of the charge degrees of freedom [33],

$$\begin{aligned} \hat{\mathcal{H}}_{\text{eff}} &= \hat{\mathcal{H}}^{(0)} + \sum_i \bar{U}_i q_i \hat{\mathbf{n}}_i + 2 \sum_i \mathbf{h}_i \hat{\mathbf{S}}_i \\ &\equiv \hat{\mathcal{H}}^{(0)} + \sum_i \mu_i \hat{\mathbf{n}}_i + 2 \sum_i \mathbf{h}_i \hat{\mathbf{S}}_i \end{aligned} \quad (3.14)$$

where the term  $\bar{U}_i q_i$  works as a Coulomb field  $\mu_i$  that is induced by the local charge and the charge  $q_i$  should be determined self-consistently as it appears in the Hamiltonian.

Within the two-center approximation [116], the intersite matrix element of the Hamiltonian  $\hat{\mathcal{H}}^{(0)}$  is parametrized as a pair-wise function of distance, and the analytic atomic force can be expressed as

$$\mathbf{F}_i = -\frac{\partial U_{\text{pot}}}{\partial \mathbf{r}_i} = -\sum_{\alpha j \beta \sigma, j \neq i} \left( \rho_{\sigma}^{i\alpha, j\beta} \frac{\partial H_{j\beta, i\alpha}^{(0)}}{\partial \mathbf{r}_i} + \rho_{\sigma}^{j\beta, i\alpha} \frac{\partial H_{i\alpha, j\beta}^{(0)}}{\partial \mathbf{r}_i} \right) - \frac{\partial E_{\text{pair}}}{\partial \mathbf{r}_i}, \quad (3.15)$$

where  $\rho_{\sigma}^{i\alpha, j\beta}$  is the bond order between orbital  $\alpha$  of atom  $i$  and orbital  $\beta$  of atom  $j$  in spin  $\sigma$  channel  $\rho_{\sigma}^{i\alpha, j\beta} = \langle i\alpha | \hat{\rho} | j\beta \rangle$ , and  $H_{i\alpha, j\beta}^{(0)}$  is the matrix element of the Hamiltonian  $\hat{\mathcal{H}}^{(0)}$ .

The gradient of the potential energy with respect to the exchange field  $\mathbf{h}_i$  can also be obtained analytically

$$\frac{\partial U_{\text{pot}}}{\partial \mathbf{h}_i} = \frac{2\mathbf{h}_i}{J_i} - \mathbf{m}_i. \quad (3.16)$$

Eq. (3.13), (3.14), (3.15), and (3.16) are the key results in our model. We call our model the spin-lattice fluctuation theory as both spin fluctuations and atomic

vibrations are taken into account. The magnetic ground-state solution can be obtained by letting Eq. (3.16) equal zero

$$\mathbf{h}_i = \frac{1}{2} J_i \mathbf{m}_i, \quad (3.17)$$

which is nothing but the self-consistency criterion for the magnetic degrees of freedom in magnetic tight binding [33, 102]. We restore the potential energy in magnetic tight binding Eq. (3.1) by substituting Eq. (3.17) into the potential energy of our model Eq. (3.13). As expected, the magnetic ground-state solution of our model corresponds to the conventional magnetic tight-binding models [33, 102].

### 3.3 Transverse spin fluctuations

The magnetic partition function Eq. (3.11) contains both longitudinal and transverse spin fluctuations. In some cases, the longitudinal and transverse magnetic degrees of freedom may be adiabatically decoupled and a simpler model of unit spin vectors might be effective [29]. We may obtain an energy surface of the transverse spin degrees of freedom  $U_{\text{pot}}(\{\mathbf{r}_i, \mathbf{e}_i\})$  by treating adiabatically the longitudinal degrees of freedom in Eq. (3.13),

$$\frac{\partial U_{\text{pot}}}{\partial |\mathbf{h}_i|} = 0. \quad (3.18)$$

Eq. (3.18) means that for every magnetic configuration composed of unit spin vectors,  $\{\mathbf{e}_i\}$ , we optimize the potential energy Eq. (3.13) with respect to all longitudinal degrees of freedom  $|\mathbf{h}_i|$ . The magnetic partition function for transverse spin fluctuations can then be defined as

$$Z^{\text{TSF}} \approx \int \prod_i d\mathbf{e}_i \exp[-\beta U_{\text{pot}}(\{\mathbf{r}_i, \mathbf{e}_i\})]. \quad (3.19)$$

We note that this treatment of the transverse spin fluctuations is merely an approximation. The unit vector  $\mathbf{e}_i$  represents the direction of the exchange field  $\mathbf{h}_i$  as compared to the classical spin vector  $\mathbf{s}_i$  defined as the direction of the atomic magnetic moment in some of the others' work [28, 29, 86, 87, 111]. The advantage of the former treatment compared to the later one is that the complicated constrained calculations are avoided and the numerical implementation is expected to be more robust in practice.

### 3.4 Derivation of the quantized magnetic Hamiltonian

In the last section, we obtained the quantized magnetic Hamiltonian Eq. (3.2) by quantizing the exchange interaction in magnetic tight binding, which is merely an approximation. In this section, we give a formal derivation of this Hamiltonian. In principle, the many-electron system can be accurately described by the Hamiltonian below in the second-quantization form

$$\begin{aligned}\hat{\mathcal{H}} &= \hat{\mathcal{H}}^{(0)} + \hat{V}, \\ \hat{V} &= \frac{1}{2} \sum_{\sigma\sigma'} \sum_{il} \sum_{i'l'} \sum_{mm'} \sum_{pp'} V_{ill'i'}^{mpp'm'} \hat{c}_{im\sigma}^\dagger \hat{c}_{lp\sigma'}^\dagger \hat{c}_{l'p'\sigma'} \hat{c}_{i'm'\sigma}, \\ V_{ill'i'}^{mpp'm'} &= e^2 \int \int d\mathbf{r} d\mathbf{r}' \frac{1}{|\mathbf{r} - \mathbf{r}'|} W_m(\mathbf{r} - \mathbf{R}_i) W_p(\mathbf{r}' - \mathbf{R}_l) W_{p'}(\mathbf{r}' - \mathbf{R}_{l'}) W_{m'}(\mathbf{r} - \mathbf{R}_{i'}),\end{aligned}\tag{3.20}$$

where  $\hat{\mathcal{H}}^{(0)}$  is the non-interacting part of the Hamiltonian that contains no electron-electron interactions, and  $\hat{V}$  is the interaction Hamiltonian that describes electron-electron interactions.  $W_m(\mathbf{r} - \mathbf{R}_i)$  represents the  $m$ th Wannier orbital at site  $i$ . In our work, we replace the Wannier-orbital basis by the orthogonal atomic-orbital basis and denote this treatment as tight-binding approximation.

The interaction Hamiltonian  $\hat{V}$  contains both inter-atomic and intra-atomic contributions. If we neglect the inter-atomic contributions and only consider intra-atomic electron-electron interactions, the interaction Hamiltonian  $\hat{V}$  can be significantly simplified [94]

$$\begin{aligned}\hat{V} &\approx \frac{1}{2} \sum_i \sum_\sigma \left\{ \sum_{mm'} U_{i,mm'} \hat{n}_{im\sigma} \hat{n}_{im'\sigma} \right. \\ &\quad \left. + \sum_{m \neq m'} \left[ (U_{i,mm'} - J_{i,mm'}) \hat{n}_{im\sigma} \hat{n}_{im'\sigma} - J_{i,mm'} c_{im\sigma}^\dagger c_{im-\sigma} c_{im'\sigma}^\dagger c_{im'-\sigma} \right] \right\}.\end{aligned}\tag{3.21}$$

$U_{i,mm'}$  and  $J_{i,mm'}$  are the Coulomb and exchange integrals and defined as

$$\begin{aligned}U_{i,mm'} &= V_{iii}^{mm'm'm}, \\ J_{i,mm'} &= V_{iii}^{mm'mm'}.\end{aligned}\tag{3.22}$$

The orbital-resolved Coulomb and exchange integrals in Eq. (3.21) are difficult to handle. A frequently-used simplification is to replace  $U_{i,mm'}$  and  $J_{i,mm'}$  by their

average values  $U_i$  and  $J_i$ , and to simplify the interaction Hamiltonian as

$$\begin{aligned}\hat{V} &\approx \frac{1}{2} \sum_i \sum_{m,m'} \sum_{\sigma} U_i \hat{n}_{im\sigma} \hat{n}_{im'\sigma} + \frac{1}{2} \sum_i \sum_{m \neq m'} \sum_{\sigma} (U_i - J_i) \hat{n}_{im\sigma} \hat{n}_{im'\sigma} \\ &\quad - \frac{1}{2} \sum_i \sum_{m \neq m'} \sum_{\sigma} J_i \hat{c}_{im\sigma}^{\dagger} \hat{c}_{im-\sigma} \hat{c}_{im'\sigma}^{\dagger} \hat{c}_{im'-\sigma},\end{aligned}\tag{3.23}$$

A further simplification is to drop out the last term in Eq. 3.23 within the diagonal density approximation [66]. Then the interaction Hamiltonian becomes

$$\begin{aligned}\hat{V} &\approx \frac{1}{2} \sum_i \sum_{m,m'} \sum_{\sigma} U_i \hat{n}_{im\sigma} \hat{n}_{im'\sigma} + \frac{1}{2} \sum_i \sum_{m \neq m'} \sum_{\sigma} (U_i - J_i) \hat{n}_{im\sigma} \hat{n}_{im'\sigma} \\ &\equiv \frac{1}{2} \sum_{i\sigma} U_i \hat{n}_{i\sigma} \hat{n}_{i-\sigma} + \frac{1}{2} \sum_{i\sigma} (U_i - J_i) \hat{n}_{i\sigma} \hat{n}_{i\sigma} - \frac{1}{2} \sum_{i\sigma} (U_i - J_i) \hat{n}_{i\sigma},\end{aligned}\tag{3.24}$$

where we employed the identities below from the first to the second line on the right-hand side,

$$\begin{aligned}\hat{n}_{i\sigma} &= \sum_m \hat{n}_{im\sigma}, \\ (\hat{n}_{im\sigma})^2 &= \hat{n}_{im\sigma}.\end{aligned}\tag{3.25}$$

The second identity is valid due to the Pauli principle.

We next choose the quantization axis at the site  $i$  along a chosen direction  $\mathbf{e}_i$  and use the following identities,

$$\begin{aligned}\mathbf{e}_i \hat{\mathbf{S}}_i &= \frac{1}{2} (\hat{n}_{i\uparrow} - \hat{n}_{i\downarrow}), \\ \hat{n}_i &= \hat{n}_{i\uparrow} + \hat{n}_{i\downarrow},\end{aligned}\tag{3.26}$$

to reformulate the interaction Hamiltonian Eq. (3.24) as

$$\begin{aligned}\hat{V} &\approx \frac{1}{2} \sum_i \left( U_i - \frac{1}{2} J_i \right) (\hat{n}_i)^2 - \sum_i J_i (\mathbf{e}_i \hat{\mathbf{S}}_i)^2 - \frac{1}{2} \sum_{i\sigma} (U_i - J_i) \hat{n}_{i\sigma} \\ &\equiv \frac{1}{2} \sum_i \bar{U}_i (\hat{n}_i)^2 - \sum_i J_i (\mathbf{e}_i \hat{\mathbf{S}}_i)^2 - \frac{1}{2} \sum_{i\sigma} (U_i - J_i) \hat{n}_{i\sigma},\end{aligned}\tag{3.27}$$

where we introduced the spin operator  $\hat{\mathbf{S}}_i$  and the new parameter  $\bar{U}_i = U_i - \frac{1}{2} J_i$ . The last term does not contain quadratic contributions and from now on we group it into the non-interacting-electron Hamiltonian  $\hat{\mathcal{H}}^{(0)}$ . Now we obtain a simplified many-electron Hamiltonian

$$\hat{\mathcal{H}} \approx \hat{\mathcal{H}}^{(0)} - \sum_i J_i (\mathbf{e}_i \hat{\mathbf{S}}_i)^2 + \frac{1}{2} \sum_i \bar{U}_i (\hat{n}_i)^2.\tag{3.28}$$

We see that the only difference between Eq. (3.28) and Eq. (3.2) is the last term in Eq. (3.28), which corresponds to a quantized treatment of the Coulomb interaction and is replaced by a mean-field treatment in our model.

### 3.5 Comparison with the constrained magnetic tight binding

A widely-used approach for investigating magnetic excitations with first-principles calculations is the constrained local-moment method [49, 78, 87, 121, 129]. In this subsection, we make a comparison between our model and this approach in the framework of tight binding. This approach is based on a phenomenological theory of spin fluctuations with the partition function defined as [94]

$$Z = \int \delta \mathbf{M}(\mathbf{r}) \exp \{ -\beta U_{\text{pot}}[\mathbf{M}(\mathbf{r})] \}, \quad (3.29)$$

where  $\mathbf{M}(\mathbf{r})$  represents the space-varying spin density, and  $U_{\text{pot}}[\mathbf{M}(\mathbf{r})]$  the energy functional. For the magnetic transition metals, the spin density is localized around the atomic sites due to the localized nature of the  $d$ -band electrons. The local atomic magnetic moment  $\mathbf{m}_i$  can be defined, and the spin density can be discretized as a series of atomic magnetic moments  $\{\mathbf{m}_i\}$ . The partition function can be approximated as

$$Z = \int \prod_i d\mathbf{m}_i \exp [ -\beta U_{\text{pot}}(\{\mathbf{m}_i\}) ]. \quad (3.30)$$

The energy  $U_{\text{pot}}(\{\mathbf{m}_i\})$  is now defined as a function of magnetic configurations and can be evaluated by adding constraints in the density-functional theory for non-collinear magnetism.

This phenomenological approach also applies to tight binding. We first introduce the local atomic magnetic moment in tight binding, which can be naturally defined as a thermal average of the spin operator with respect to the intersite electron hoppings,  $\mathbf{m}_i = -2\langle \hat{\mathbf{S}}_i \rangle$ . This definition of the local atomic magnetic moments is based on the same physical reasoning with that in density-functional theory, namely, the time scale of the intersite electron hoppings, the “quantum fluctuation time” is of order  $10^{-15}$  s for 3d transition metals, and the corresponding fast quantum fluctuations can be averaged over and lead to magnetic moments per atom [23]. The atomic magnetic moments are then constrained to be the values

of a specific magnetic configuration  $\{\mathbf{m}_i\}$  by applying constraints on the single-electron Hamiltonian and satisfying the constraining criterion. The constraining Hamiltonian is defined as

$$\hat{\mathcal{H}}_{\text{cons}} = \sum_{i\alpha j\beta\sigma} H_{i\alpha,j\beta}^{(0)} \hat{c}_{i\alpha\sigma}^\dagger \hat{c}_{j\beta\sigma} + 2 \sum_i \mathbf{h}_i \hat{\mathbf{S}}_i + \sum_i \mu_i \hat{n}_i, \quad (3.31)$$

where  $\mathbf{h}_i$  is interpreted as the constraining field with the constraining criterion given as

$$-2\langle \mathbf{S}_i \rangle = \mathbf{m}_i, \quad (3.32)$$

and has a different physical meaning with the (auxiliary) exchange field in Eq. (3.14). The constraining fields work as three-dimensional Lagrange multipliers to constrain the system to a specific magnetic configurations  $\{\mathbf{m}_i\}$  whereas the (auxiliary) exchange fields are introduced from the Hubbard-Stratonovich transformation. The Coulomb field  $\mu_i$  in Eq. (3.31) is the same with that in Eq. (3.14) and should be determined in a self-consistent manner. In practice, we tune the constraining field  $\mathbf{h}_i$  in order to satisfy Eq. (3.32). The kinetic energy for the constrained electron system can be obtained by subtracting the interaction energy between the constraining fields and the atomic magnetic moments from the band energy  $E_{\text{band}}$  for the Hamiltonian Eq. (3.31)

$$U_{\text{kin}} = E_{\text{band}} + \sum_i \mathbf{h}_i \mathbf{m}_i. \quad (3.33)$$

The interaction energy associated with atomic magnetic moments can be approximated as a Stoner-like term [11, 33]

$$U_{\text{X}} = -\frac{1}{4} \sum_i J_i \mathbf{m}_i^2. \quad (3.34)$$

The total energy in Eq. (3.30) is defined as the sum of the kinetic energy Eq. (3.33) and the interaction energies Eq. (3.34),

$$U_{\text{pot}}(\{\mathbf{m}_i\}) = E_{\text{band}} + \sum_i \mathbf{h}_i \mathbf{m}_i - \frac{1}{4} \sum_i J_i \mathbf{m}_i^2 - \frac{1}{2} \sum_i \bar{U}_i q_i^2. \quad (3.35)$$

The last term is there due to the same consideration in Eq. (3.13). Now we are ready to make a comparison between our model and the phenomenological approach in this subsection. The main results of the two models are listed in



Table 3.1. The main difference between the two models is the choice of different free variables. In our model, the potential energy is defined as a function of exchange fields, and the partition function is defined as an integral in the high-dimensional space of exchange fields. In the constrained magnetic tight binding, the potential energy is a function of atomic magnetic moments, and the partition function is defined as an integral in high-dimensional space of atomic magnetic moments. As the atomic magnetic moments are chosen as free variables in the constrained magnetic tight binding, the constraining fields need to be introduced into the effective Hamiltonian in order to constrain the thermal averages of the spin operators, and the constraining criterion needs to be fulfilled to get a well-defined potential energy as a function of a specific magnetic configuration. In our model, the free variables are the (auxiliary) exchange fields, and the constraining criterion is not involved. As a consequence, our model is easier to solve than the constrained magnetic tight binding.

### 3.6 Summary

We extend magnetic tight binding in order to take into account longitudinal and transverse spin fluctuations that are necessary to describe magnetic transition metals at finite temperature. The original magnetic tight binding is shown to be the magnetic ground-state solution of our model. A comparison between our model and the constrained magnetic tight binding shows that the former is easier to implement.

Table 3.1: Comparison between our model and constrained magnetic tight binding

	our model	constrained magnetic tight binding
free variables	(auxiliary) exchange fields $\mathbf{h}_i$	atomic magnetic moments $\mathbf{m}_i$
partition function	$\int \prod_i d\mathbf{h}_i \exp[-\beta U_{\text{pot}}(\{\mathbf{h}_i\})]$	$\int \prod_i d\mathbf{m}_i \exp[-\beta U_{\text{pot}}(\{\mathbf{m}_i\})]$
potential energy	$E_{\text{band}} + \sum_i \frac{1}{J_i} \mathbf{h}_i^2 - \frac{1}{2} \sum_i U_i \mathbf{q}_i^2$	$E_{\text{band}} + \sum_i \mathbf{h}_i \mathbf{m}_i - \frac{1}{4} \sum_i J_i \mathbf{m}_i^2 - \frac{1}{2} \sum_i U_i \mathbf{q}_i^2$
effective Hamiltonian	$\sum_{i\alpha j\beta\sigma} H_{i\alpha,j\beta}^{(0)} \hat{c}_{i\alpha\sigma}^\dagger \hat{c}_{j\beta\sigma} + 2 \sum_i \mathbf{h}_i \hat{\mathbf{S}}_i + \sum_i \mu_i \hat{n}_i$	$\sum_{i\alpha j\beta\sigma} H_{i\alpha,j\beta}^{(0)} \hat{c}_{i\alpha\sigma}^\dagger \hat{c}_{j\beta\sigma} + 2 \sum_i \mathbf{h}_i \hat{\mathbf{S}}_i + \sum_i \mu_i \hat{n}_i$
self-consistent criterion	$\langle \hat{n}_i \rangle - n_i^0 = \frac{\mu_i}{U_i}$	$\langle \hat{n}_i \rangle - n_i^0 = \frac{\mu_i}{U_i}$
constraining criterion	no	$-2 \langle \mathbf{S}_i \rangle = \mathbf{m}_i$

# Chapter 4

## Accelerated spin-space sampling

In the last chapter, we obtained a model for microscopic interactions in magnetic transition metals. However, there is still one crucial problem to solve before we finish the bridge between the microscopic physical interactions and the macroscopic thermodynamic properties, the sampling of the configurational space. This problem is there because the evaluation of a specific thermodynamic property requires to know a thermal average over the whole configurational space and the analytic procedure is in general not possible. Fortunately, not every point in the configurational space is important to evaluate a given thermodynamic property, and we may employ an importance sampling technique to give a good estimate of its value by drawing a limited number of samples from the configurational space. Different sampling algorithms have different efficiency, and the more efficient the sampling algorithm is, the less samples we need to draw to reach a target precision for an estimation. Our goal in this chapter is to build efficient sampling algorithms for the spin system.

For a spin system in which the longitudinal spin fluctuations are not important, we may define the potential energy  $E$  as a function of the spin configuration  $\{\mathbf{s}_1, \mathbf{s}_2 \dots \mathbf{s}_N\}$ , where  $\mathbf{s}_i$  is the unit spin vector of atom  $i$ . Finite-temperature properties are then investigated using Boltzmann statistics,

$$\langle O \rangle = \int \prod_i d\mathbf{s}_i \pi(\{\mathbf{s}_i\}) O(\{\mathbf{s}_i\}), \quad (4.1)$$

with the normalized configurational probability density in spin space,

$$\pi(\{\mathbf{s}_i\}) = \frac{1}{Z_{\text{TSF}}} \exp[-\beta E(\{\mathbf{s}_i\})], \quad (4.2)$$

where  $\beta = 1/(k_B T)$  with the temperature  $T$ .  $O$  may be any spin-dependent observable, and  $Z^{\text{TSF}}$  is the partition function in the classical limit.

For a spin system in which the longitudinal spin fluctuations are crucial, e.g., Ni [111], we need to include the longitudinal degrees of freedom into the spin configuration and define a potential energy surface  $E(\{\mathbf{h}_1, \mathbf{h}_2 \dots \mathbf{h}_N\})$  in our model or  $E(\{\mathbf{m}_1, \mathbf{m}_2 \dots \mathbf{m}_N\})$  in others's work [28, 86, 111], where  $\mathbf{h}_i$  and  $\mathbf{m}_i$  are the exchange field and the atomic magnetic moment of atom  $i$ . Although the free variables  $\mathbf{m}_i$  and  $\mathbf{h}_i$  are different, we can use the same algorithms to sample them as physically they both represent microscopic magnetic configurations and mathematically they are both three-dimensional vectors. Therefore, from now on we do not differentiate between  $\mathbf{h}_i$  and  $\mathbf{m}_i$  in this chapter. In this case, finite-temperature properties are determined via

$$\langle O \rangle = \int \prod_i d\mathbf{m}_i \pi(\{\mathbf{m}_i\}) O(\{\mathbf{m}_i\}), \quad (4.3)$$

and the normalized configurational probability density is now defined as

$$\pi(\{\mathbf{m}_i\}) = \frac{1}{Z} \exp[-\beta E(\{\mathbf{m}_i\})]. \quad (4.4)$$

We put the focus of this chapter on the development of efficient Hamiltonian MC algorithms [34, 98] for the transverse spin-fluctuation model Eq. (4.1) due to the following considerations:

- Although the full spin-fluctuation model Eq. (4.3) is more complicated than the transverse spin-fluctuation model Eq. (4.1), it is actually easier and more straightforward to employ Hamiltonian MC on the former as the free variables  $\mathbf{m}_i$  in Eq. (4.3) have the same mathematical properties with the atomic positions in the conventional Hamiltonian MC whereas the free variables in the latter should be constrained on a unit sphere.
- The transverse spin-fluctuation model is till now one of the most widely-used models to study finite-temperature properties of magnetic materials [5, 29, 30, 71, 89, 99, 121, 127]. In spite of its popularity, an efficient sampling algorithm of general applicability is still missing, and we will discuss about this in detail in section 4.1.

The material in the following has been published in our paper in Physical Review B [132] and is reused under the license number RNP/19/OCT/019547.

## 4.1 Introduction

Frequently, model Hamiltonians are used for evaluating spin-dependent observables, such as the rigid-lattice Heisenberg model or its coordinate-dependent variants that account for spin-lattice coupling [89]. For materials design it would be desirable to work with material specific Hamiltonians that explicitly take into account the electronic structure. This would also facilitate an adequate treatment of spin fluctuations in itinerant-electron magnets [94], complex exchange-interactions in Fe [79] and magnon-phonon coupling in magnetic transition metals [73]. Recent years have seen significant progress in the development of electronic-structure based models, e.g., density functional theory for non-collinear magnetism [57, 77, 78, 87, 105, 121], non-collinear magnetic tight-binding [11, 96] or bond-order potentials [31, 33, 43, 44].

For model Hamiltonians there are many Monte Carlo (MC) sampling algorithms that efficiently sample the spin space, but unfortunately none of them is suitable for electronic-structure based models. We notice that there are three main differences between model Hamiltonians and electronic-structure based models. First, model Hamiltonians, at least most of them, contain only pair-wise interactions, while electronic-structure based models require many-spin interactions. Second, the range of the interaction is different. In model Hamiltonians typically only first and second nearest-neighbour interactions are taken into account, while in principle all spins are coupled in electronic-structure based models. Third, electronic-structure based models are orders of magnitude slower in the evaluation of the Hamiltonian. These differences prohibit application of many efficient MC algorithms. For example, the checkerboard MC algorithm [103] is not applicable to electronic-structure based models as the system cannot be decomposed into non-interacting sublattices and the checkerboard-decomposition method is not applicable. The Swendsen-Wang [124] and Wolff [135] cluster algorithms significantly reduce the correlation of samples, but they only work for models which may be mapped onto percolation models, which is difficult for electronic-structure based models. The over-relaxation [20, 26] algorithm works well for the classical Heisenberg model, but its efficient implementation depends upon the checkerboard-decomposition method [80]. The heat-bath spin dynamics [85, 127] might be seen as a variant of the over-relaxation algorithm and suffers from the same problem.

The Wang-Landau sampling [131] can in principle overcome the critical slowing-down, but the convergence of the density of states usually requires millions of energy evaluations, which is not affordable for electronic-structure based methods. In a recent application of the Wang-Landau sampling to first-principle non-collinear magnetism 590,000 energy evaluations were performed yielding a reasonable estimate of the density of states [37], but despite the huge computational effort the results could not be fully converged.

Our work builds on recent progress in Hamiltonian MC [17–19, 47, 58, 98, 133] and efficient methods to accelerate first-principles thermodynamic calculations [36, 48, 55]. For the former, a rigorous theoretical proof has been given that underpins the empirical success of Hamiltonian MC [19] and the theoretical considerations [17] and techniques [18, 58, 98, 133] developed for the automatic tuning of its hyper-parameters. In the latter, effective potentials are employed to speed up first-principles thermodynamic calculations, as direct calculations with first-principles methods are too expensive. However, the conventional Hamiltonian MC algorithm is not applicable to spin systems as the spin length is not preserved in standard molecular dynamics that is used in Hamiltonian MC. The effective-potential methods in literature [36, 48, 55] are designed to accelerate calculations of free energies and cannot be applied to evaluate other thermodynamic quantities straightforwardly. These considerations form the basis for the methods developed in this work. First, we propose an auxiliary spin-dynamics as a basis for a Hamiltonian MC algorithm for spin systems that rigorously preserves spin lengths. Second, we propose a Hamiltonian MC framework in which the temperature-dependent spin-cluster expansion (SCE) [29, 30] is used as an auxiliary model to further accelerate the sampling of the spin space.

We first introduce the Hamiltonian MC algorithm for spin systems using auxiliary spin-dynamics, and discuss the automatic tuning of its hyper-parameters. Then we introduce the temperature-dependent SCE as an auxiliary model to accelerate the sampling of the spin space. In Sec. 4.3, we employ the classical Heisenberg model to demonstrate the efficiency of our method, and apply our algorithm to sample the magnetic phase transition in bcc iron with magnetic bond-order potentials [33, 44, 95].

## 4.2 Methodology

Our target is to draw efficiently independent samples according to the configurational probability density defined in spin space. To this end we extend Hamiltonian Monte Carlo (HMC) [19, 98] for the sampling of spin space variables. HMC does not sample the configurational distribution directly but a joint distribution of positions  $q$  and momenta  $p$ ,

$$\pi(q, p) = \frac{1}{Q} \exp[-\beta \mathcal{H}(q, p)], \quad (4.5)$$

where  $Q$  is the partition function in the phase space. The marginal distribution of  $q$  then restores the target distribution.

For sampling spin space using HMC we introduce auxiliary spin angular velocities  $\boldsymbol{\omega}_i$  as canonical variables of the spin directions  $\{\boldsymbol{\omega}, \mathbf{s}\}$  in formal analogy to the classical canonical variables  $\{\mathbf{p}, \mathbf{q}\}$  and define the Hamiltonian as

$$\mathcal{H} = \frac{I}{2} \sum_i \boldsymbol{\omega}_i^T \cdot \boldsymbol{\omega}_i + E(\{\mathbf{s}_i\}), \quad (4.6)$$

where  $I$  is a fictitious mass that later is used as a parameter to optimize the efficiency of the HMC sampling.

The configurational probability density in spin space, Eq. (4.2), is restored by the marginal distribution of the configurational variables in phase space,

$$\pi(\{\mathbf{s}_i\}) = \int \prod_i d\boldsymbol{\omega}_i \pi(\{\boldsymbol{\omega}_i, \mathbf{s}_i\}), \quad (4.7)$$

with the joint probability density defined as

$$\pi(\{\boldsymbol{\omega}_i, \mathbf{s}_i\}) = \frac{1}{Q} \exp[-\beta \mathcal{H}(\{\boldsymbol{\omega}_i, \mathbf{s}_i\})]. \quad (4.8)$$

Different from usual spin dynamics, which is based on a first order differential equation in time [9, 46, 89]

$$\frac{d\mathbf{s}_i}{dt} = \frac{\gamma_e}{m_i} \frac{\partial E}{\partial \mathbf{s}_i} \times \mathbf{s}_i, \quad (4.9)$$

where  $m_i$  is the magnitude of magnetic moments, and  $\gamma_e$  is the gyromagnetic ratio for an electron spin, the auxiliary Hamiltonian, Eq. (4.6), dictates that the spins

follow conventional Hamiltonian dynamics for rigid bodies

$$\begin{aligned} I \frac{d\boldsymbol{\omega}_i}{dt} &= \frac{\partial E}{\partial \mathbf{s}_i} \times \mathbf{s}_i, \\ \frac{d\mathbf{s}_i}{dt} &= \boldsymbol{\omega}_i \times \mathbf{s}_i. \end{aligned} \tag{4.10}$$

It is evident that the spin dynamics described by Eq. (4.9) and Eq. (4.10) is different. Eq. (4.10) describes a completely fictitious dynamics of the spins that, however, by construction may be used to sample spin space according to the probability density  $\pi(\{\mathbf{s}_i\})$ . We denote Eq. (4.9) as the semi-classical spin dynamics and Eq. (4.10) as the auxiliary spin-dynamics in this paper.

While it is very difficult or impossible to find an effective symplectic time-reversible integrator for the semi-classical spin dynamics [76, 91], this is not a problem for the auxiliary spin-dynamics. We combine the velocity Verlet method [125] and a spin rotation scheme to obtain an efficient numerical integration algorithm that is time-reversible, area-preserving and preserves spin length. There are three steps per update,

$$\begin{aligned} \tilde{\boldsymbol{\omega}}_i^{t+1} &= \boldsymbol{\omega}_i^t + \frac{1}{2} \frac{\epsilon}{I} \cdot \frac{\partial E}{\partial \mathbf{s}_i^t} \times \mathbf{s}_i^t, \\ \mathbf{s}_i^{t+1} &= \mathbf{D}(\tilde{\boldsymbol{\omega}}_i^{t+1}, \epsilon) \cdot \mathbf{s}_i^t, \\ \boldsymbol{\omega}_i^{t+1} &= \tilde{\boldsymbol{\omega}}_i^{t+1} + \frac{1}{2} \frac{\epsilon}{I} \cdot \frac{\partial E}{\partial \mathbf{s}_i^{t+1}} \times \mathbf{s}_i^{t+1}, \end{aligned} \tag{4.11}$$

where the index  $i$  denotes spin,  $t$  the current state and  $t + 1$  the next state.  $\epsilon$  is the time step, and  $\mathbf{D}(\tilde{\boldsymbol{\omega}}_i^{t+1}, \epsilon)$  is a  $3 \times 3$  rotation matrix [101],

$$\mathbf{D}(\tilde{\boldsymbol{\omega}}_i^{t+1}, \epsilon) = \mathbf{I} + \mathbf{W}_i^{t+1} \sin(\omega_i^{t+1} \epsilon) + (\mathbf{W}_i^{t+1})^2 [1 - \cos(\omega_i^{t+1} \epsilon)]. \tag{4.12}$$

$\omega_i^{t+1}$  is the magnitude of  $\tilde{\boldsymbol{\omega}}_i^{t+1}$ , and  $\mathbf{W}_i^{t+1}$  is a skew - symmetric matrix with  $\mathbf{W}_{i,XY}^{t+1} = -\hat{\omega}_{i,Z}^{t+1}$ ,  $\mathbf{W}_{i,XZ}^{t+1} = \hat{\omega}_{i,Y}^{t+1}$ ,  $\mathbf{W}_{i,YZ}^{t+1} = -\hat{\omega}_{i,X}^{t+1}$ , where  $\hat{\boldsymbol{\omega}}_i^{t+1}$  is the directional vector of  $\tilde{\boldsymbol{\omega}}_i^{t+1}$ .  $X$ ,  $Y$  and  $Z$  denote Cartesian components.

We may now employ standard HMC for sampling the spin space probability density  $\pi(\{\mathbf{s}_i\})$  on the basis of the auxiliary spin-dynamics. There are three steps per MC update. The first step performs a Gibbs sampling of angular velocities, in which we fix the configurational variables  $\{\mathbf{s}_i\}$  and sample the angular velocities according to their conditional, Gaussian distribution. In the second step the auxiliary spin-dynamics is run for a specific trajectory of length  $L$ . In the third step



the Metropolis-Hastings acceptance-rejection is performed for the proposal state generated by auxiliary spin-dynamics in order to guarantee detailed balance. The acceptance probability is given by

$$p^{\text{acc}}(\mathbf{x}_{\text{new}}|\mathbf{x}_{\text{old}}) = \min \{1, \exp(-\beta\Delta\mathcal{H}_{\text{old}\rightarrow\text{new}})\}, \quad (4.13)$$

where  $\mathbf{x}_{\text{old}}$  and  $\mathbf{x}_{\text{new}}$  are the state variables containing both the spins and the angular velocities. Repeating the three steps above leads to a Markov chain which obeys the joint distribution and is used to evaluate thermal averages.

There are three hyper-parameters in our algorithm, the mass  $I$ , the time-step  $\epsilon$  for numerical integration and the trajectory length  $L$ . They have no effect on the accuracy of the MC sampling but strongly influence the efficiency and in practical applications should be set automatically without user intervention. We adapt the time step such that the exponential moving average of the acceptance probability is in the range from 0.6 to 0.7, which is centered around the optimal value 0.651 suggested by Beskos et al. [17]. More specifically, we compute the exponential moving average of the acceptance probability at each step. If it is smaller (larger) than 0.6 (0.7), the time step is decreased (increased) by a specific factor. For the tuning of the trajectory length  $L$ , we employ an empirical termination criterion, the U-turn termination [58], which is an empirical estimate for the optimal length of Hamiltonian dynamics per MC step. The basic idea is to maximize the squared distance between the initial and final states. Its implementation in this work is slightly different from the one in the original paper as we do not use standard molecular dynamics. We first define the half squared distance for spin systems,

$$\Delta(t) = \frac{1}{2} \sum_i [\mathbf{s}_i(t) - \mathbf{s}_i(0)]^T \cdot [\mathbf{s}_i(t) - \mathbf{s}_i(0)]. \quad (4.14)$$

The U-turn termination criterion is then derived according to,

$$\frac{d\Delta}{dt} < 0, \quad (4.15)$$

and given as,

$$\sum_i [\mathbf{s}_i(t) - \mathbf{s}_i(0)]^T \cdot [\boldsymbol{\omega}_i(t) \times \mathbf{s}_i(t)] < 0, \quad (4.16)$$

where the equations of motion, Eq. (4.10), are employed.

The hyper-parameters are only tuned in the warm-up phase and then fixed to leave the distribution function invariant in the sampling phase. We fix the mass  $I$  to  $1 \text{ eVfs}^2$  in our work, which is an empirical optimal value according to our tests.

We denote the HMC based on auxiliary spin-dynamics Algorithm I in this paper. We next incorporate the temperature-dependent SCE into Algorithm I to further accelerate the sampling for expensive spin models and denote the new method Algorithm II. This is based on the observation that the auxiliary spin-dynamics is only used to generate the proposal state and may be run with a cheaper auxiliary model instead of the expensive target one. This leaves the sampling correct as long as the detailed balance is guaranteed for the target model through the Metropolis-Hastings acceptance-rejection. The criterion for the auxiliary model is that it should be as close to the target one as possible since the acceptance probability is now determined by the difference between auxiliary and target models,

$$\begin{aligned}
p^{\text{acc}}(\mathbf{x}_{\text{new}}|\mathbf{x}_{\text{old}}) &= \min \left[ 1, \exp \left( -\beta \Delta \mathcal{H}_{\text{old} \rightarrow \text{new}}^{\text{target}} \right) \right] \\
&= \min \left[ 1, \exp \left( \beta \Delta \mathcal{H}_{\text{old}}^{\text{auxiliary} \rightarrow \text{target}} \right) \times \right. \\
&\quad \exp \left( -\beta \Delta \mathcal{H}_{\text{old} \rightarrow \text{new}}^{\text{auxiliary}} \right) \times \\
&\quad \left. \exp \left( -\beta \Delta \mathcal{H}_{\text{new}}^{\text{auxiliary} \rightarrow \text{target}} \right) \right].
\end{aligned} \tag{4.17}$$

In Eq. (4.17), the first and last exponentials contain the energy difference between the auxiliary and the target model for the old and new states, respectively. The second exponential arises from the numerical error of the integration of the auxiliary spin-dynamics with the auxiliary model, which is typically a small contribution.

For spin systems, an ideal auxiliary model is the spin-cluster expansion [29, 30] which may be fitted to accurately reproduce the target model. Here we propose to generate temperature-dependent SCEs due to two considerations. First, only a specific area in the spin space is explored with high probability at a given temperature, as shown in Fig. 4.1, where we plot the magnetization and the potential energy of spin configurations at different temperatures for a classical ferromagnetic Heisenberg model. Clearly, the configurations at different temperatures are clustered into specific areas. This locality makes it easier to fit a temperature-dependent effective potential. Second, the temperature dependence of the exchange parameters is inherited in some models, e.g., in spin-density-functional-theory for itinerant-electron

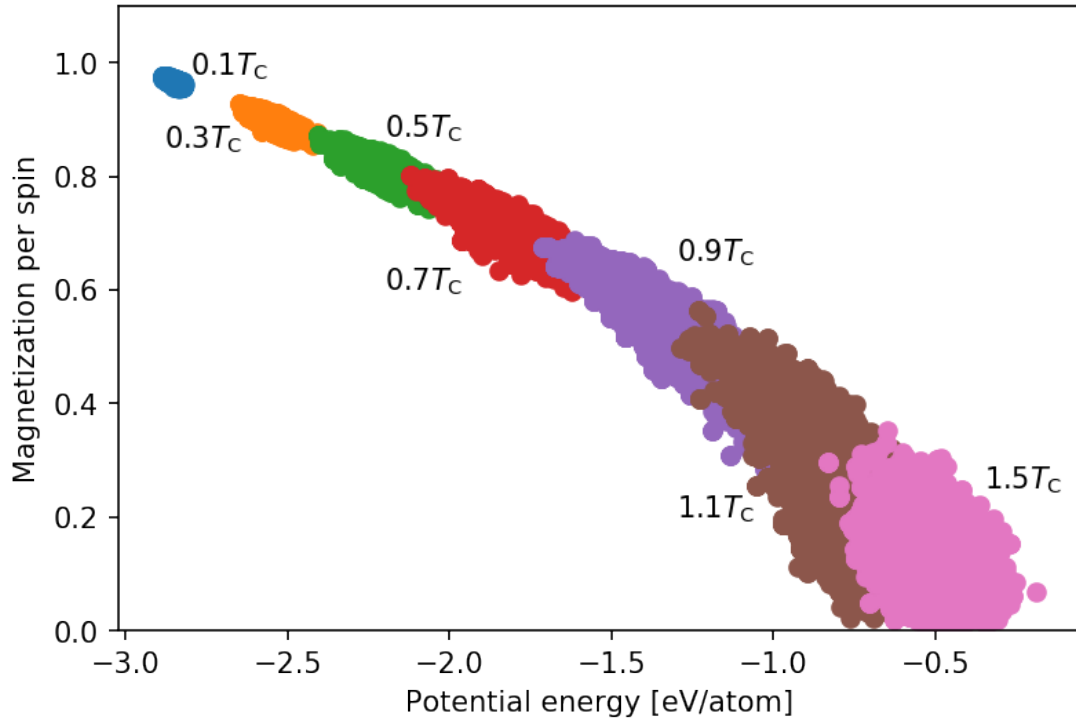


Figure 4.1: Magnetization-energy plot for spin configurations of a  $6 \times 6 \times 6$  simple cubic lattice at different temperatures. The classical ferromagnetic Heisenberg model is employed in this test.  $T_C$  is its Curie temperature. The exchange parameter  $J$  is chosen to be 1 eV.

magnets [110]. In practice, we collect the spin configurations in the warm-up phase and fit the temperature-dependent SCE at different temperatures separately. The extra cost required for fitting the temperature-dependent SCEs is normally negligible compared to the total computational time for sampling. The auxiliary spin-dynamics is then run with the temperature-dependent SCE to generate proposal states while the Metropolis-Hastings acceptance-rejection is performed for the target models in order to guarantee correct sampling. We note that no gradient calculations for the electronic-structure based models are required in this algorithm as the auxiliary spin-dynamics is run with the temperature-dependent SCE, which is another advantage of our method since the evaluation of gradients usually requires considerable extra computational cost.

## 4.3 Results and Discussion

We demonstrate two applications in this section. In the first application, we perform efficiency tests for Algorithm I using the classical Heisenberg model. In the second application, we test and discuss Algorithm II using magnetic bond-order potentials [31, 33, 43, 44].

### 4.3.1 Application to the classical Heisenberg model

We first employ the classical ferromagnetic Heisenberg model,

$$E = -J \sum_{\langle ij \rangle} \mathbf{s}_i \cdot \mathbf{s}_j, \quad (4.18)$$

on a simple cubic lattice to perform an efficiency test for Hamiltonian MC, Algorithm I.  $J$  is the exchange parameter, and  $\langle ij \rangle$  denotes the first-nearest-neighbour pairs without double counting.  $J$  is chosen to be 1 eV in this test.

In Fig. 4.2, we measure the warm-up efficiency for a  $6 \times 6 \times 6$  simple cubic lattice from the high (low)-energy to low (high)-energy states. As expected, the efficiency from low-energy to high-energy states is higher than the other way round, and the former (latter) takes around 400 (1200) gradient calls.

We next fix the temperature to the critical temperature of the 3D classical Heisenberg model ( $T_C = 1.4459 J/k_B$ ) [103], and estimate the dynamical critical exponent. The estimation is based on the dynamical finite-size scaling ansatz [123]

$$\tau \approx L^z, \quad (4.19)$$

where  $L$  is the side length of the cubic simulation cell.  $\tau$  is the relaxation time of magnetization and evaluated according to

$$\phi(t) = Ae^{-t/\tau}, \quad (4.20)$$

where  $\phi(t)$  is the time auto-correlation function of magnetization. The relaxation time  $\tau$  is measured in units of gradient calls instead of MC step as multiple gradient calls may be required for one MC step. In Fig. 4.3, we show the log-log plot for the relaxation time versus the side length of the cubic simulation cell. The dynamical critical exponent is estimated to be around 2.23. This value is comparable to that of the checkerboard MC algorithm (1.96, cf. Ref. [103]), but cannot compete

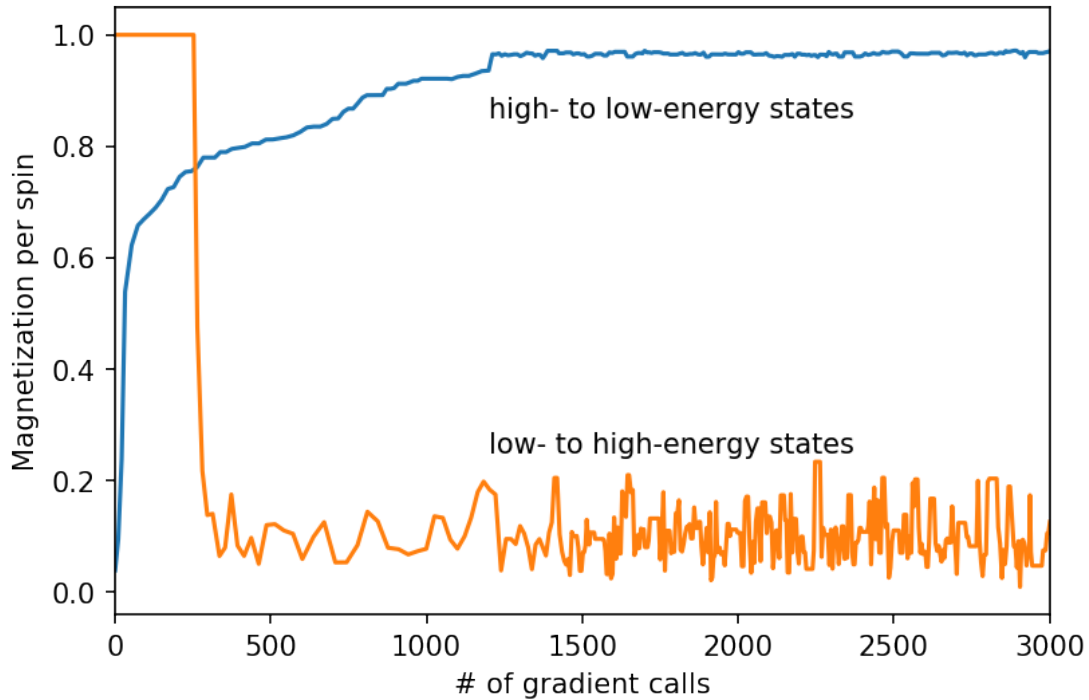


Figure 4.2: Evolution of the magnetization of a  $6 \times 6 \times 6$  simple cubic lattice for the classical Heisenberg model in the warm-up phase. Orange line: the initial state is the ferromagnetic ground state and the temperature is  $2 T_C$ . Blue line: the initial state is a random-spin state and the temperature is  $0.1 T_C$ .

with the cluster algorithms whose relaxation times are almost independent of the size [60]. However, as we discussed in the introduction, these algorithms are only applicable for a small group of spin models, whereas Hamiltonian MC is generally applicable.

### 4.3.2 Application to electronic-structure based models

Next, we employ the magnetic bond-order potential (BOP) [33, 44, 95] to demonstrate the application of our algorithm with an auxiliary model, Algorithm II. In algorithm I, we need to run both MC and auxiliary spin-dynamics with the target model, which requires too many energy and gradients calls to converge thermal averages for electronic-structure based models. A trajectory length of more than ten is usually needed in auxiliary spin-dynamics in order to decorrelate the current and the proposal state. The computational cost of this part can be

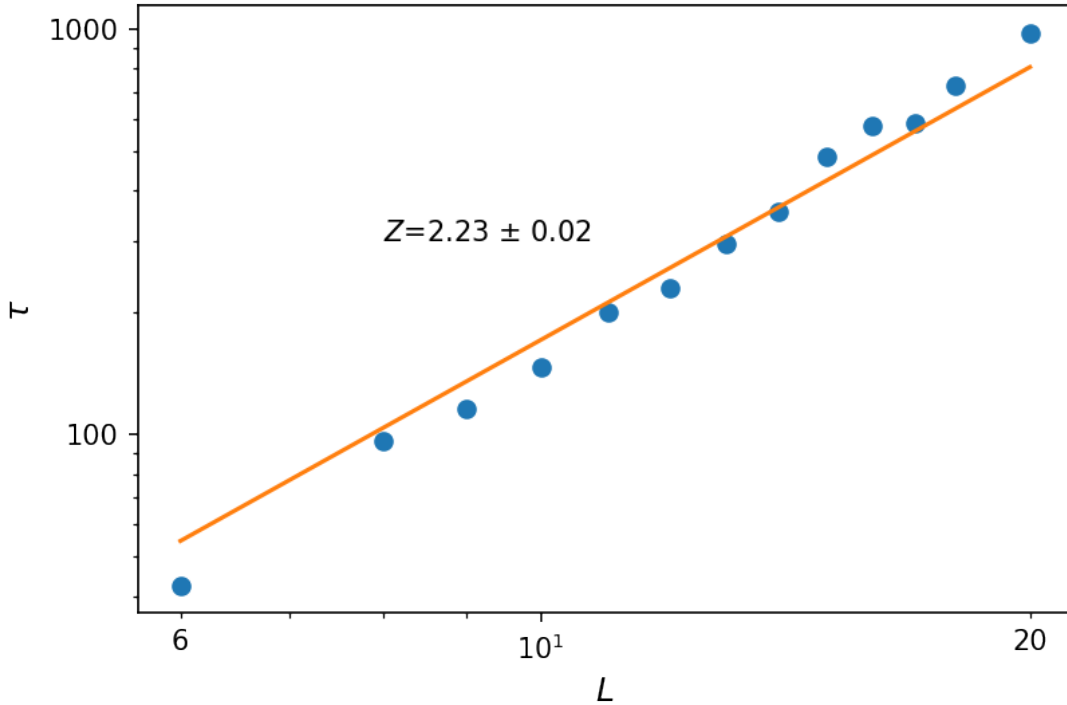


Figure 4.3: Log-log plot of the relaxation time for the magnetization in units of gradient calls.  $L$  represents the side length of the cubic simulation cell and  $\tau$  represents the relaxation time. The error bars of the relaxation time are smaller than the symbol size. The classical Heisenberg model on the simple cubic lattice is used here.

dramatically reduced with algorithm II in which the auxiliary spin-dynamics is run with a temperature-dependent SCE. As the temperature-dependent SCE is orders of magnitude faster than the electronic-structure based models, this gives a significant speed-up.

The magnetic BOP is one of the simplest electronic-structure based models for magnetic transition metals. In this model, the potential energy is based on the electronic density of states. It is given as a function of atomic positions and spin orientations,

$$E(\{\mathbf{r}_i, \mathbf{s}_i\}) = U_{\text{bond}} + U_{\text{trans}} + U_{\text{rep}} + U_{\text{C}} + U_{\text{X}} + U_{\text{ext}}, \quad (4.21)$$

where  $U_{\text{bond}}$  is the bond energy,  $U_{\text{trans}}$  the electron transfer energy,  $U_{\text{rep}}$  the repulsion energy,  $U_{\text{C}}$  the Coulomb energy,  $U_{\text{X}}$  the exchange energy, and  $U_{\text{ext}}$  the

external energy. Readers are referred to Ref. [33] for a detailed discussion of this model.

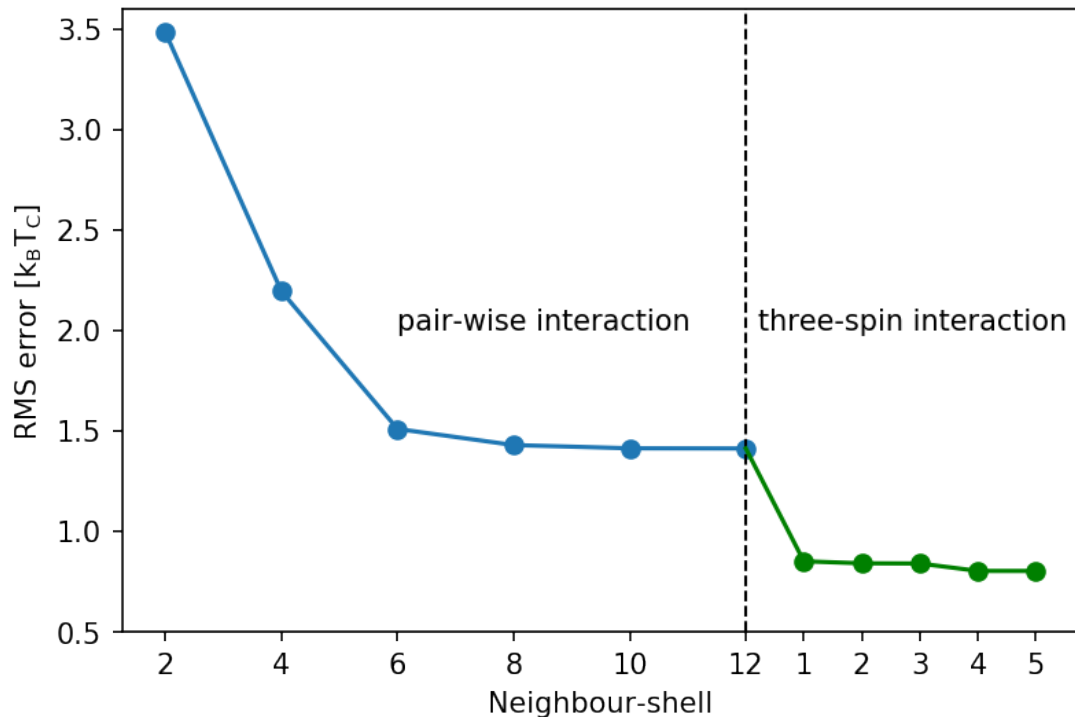


Figure 4.4: Root-mean-squared (RMS) error of the spin-cluster expansion model plotted as a function of neighbour shells for pair-wise and three-spin interactions. The RMS error per cell is in the unit of  $k_B T_C$ , where  $T_C$  is the experimental Curie temperature of iron (1043 K). The spin-cluster expansion model is fitted for the potential energy of a magnetic BOP for  $5 \times 5 \times 5$  bcc lattice of iron.

The magnetic BOP gives a robust description of ferromagnetism, and more importantly, the real-material properties such as phase stability, elastic constants, and dislocations are described properly [43, 44, 95]. More specifically, we use the 9-moments magnetic BOP of iron by Mrovec et al. [95] and the implementation in the BOPfox code [?] to calculate potential energies for spin configurations in the bcc lattice. The  $5 \times 5 \times 5$  simulation cell contains 250 spins, and the atomic positions are fixed. We employ a temperature-dependent SCE fitted for the BOP of iron as an auxiliary model to run the auxiliary spin-dynamics. As shown in Eq. (4.17), the energy difference between the electronic-structure based model and the auxiliary model should be as small as possible to guarantee a good acceptance

probability. A rough estimation can be given for the relationship between the root-mean-squared (RMS) error  $\Delta E_{\text{RMS}}$  and the average acceptance probability  $\bar{p}^{\text{acc}}$ ,

$$\bar{p}^{\text{acc}} \approx \frac{1}{2} [1 + \exp(-\beta \Delta E_{\text{RMS}})]. \quad (4.22)$$

For example, a RMS error of one  $k_{\text{B}}T$  corresponds to an average acceptance probability of around 0.68, which is a good value for MC acceptance-rejection.

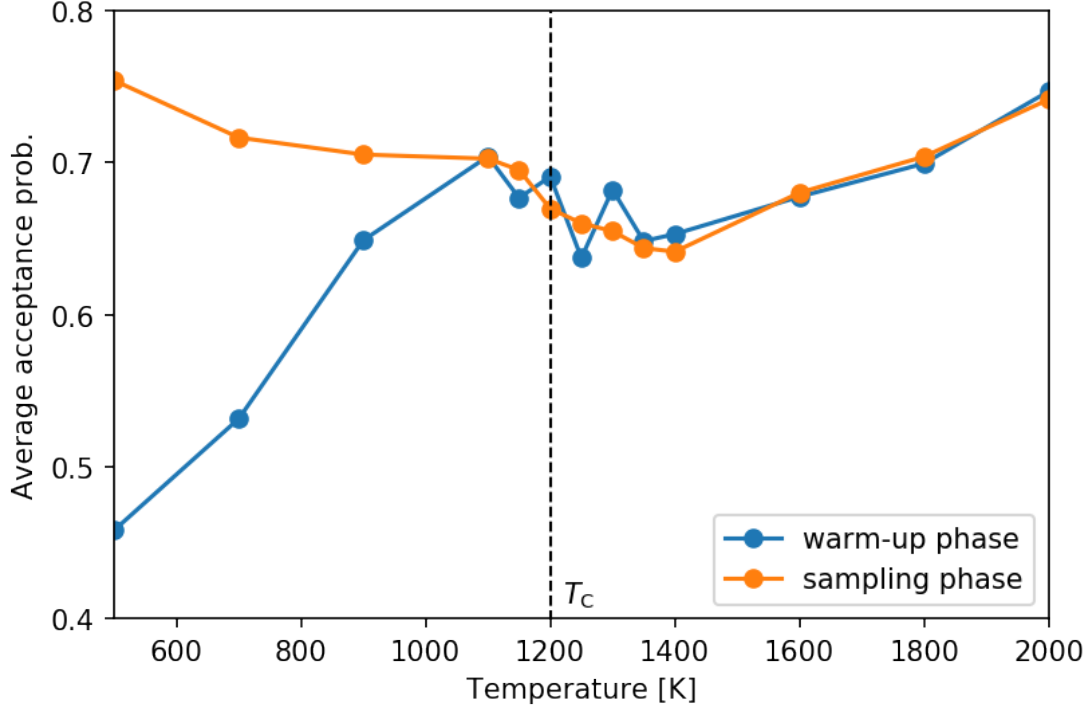


Figure 4.5: Average acceptance probability in the warm-up and the sampling phases. The temperature-independent spin cluster expansion is used in the warm-up phase while the temperature-dependent one used in the sampling phase. The magnetic BOP of iron is the target model in this test, with  $5 \times 5 \times 5$  bcc lattice of 250 spins.

In Fig. 4.4, we show a typical plot for the RMS error versus neighbour shells of pair-wise and three-spin interactions. The pair-wise spin clusters are not sufficient to reduce the root-mean-squared (RMS) error to less than one  $k_{\text{B}}T_{\text{C}}$  and three-spin interactions are taken into account in order to further reduce the RMS error to  $0.80 k_{\text{B}}T_{\text{C}}$ . In practice, we include pair-wise interactions up to the sixth nearest-neighbour shell and the first-nearest-neighbour three-spin interactions in



our temperature-dependent SCE. The two-spin and three-spin interactions are sufficient to converge the SCE for the ideal lattice with fixed atomic positions that is used in this work. Breaking the geometric degeneracy by, e.g., vibrations or defects, will introduce distance- and environment-dependent interaction terms which rule the convergence of the SCE much more difficult or even intractable.

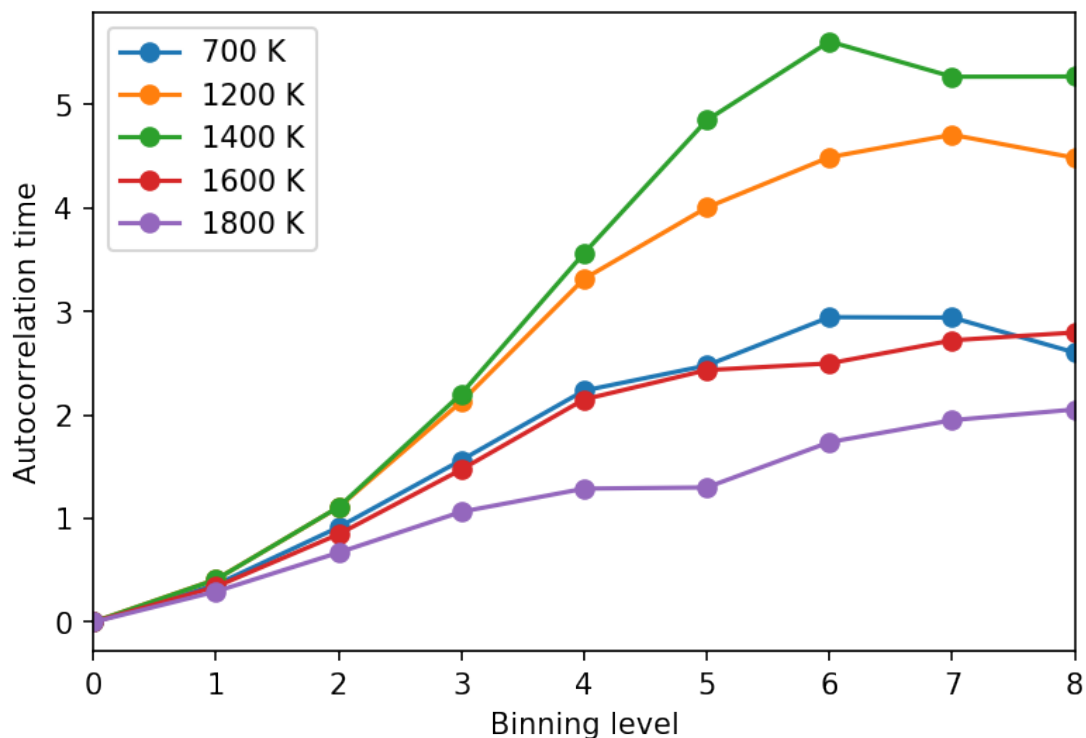


Figure 4.6: Binning analysis for potential energies of  $5 \times 5 \times 5$  bcc lattice at different temperatures.

In practice, we first fit a temperature-independent SCE as a start-up auxiliary model. This involves 1000 spin configurations generated with the classical Heisenberg model at the critical point and the corresponding potential energies for electronic-structure based models (magnetic bond-order potential in our application). The warm-up phase is split into two stages. In the first stage, the system is thermalized purely with the start-up auxiliary model and the length is set to 1000 MC steps. The time-step and the trajectory length are automatically tuned with the methods in Section 4.2. In the second stage, the start-up model is used to run auxiliary spin-dynamics while the Metropolis-Hastings acceptance-rejection is

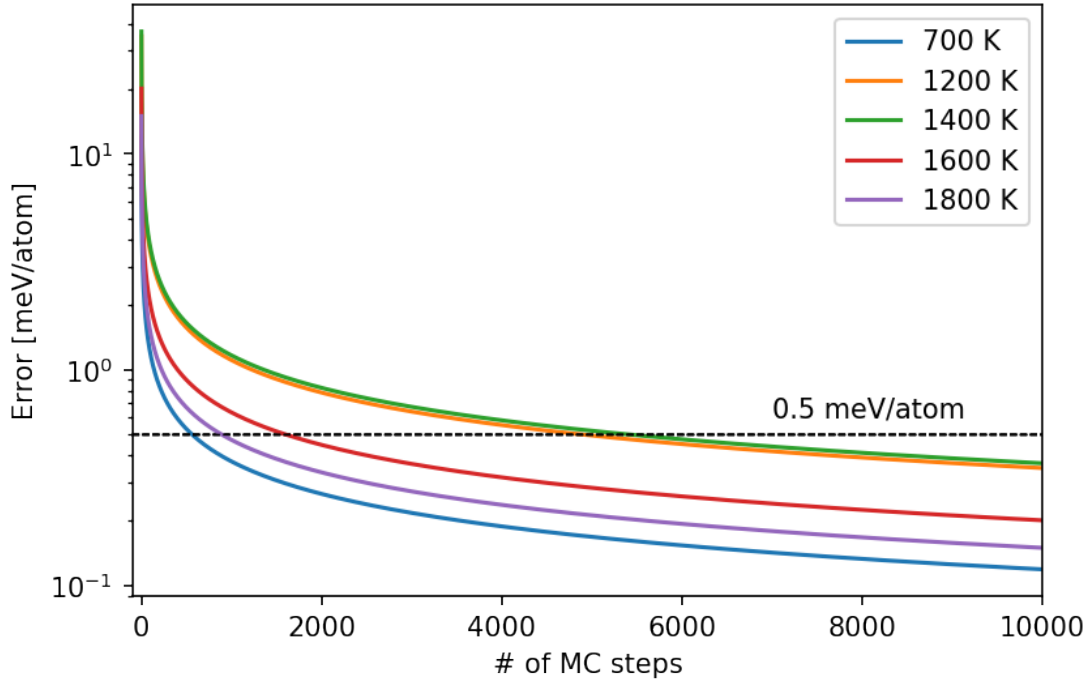


Figure 4.7: Running errors in the estimation of thermal averages of potential energies at different temperatures.

performed for the target electronic structure based models. The time-step is further tuned while the trajectory length is fixed to the mean value in the first stage. In our implementation for the magnetic bond-order potential, a typical time step is around 0.3 fs, and a typical trajectory length is around 18. The length of the second stage is set to be 500 MC steps. Once the warm-up phase is finished, we collect all the spin configurations and the potential energies in the second stage to fit a temperature-dependent SCE with least-squares fitting, which is then used to run auxiliary spin-dynamics in the sampling phase. Both the time-step and the trajectory length are fixed in this phase. We use 10,000 MC steps to evaluate thermal averages, which are sufficient to guarantee convergence due to the small autocorrelation time in our algorithm.

In Fig. 4.5, we show the average acceptance probability at different temperatures in both the warm-up and sampling phase. It is higher in the sampling phase than in the warm-up phase as the temperature-dependent SCE reproduces the energy landscape of the BOP better, as discussed in Sec. 4.2.

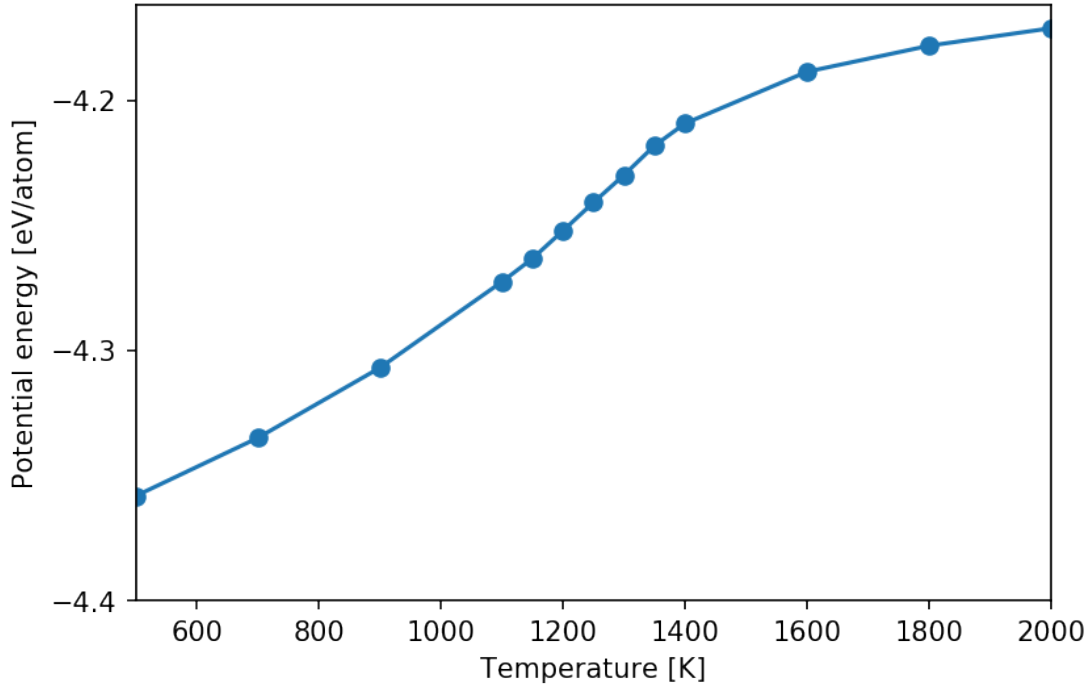


Figure 4.8: Thermal-average potential energy as a function of temperature for  $5 \times 5 \times 5$  bcc lattice of iron obtained with a magnetic bond-order potential.

We performed a binning analysis [8] for the potential energy to check the convergence. As shown in Fig. 4.6, the autocorrelation times at all temperatures reach a plateau, which indicates that the calculation is fully converged. The autocorrelation times range from two to six depending on the temperature. The running error can be estimated according to [8]

$$\Delta_O = \sqrt{\frac{\text{Var}O}{N}(1 + 2\tau_O)}, \quad (4.23)$$

where  $O$  is the observable,  $\text{Var}O$  its variance,  $\tau_O$  its autocorrelation time, and  $N$  the number of MC steps. Based on this, we plot in Fig. 4.7 the running errors in the estimation of thermal averages of potential energies at different temperatures. Clearly, more MC steps are required to reach convergence at temperatures closer to the critical point (1200 K in this case, as shown later) as the variance is larger. For our algorithm, an error of 0.5 meV/atom can be reached within 5000 MC steps. This excellent efficiency is due to the short autocorrelation time, as already discussed.

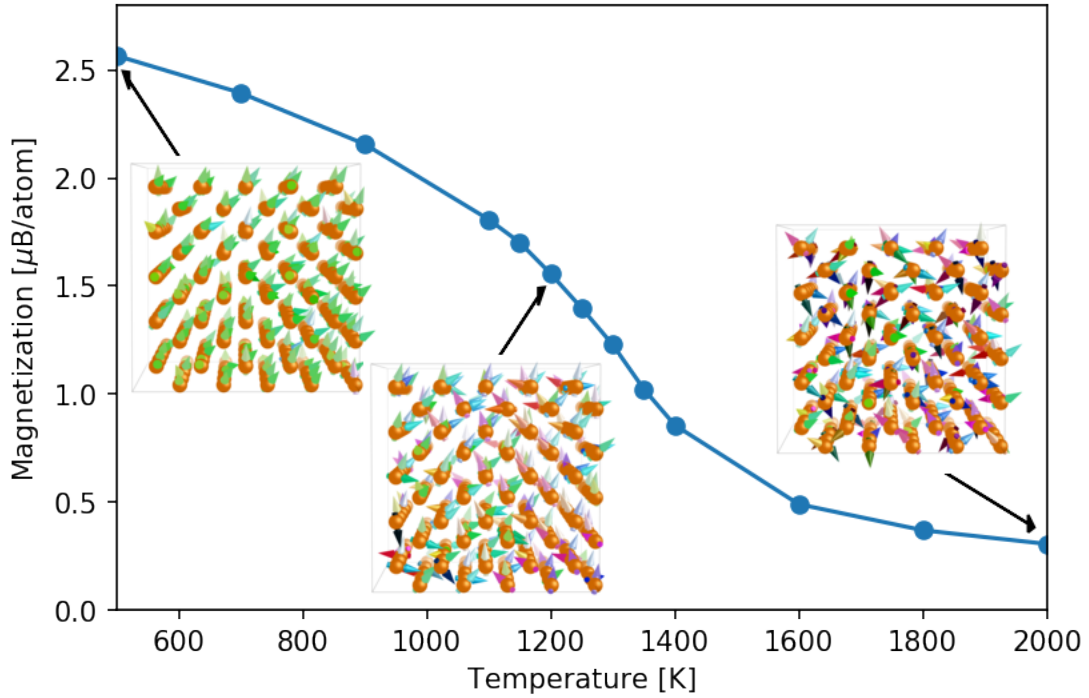


Figure 4.9: Magnetization as a function of temperature for  $5 \times 5 \times 5$  bcc lattice of iron obtained with a magnetic bond-order potential. The images are snapshots of spin configurations at 500 K, 1200 K, and 2000 K, respectively, which are generated with the code `V_sim` [2]. The spin directions are indicated by the arrows and the coloration. We see the collapse of the long- and short-range magnetic orders with increasing temperatures.

The thermal-average potential energy, the magnetization, and the magnetic contribution to the specific heat of bcc iron for magnetic BOP are plotted as a function of temperature in Fig. 4.8, Fig. 4.9, and Fig. 4.10, respectively. The magnetization curve we obtain here has similar features to that of the classical Heisenberg model [72, 86], which indicates that the exchange parameters are not influenced considerably by spin fluctuations in magnetic iron. We notice that there is a recent paper by Ruban and Peil [112] who found that the exchange parameters are significantly influenced by atomic vibrations in magnetic iron. This effect is not considered here as we fix atomic positions in our simulation. There is residual magnetization up to 2000 K due to the finite-size effect. Based on the magnetic contribution to the specific heat (see Fig. 4.10), we estimate the Curie temperature to be around 1200 K, which is close to the experimental value (1043 K). The

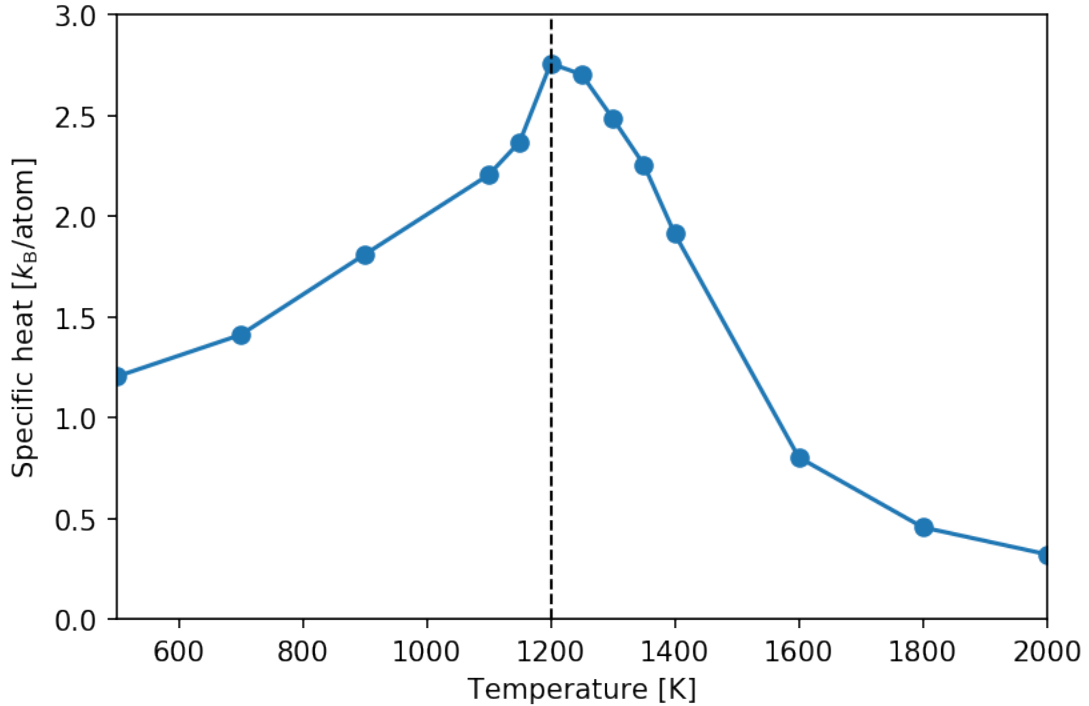


Figure 4.10: Magnetic contribution to the specific heat as a function of temperatures for  $5 \times 5 \times 5$  bcc lattice of iron for magnetic bond-order potentials.

difference in  $T_C$  is attributed to the neglect of magnon-phonon coupling [112] and limitations of the parametrization of the magnetic BOP used here. To our knowledge, this is the first result for direct and high-fidelity simulations of the magnetic phase transition of bcc iron with an electronic-structure based model, in contrast to related works in literature that are based on parametrized model Hamiltonians [72, 86, 112].

## 4.4 Conclusion

We develop a Hamiltonian MC framework in order to efficiently sample the spin space for electronic-structure based models of magnetic materials. From auxiliary spin-dynamics we derive a Hamiltonian MC algorithm for spin systems. Our tests with the classical Heisenberg model show that this algorithm has a fast warm-up efficiency and a reasonably small dynamical critical exponent. The utilization of the temperature-dependent spin-cluster expansion as an auxiliary model to run

auxiliary spin-dynamics further accelerates the exploration of the spin space. Our application employing the magnetic bond-order potentials demonstrates the efficiency of our sampler. We compute the magnetization curve, the magnetic contribution to the specific heat, and the Curie temperature of bcc iron as predicted by the BOP model with high fidelity. We conclude that this work paves the way towards atomistic simulations of magnetic materials with complex spin interactions, and look forward to seeing applications of our method for more complex models, such as non-collinear magnetic density-functional theory.

# Chapter 5

## Application to magnetic iron

In this chapter, we apply the methods developed in chapter 3 and 4 to study magnetic iron at finite temperature. More specifically, we aim at investigating

1. the magnetic phase transition in bcc and fcc iron,
2. the interplay between spin fluctuations and atomic vibrations,
3. the effect of longitudinal spin fluctuations (LSF) on the magnetic and  $\alpha$  (bcc) -  $\gamma$  (fcc) structural phase transitions,
4. the  $\alpha$  (bcc) -  $\gamma$  (fcc) -  $\delta$  (bcc) phase transitions.

We use the first and the second part as a benchmark test of our methods as there are both experimental and first-principles results for magnon-phonon coupling in iron. The third part is a good example to show the strength of our methods as LSF and its coupling to the lattice are treated properly in our model and the collective nature of spin fluctuations requires an efficient Monte Carlo sampler. In the last part, we offer our insight into the  $\alpha$  (bcc) -  $\gamma$  (fcc) -  $\delta$  (bcc) phase transitions in iron, which have been studied by numerous investigators with different methods over decades and still has controversy about its microscopic origin.

All the results shown in this chapter are based on the tight binding parametrizations of Mrovec *et al.* [95], and the parameter  $\bar{U} = U - 1/2J$  is chosen as 3.6 eV and  $J$  chosen as 0.8 eV, as suggested by Belozarov and Anisimov [15] based on their LDA+DMFT calculations. We focus on the vibrational and magnetic excitations and neglect the free-electron excitations in all the calculations. We use the BOPfox program [50] to solve the single-electron effective Hamiltonian, and the method of Methfessel and Paxton [92] is used to sample the Brillouin-zone.

## 5.1 Magnetic phase transition in bcc and fcc iron

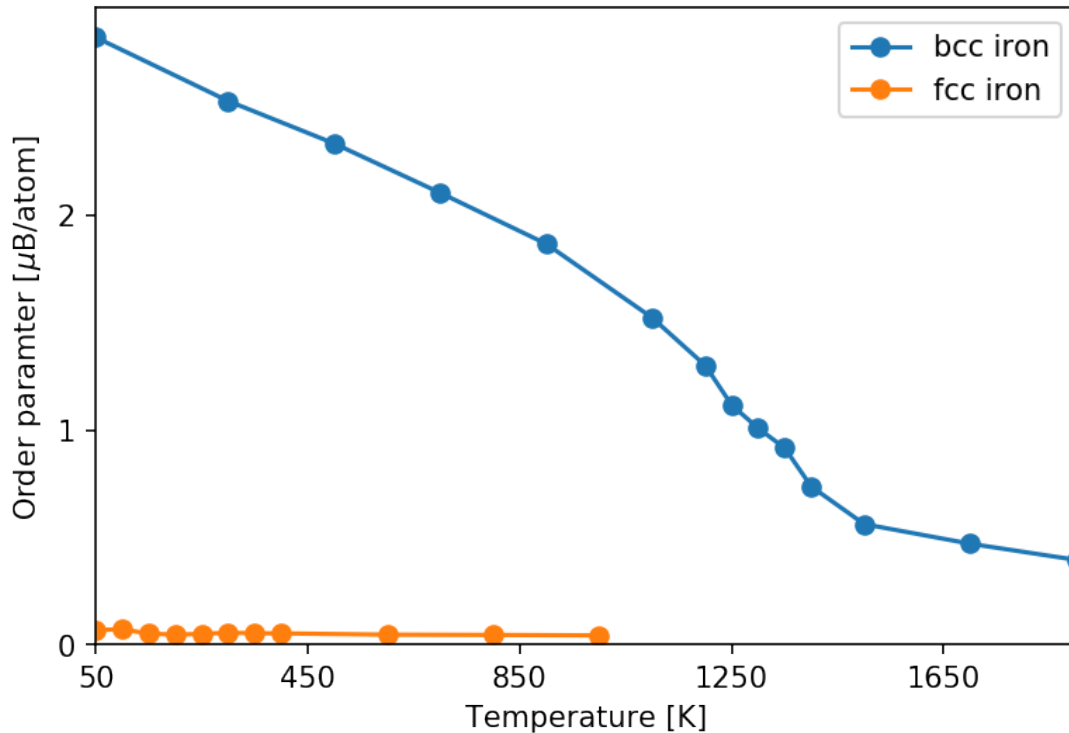


Figure 5.1: Order parameter of bcc and fcc iron plotted as function of temperature. The bcc supercell contains 250 atoms, and the fcc supercell contains 300 atoms.

We first calculate the magnetic phase transition in bcc and fcc iron. We choose different order parameters for bcc and fcc iron as they have different magnetic ground states. As bcc iron has a ferromagnetic ground state and transforms to paramagnetic state at high temperature, the total magnetization is a natural choice of its order parameter. The magnetic ground state of fcc iron is the antiferromagnetic double layer with two sublattices having opposite magnetization, and we choose the difference of the magnetizations of the two sublattices as its order parameter. We plot in Fig. 5.1 the calculated order parameters as function of temperature. The lowest temperature we considered is 50 K as our model is based on the static approximation, which becomes problematic at very low temperature due to the presence of strong quantum fluctuations. The order parameter of fcc iron is close to zero at temperature higher than 50 K, which indicates that the calculated



magnetic phase-transition temperature (Néel-Temperature) is lower than 50 K. In contrast, the magnetic ordering of bcc iron remains at much higher temperature, and the calculated magnetic phase-transition temperature (Curie temperature) of bcc iron is around 1250 K, close to the experimental value.

## 5.2 Interplay between spin fluctuations and atomic vibrations

At evaluated temperatures, both spin and lattice degrees of freedom (DOFs) are excited in magnetic materials. The coupling of the two types of excitations, denoted as magnon-phonon coupling in this chapter, plays an important role in thermodynamics and kinetics [107, 115, 120, 126, 134]. We next use our model to study the interplay of the atomic vibrations and spin fluctuations in magnetic iron and first put the focus of this subsection on the effect of the spin fluctuations on phonon spectra. The calculations are based on the spin-space averaging scheme [70]. Here we perform an extension of this scheme in order to include the effect of both transverse and longitudinal spin fluctuations. If we assume that the magnetic excitations have faster time scales, we can then define the mean atomic force as

$$\bar{\mathbf{F}}_k(\{\mathbf{r}_i\}) = \frac{1}{Z^{\text{mag}}(\{\mathbf{r}_i\})} \int \prod_i d\mathbf{h}_i \mathbf{F}_k(\{\mathbf{r}_i, \mathbf{h}_i\}) \times \exp[-\beta E_{\text{pot}}(\{\mathbf{r}_i, \mathbf{h}_i\})]. \quad (5.1)$$

where the mean atomic force is defined as a thermal average with respect to spin fluctuations, and  $Z^{\text{mag}}(\{\mathbf{r}_i\})$  is the magnetic partition function for a given atomic configuration  $\{\mathbf{r}_i\}$ ,

$$Z^{\text{mag}}(\{\mathbf{r}_i\}) = \int \prod_i d\mathbf{h}_i \exp[-\beta E_{\text{pot}}(\{\mathbf{r}_i, \mathbf{h}_i\})]. \quad (5.2)$$

Based on the mean force defined in Eq. 5.1, we employ the small-displacement method to calculate phonon spectra at finite magnetic temperature. In its implementation, we compute the thermal average of the restoring force instead of the atomic force Eq. (5.1) [70]. If we shift the  $\gamma$ -component of the position of atom  $l$  by a small displacement  $\Delta r_l^\gamma$ , the corresponding restoring force can be evaluated

through

$$\begin{aligned} \bar{F}_k^\alpha(\{r_i^\zeta\}_{i\zeta\neq l\gamma}, r_l^\gamma + \Delta r_l^\gamma) - \bar{F}_k^\alpha(\{\mathbf{r}_i\}) = \\ \frac{1}{Z^{\text{mag}}} \int \prod d\mathbf{h}_i \left[ F_k^\alpha(\{r_i^\zeta\}_{i\zeta\neq l\gamma}, r_l^\gamma + \Delta r_l^\gamma, \{\mathbf{h}_i\}) - F_k^\alpha(\{\mathbf{r}_i, \mathbf{h}_i\}) \right] \exp[-\beta E_{\text{pot}}(\{\mathbf{r}_i, \mathbf{h}_i\})]. \end{aligned} \quad (5.3)$$

A cleaner expression can be immediately obtained by dividing both sides in Eq. (5.3) by the small displacement  $\Delta r_l^\gamma$  and employing the definition of the force constant  $\Phi_{i,j}^{\alpha,\gamma}$ ,

$$\bar{\Phi}_{i,j}^{\alpha,\gamma}(\{\mathbf{r}_i\}) = \frac{1}{Z^{\text{mag}}} \int \prod d\mathbf{h}_i \Phi_{i,j}^{\alpha,\gamma}(\{\mathbf{r}_i\}, \{\mathbf{h}_i\}) \exp[-\beta E_{\text{pot}}(\{\mathbf{r}_i\}, \{\mathbf{h}_i\})]. \quad (5.4)$$

In other words, we define a mean force constant  $\bar{\Phi}_{i,j}^{\alpha,\gamma}(\{\mathbf{r}_i\})$  at finite magnetic temperature, and use it to calculate finite-temperature phonon spectra in an effective manner. This method can be viewed as an effective harmonic approximation to treat phonon anharmonicity induced by spin fluctuations.

In practice, we choose a small displacement of 0.01 Å and use Eq. (5.4) to calculate the phonon spectra of bcc and fcc iron at finite magnetic temperature. The first pronounced effect we observed is that the spin fluctuations stabilize the phonon modes of fcc iron. This observation has already been reported by Körmann *et al.* [70] with their first-principles calculations. Here we reproduce this result with our model. In Fig. 5.2, we plot the phonon spectra of fcc iron in the ferromagnetic state and at the magnetic temperature of 1573 K, and the experimental data [100] are also plotted for comparison. There are imaginary phonon frequencies around the  $\Gamma$  point in ferromagnetic fcc iron. However, all frequencies become positive once spin fluctuations at 1573 K are taken into account, and this gives an excellent agreement with experimental data [100].

For bcc iron, the phonon spectra at 773 K, 1043 K, 1173 K, and 1743 K are shown in Fig. 5.3. We observe strong phonon softening in bcc iron with increasing magnetic temperature and the N point and the 2/3[111] point in the  $\Gamma - \text{H}$  branch are softened most significantly, which are related to the bcc-hcp and bcc-fcc phase transitions [64]. It means that bcc iron gains more and more vibrational entropy with increasing temperature and becomes more and more thermodynamically favorable, and we will show in Section 5.4 that this leads to the  $\gamma - \delta$  phase transition.

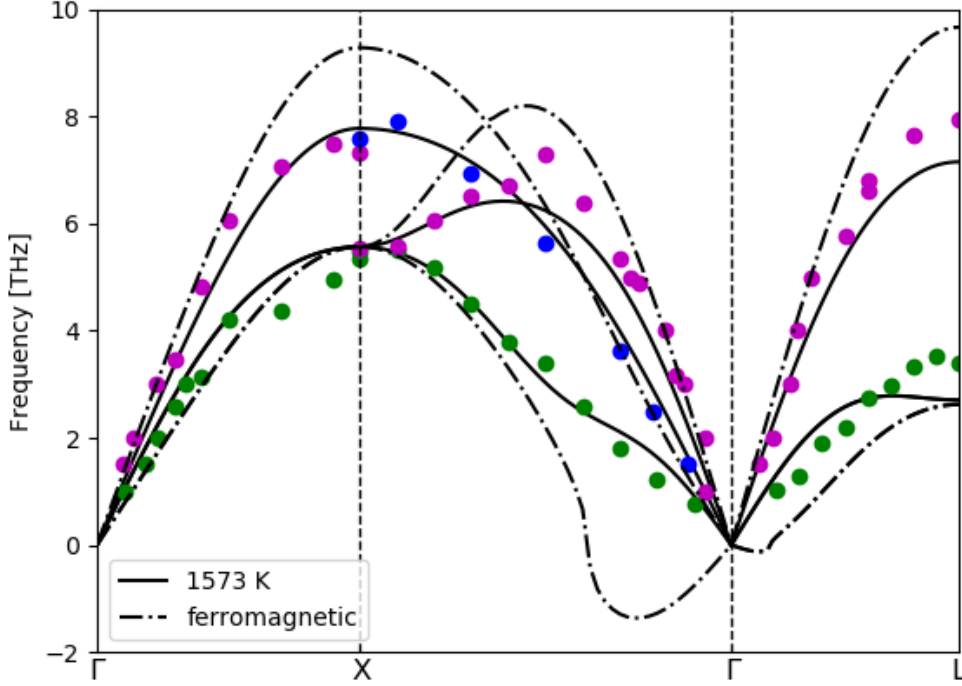


Figure 5.2: Calculated phonon spectra of fcc iron in the ferromagnetic state (dashed line) and at the magnetic temperature of 1573 K (full line). Dots: experimental phonons at 1573 K from Neuhaus et al. [100]

We next take the  $T_1$  phonon branch at the  $N$  point as an example to illustrate the reason for the phonon softening. We first plot the temperature-dependent force constants for the first and second shells of neighbours in Fig. 5.4, There are four independent components,  $\Phi_{xx}(a/2, a/2, a/2)$ ,  $\Phi_{xy}(a/2, a/2, a/2)$ ,  $\Phi_{xx}(a, 0, 0)$  and  $\Phi_{yy}(a, 0, 0)$ , according to the crystal symmetry of bcc lattice, and they are denoted in Fig. 5.4 as the small Greek letters  $\alpha_1$ ,  $\beta_1$ ,  $\alpha_2$ , and  $\beta_2$  following the convention in [136]. We plot in the last two subplots in Fig. 5.4 the stretching (longitudinal) and shearing (transverse) force constants  $\Phi_1^L$  and  $\Phi_1^T$  for the first-nearest neighbour, which are converted from  $\alpha_1$  and  $\beta_1$  through

$$\begin{aligned}\alpha_1 &= \frac{2}{3}\Phi_1^T + \frac{1}{3}\Phi_1^L \\ \beta_1 &= -\frac{1}{3}\Phi_1^T + \frac{1}{3}\Phi_1^L.\end{aligned}\tag{5.5}$$

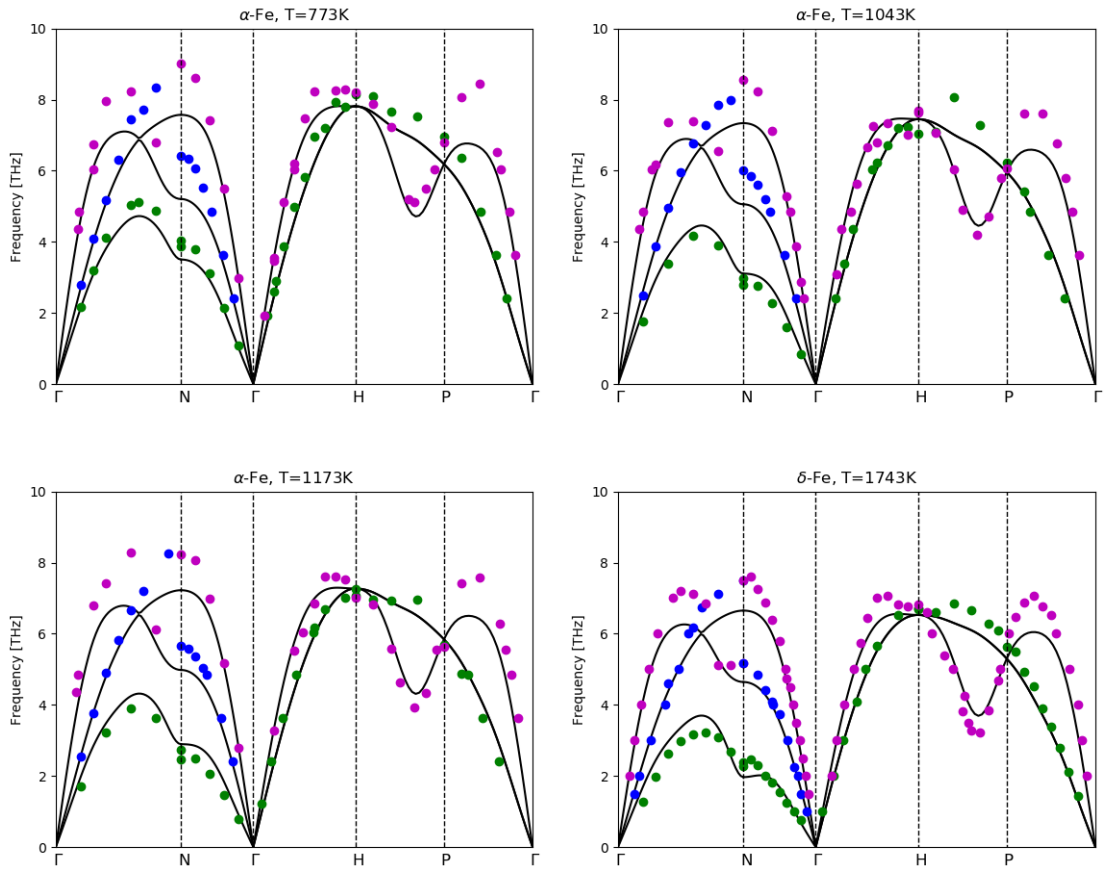


Figure 5.3: Calculated phonon spectra of bcc iron at magnetic temperatures of 773 K, 1043 K, 1173 K and 1743 K, respectively. Lines: calculated results in this work. Dots: experimental data from Neuhaus et al. [100].

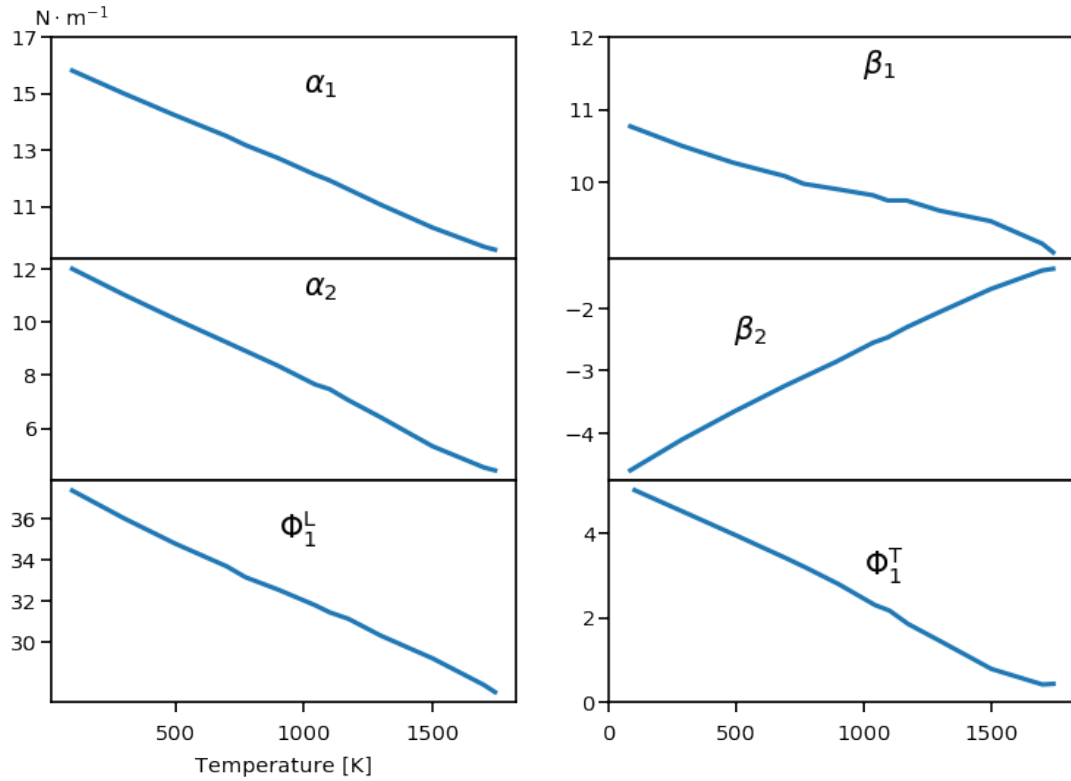


Figure 5.4: Calculated force constants for the first and second neighbours as function of magnetic temperature.

The expressions above are obtained from Eq. (2.56). If we only consider the first- and second-nearest-neighbour interactions, the  $T_1$  vibrational mode at the  $N$  point can be expanded linearly in terms of the force constants in the global coordinate frame, as given by Eq. (2.55). Substituting Eq. (5.5) into Eq. (2.55), we obtain

$$4\pi^2 M \nu_{T_1}^2 = 8\Phi_1^T + 4\alpha_2 + 4\beta_2. \quad (5.6)$$

We see in Eq. (5.6) that the  $T_1$  vibrational mode at the  $N$  point is determined by the shearing force constant of the first-nearest-neighbour,  $\Phi_1^T$ , the stretching force constant of the second-nearest-neighbour,  $\alpha_2$ , and the shearing force constant of the second-nearest-neighbour,  $\beta_2$ , and the drastic softening of this mode is caused the significant decrease of  $\Phi_1^T$  and  $\alpha_2$ , as shown in Fig. 5.4.

We next investigate the effect of atomic vibrations on spin fluctuations by measuring the magnetization as a function of temperature with and without the

influence of atomic vibrations. To calculate the magnetization curve without the influence of atomic vibrations (shown as orange dots in Fig. 5.5), we suppress atomic vibrations by fixing atoms in the perfect bcc lattice and measure the magnetization according to

$$\bar{M}(\{\mathbf{r}_i^{\text{bcc}}\}) = \frac{1}{Z_{\text{mag}}(\{\mathbf{r}_i^{\text{bcc}}\})} \int \prod_i d\mathbf{h}_i M(\{\mathbf{r}_i^{\text{bcc}}, \mathbf{h}_i\}) \times \exp[-\beta E_{\text{pot}}(\{\mathbf{r}_i^{\text{bcc}}, \mathbf{h}_i\})], \quad (5.7)$$

where  $\mathbf{r}_i^{\text{bcc}}$  is the atomic position of the perfect bcc lattice. To calculate the magnetization curve with the influence of atomic vibrations (shown as blue dots in Fig. 5.5), the atomic vibrations are allowed and the magnetization is measured according to

$$\bar{M} = \frac{1}{Z} \int \prod_i d\mathbf{h}_i d\mathbf{r}_i M(\{\mathbf{r}_i, \mathbf{h}_i\}) \exp[-\beta E_{\text{pot}}(\{\mathbf{r}_i, \mathbf{h}_i\})]. \quad (5.8)$$

As shown in Fig. 5.5, the atomic vibrations have a prominent effect on spin fluctuations. The thermal atomic vibrations accelerate the collapse of the long-range magnetic order and the Curie temperature is significantly reduced if atomic vibrations are included. We notice that there is the same conclusion in the recent paper of Ruban and Peil [112]. In contrast to their work which is based on the first-principles parametrized classical Heisenberg model, here we obtained a direct evidence for the strong influence of atomic vibrations on spin fluctuations.

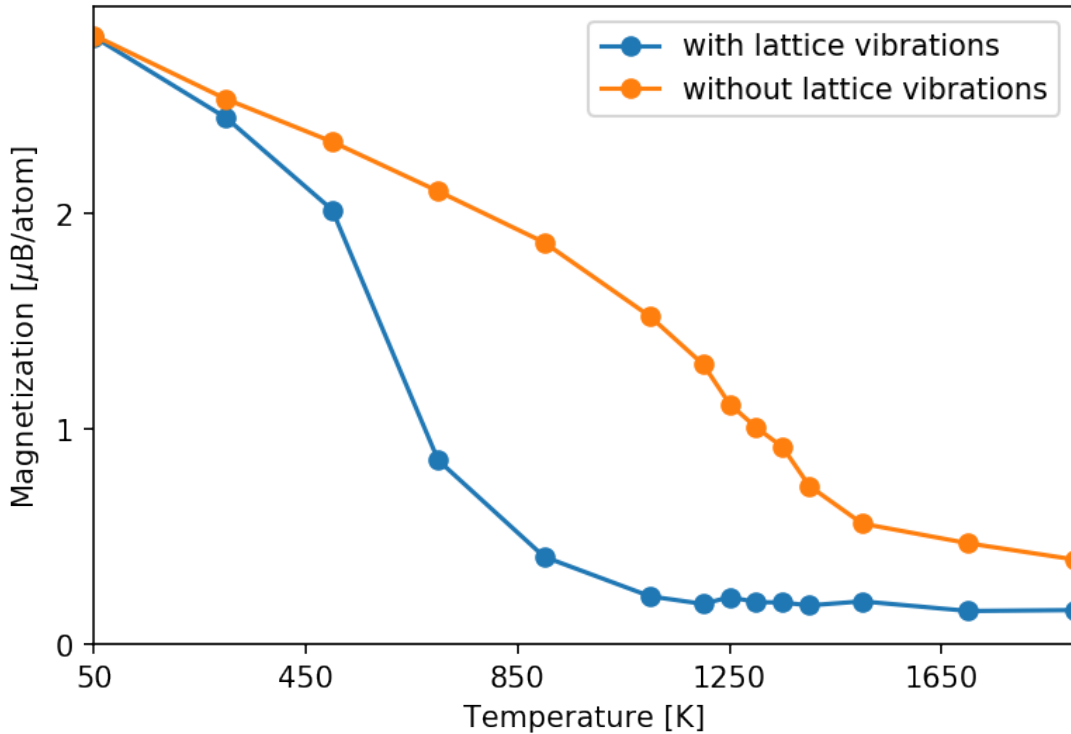


Figure 5.5: Calculated magnetization as function of temperatures. Orange dots: magnetization of a perfect  $5 \times 5 \times 5$  bcc supercell of iron with atomic positions fixed. Blue dots: atomic vibrations are included in the  $5 \times 5 \times 5$  bcc supercell of iron.

### 5.3 Effect of longitudinal spin fluctuations

In this section, we aim at investigating the effect of longitudinal spin fluctuations (LSF) on phase transitions in iron. The schematic phase diagram of iron is shown in Fig. 5.6 [81]. At the low-temperature and low-pressure regime, the  $\alpha$  phase is thermodynamically most stable and has a body-centered cubic structure. With increasing temperature, there is a magnetic phase transition from the ferromagnetic to the paramagnetic state at 1043 K and ambient pressure. This order-disorder phase transition is of second-order, which means that the second-order derivative of the free energy is discontinuous at the critical point. At around 1185 K and ambient pressure, there is a structural phase transition from the paramagnetic bcc iron to the paramagnetic fcc iron, where the latter is referred to as the  $\gamma$  phase. If we continue to increase temperature, there is another phase transition from para-

magnetic fcc iron to paramagnetic bcc iron that is referred to as  $\delta$  phase. We focus in this section on the effect of LSF on the magnetic phase transition and  $\alpha$ - $\gamma$  structural phase transition. The  $\alpha$  (bcc) -  $\gamma$  (fcc) -  $\delta$  (bcc) phase transitions will be discussed in the next section.

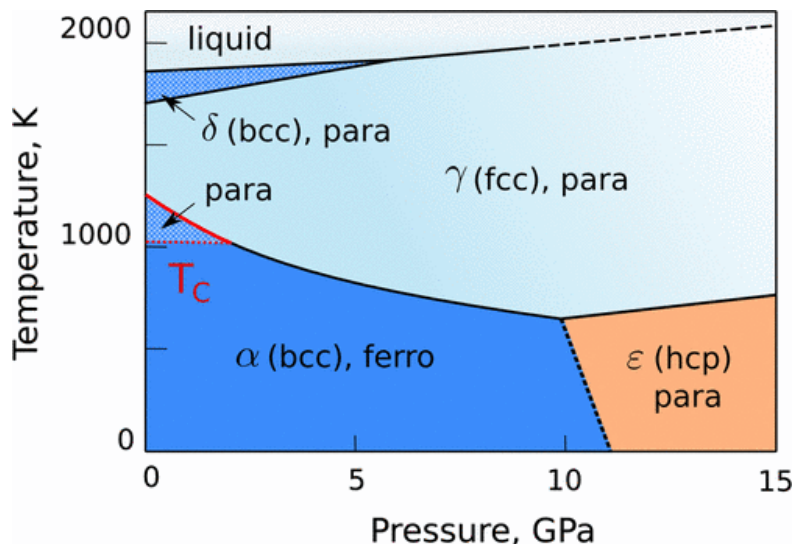


Figure 5.6: The schematic pressure-temperature phase diagram of pure iron taken from [81] and reused under the license number RNP/19/OCT/019548.

It is well known that the spin length of itinerant-electron magnets is not fixed, and its fluctuations, known as longitudinal spin fluctuations (LSF), contribute to entropy and influence the thermodynamics and kinetics at finite temperatures [28]. The simulation of LSF requires to go beyond the frequently-used Heisenberg model [74, 89, 127] as the electronic structure is involved. There were several attempts to include LSF in finite-temperature simulations of magnetic transition-metals. As a direct extension of the Heisenberg model, Ruban et al. [111] introduced a LSF model Hamiltonian which is parametrized with ab initio calculations and solved with a Monte Carlo algorithm. Similarly, Ma and Dudarev [86] proposed a Heisenberg-Landau model to describe the magnetic interactions for both transverse and longitudinal degrees of freedom and a generalized Langevin spin dynamics to perform dynamical simulations. The two models capture successfully the collective-excitations nature of both TSF and LSF with a numerically affordable methodology. However, they should be classified to be classical or empirical



models due to the missing of an explicit treatment of the electronic structure. Furthermore, the parametrizations with respect to different magnetic reference states may lead to different results. Another drawback is that they only include magnetic interactions and contain no spin-lattice couplings. This limits their application to simulations of structural phase transitions. The approach that combines density functional theory (DFT) and dynamical mean-field theory (DMFT), the so-called DFT+DMFT [75], treats the electronic-correlations and LSF in a dynamical mean-field manner. This model is usually solved with quantum Monte Carlo algorithms. It captures the itinerant-electron and the electron-correlation nature of LSF and is state-of-the-art one of the most consistent approaches to model finite-temperature magnetism of itinerant-electron magnets [5]. However, both TSF and LSF are collective excitations, while they are treated as single-site excitations in DMFT, which is the main drawback of this approach.

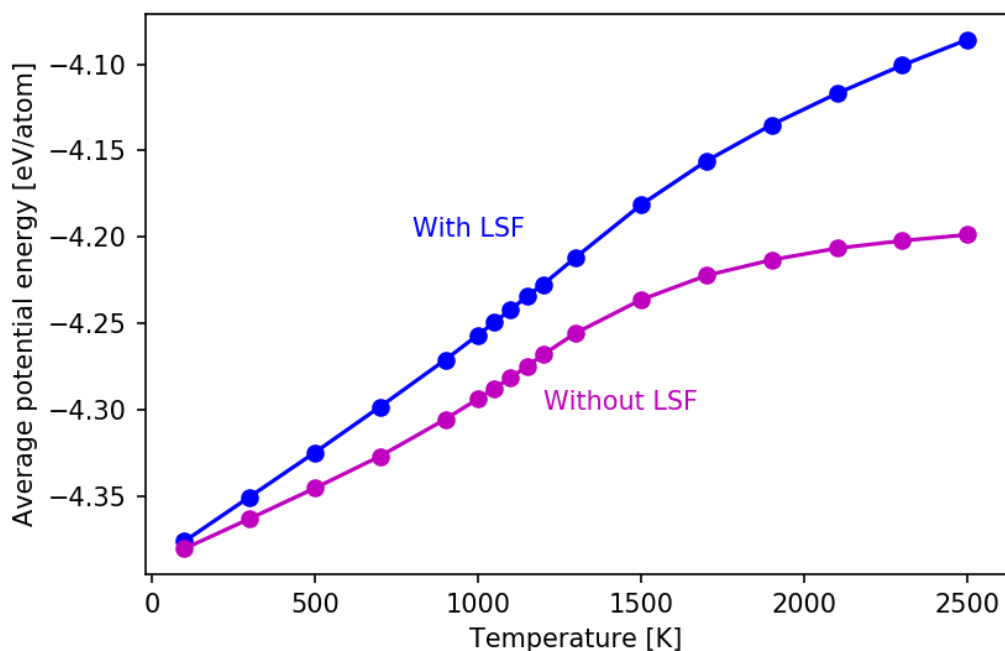


Figure 5.7: Average potential energy plotted as function of temperature.

In our calculations, we fix the atomic positions and use the magnetic partition function for TSF Eq. (3.19) and that for full spin fluctuations Eq. (3.11) to

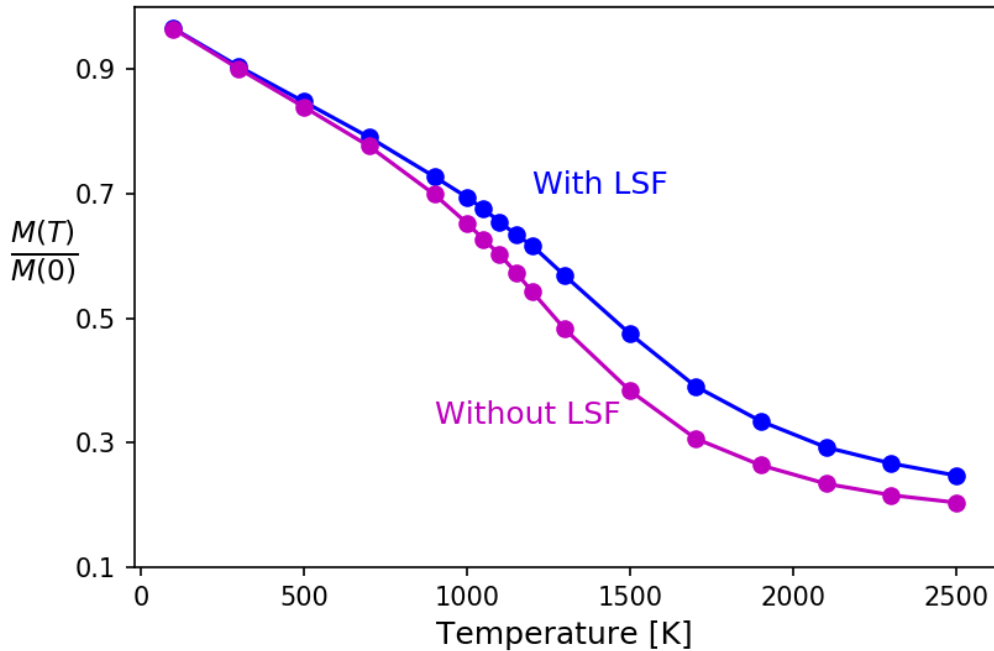


Figure 5.8: Magnetization plotted as function of temperature.

investigate the effect of LSF on the magnetic phase transition of bcc iron and the  $\alpha - \gamma$  structural phase transition. LSF in our model is described based on the electronic-structure model compared to the empirical models [86, 111] and is collective compared to single-site in DFT+DMFT [81, 83].

We compare in Fig. 5.7 the average potential energy as a function of temperature with and without LSF. For the case without LSF, only the transverse magnetic degrees of freedom are excited by thermal fluctuations. For the case with LSF, both the transverse and longitudinal magnetic DOFs are included in thermal excitations. As expected, the two curves reach the same value in the low-temperature limit as a result of the same ferromagnetic ground state. The slope of the potential energy, corresponding to magnetic contributions to heat capacity, is higher for the case with LSF as more degrees of freedom are excited.

The magnetization curves with and without LSF are shown in Fig. 5.8. The magnetization curve with LSF is above that without LSF over the whole temperature range. This can be explained by a histogram of magnitudes of atomic magnetic moments as shown in Fig. 5.9, in which we observe that the magni-

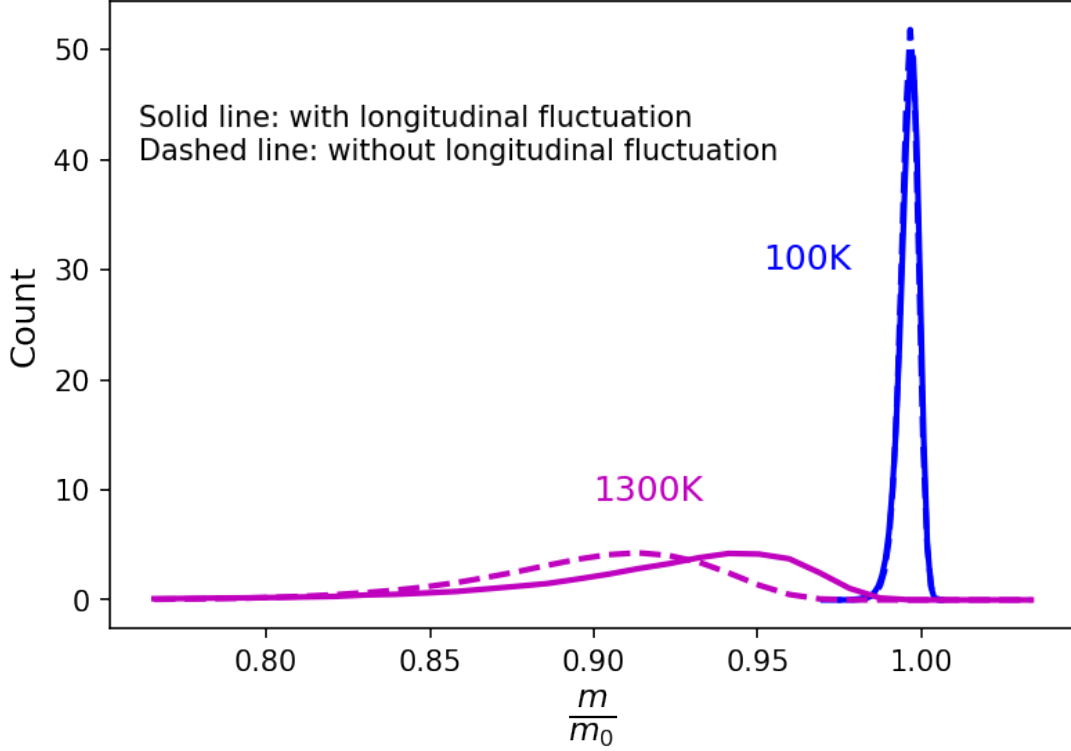


Figure 5.9: Histogram of magnitudes of atomic magnetic moments at 100 K and 1300 K.

tudes of atomic magnetic moments become higher when the longitudinal degrees of freedom are excited.

We next investigate the effect of LSF on thermodynamics and kinetics of the  $\alpha - \gamma$  structural phase transition in iron by calculating the magnetic free-energy profile along the Bain path. We employ the body-centered tetragonal (bct) unit cell, as shown in Fig. 5.10, and the  $c/a$  ratio of 1 ( $\sqrt{2}$ ) corresponds to the bcc (fcc) structure. We use a  $3 \times 3 \times 3$  bct supercell of iron containing 54 atoms. The order parameter for the bain transformation is the  $c/a$  ratio in the body-centered tetragonal unit cell shown in Fig. 5.10, and it varies from 1 at bcc to  $\sqrt{2}$  at fcc. We need the derivative of the free energy with respect to  $k = c/a$  in order to perform a thermodynamic integration along the Bain path,

$$\frac{\partial F}{\partial k} = \left\langle \frac{\partial U_{\text{pot}}}{\partial k} \right\rangle, \quad (5.9)$$

and this derivative can be expressed in terms of the stress tensor, as shown below.

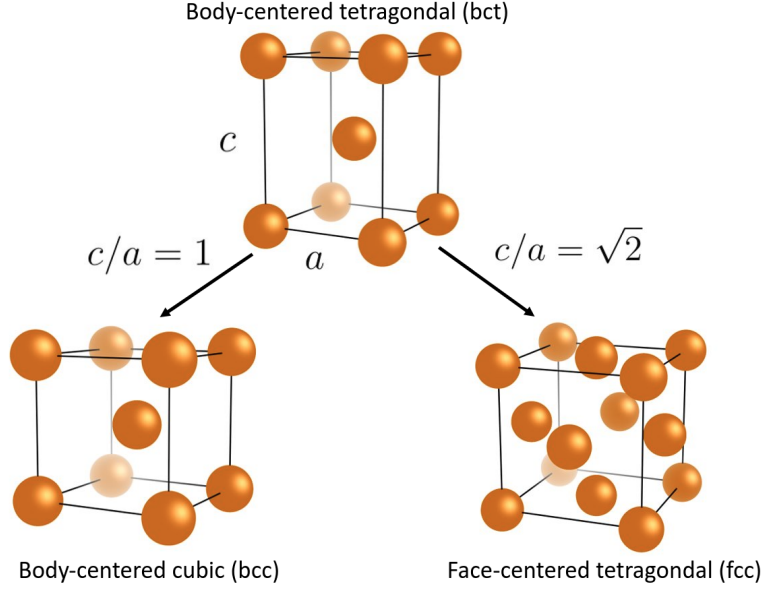


Figure 5.10: Unit cells of the body-centered tetragonal (bct), body-centered cubic (bcc) and face-centered cubic (fcc) lattices

The supercell at a given order parameter  $k$  is given as,

$$\mathbf{C} = \begin{vmatrix} V^{\frac{1}{3}}k^{-\frac{1}{3}} & 0 & 0 \\ 0 & V^{\frac{1}{3}}k^{-\frac{1}{3}} & 0 \\ 0 & 0 & V^{\frac{1}{3}}k^{\frac{2}{3}} \end{vmatrix}.$$

where  $V$  is the volume, which is fixed in the bain transformation.

The infinitesimal deformation of the supercell can be expressed in terms of the strain tensor,

$$\delta\mathbf{C} = \boldsymbol{\varepsilon} \mathbf{C}. \quad (5.10)$$

In the bain transformation, the infinitesimal deformation of the supercell can be expressed in terms of the order parameter  $k$ ,

$$\delta\mathbf{C} = \begin{vmatrix} -\frac{1}{3}V^{\frac{1}{3}}k^{-\frac{4}{3}}\delta k & 0 & 0 \\ 0 & -\frac{1}{3}V^{\frac{1}{3}}k^{-\frac{4}{3}}\delta k & 0 \\ 0 & 0 & \frac{2}{3}V^{\frac{1}{3}}k^{-\frac{1}{3}}\delta k \end{vmatrix}.$$

Substituting the expressions for  $\mathbf{C}$  and  $\delta\mathbf{C}$  into Eq. (5.10), we then obtain,

$$\frac{\boldsymbol{\varepsilon}}{\delta k} = \begin{vmatrix} -\frac{1}{3}k^{-1} & 0 & 0 \\ 0 & -\frac{1}{3}k^{-1} & 0 \\ 0 & 0 & \frac{2}{3}k^{-1} \end{vmatrix}.$$

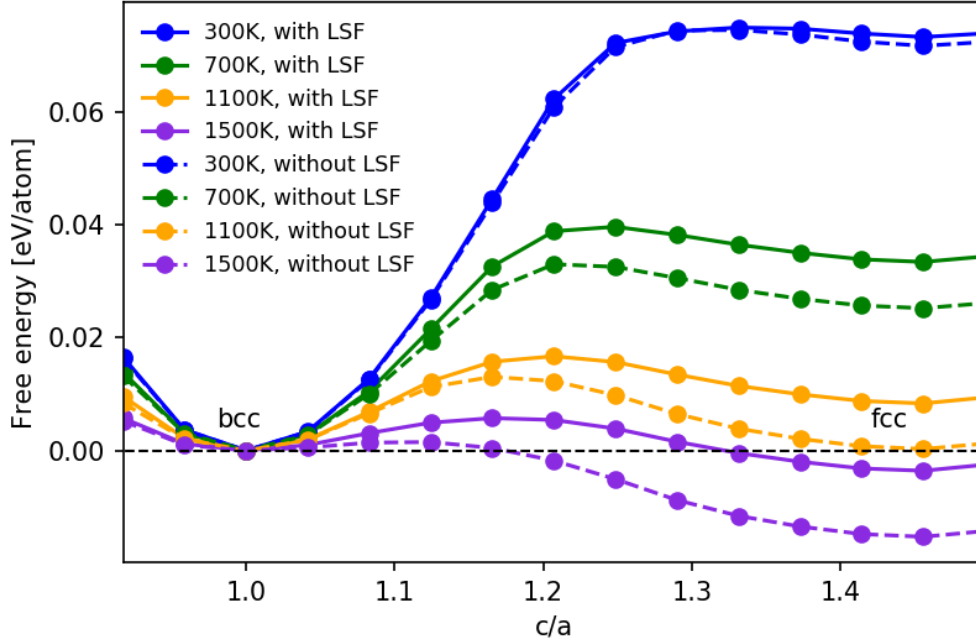


Figure 5.11: Magnetic free-energy profiles along bain transformation at different temperature.

The derivative of the potential energy with respect to the order parameter is then expressed in terms of the stress tensor,

$$\begin{aligned} \frac{\partial U_{\text{pot}}}{\partial k} &= \sum_{\alpha,\beta} \frac{\partial U_{\text{pot}}}{\varepsilon_{\alpha\beta}} \frac{\varepsilon_{\alpha\beta}}{\partial k} \\ &= -\frac{1}{3k} V (\sigma_{11} + \sigma_{22} - 2\sigma_{33}) \end{aligned} \quad (5.11)$$

In the last expression, we employed the relation,

$$\frac{\partial U_{\text{pot}}}{\partial \varepsilon_{\alpha\beta}} = V \sigma_{\alpha\beta}. \quad (5.12)$$

With Eq. (5.9) and (5.11), we are ready to calculate the magnetic free-energy profile along the Bain path with and without LSF, and our key result is shown in Fig. 5.11. At low temperature, the bcc structure is located at a deep local minimum while the fcc structure is located at a shallow local minimum. With increasing temperature, the magnetic free-energy barrier from bcc to fcc decreases

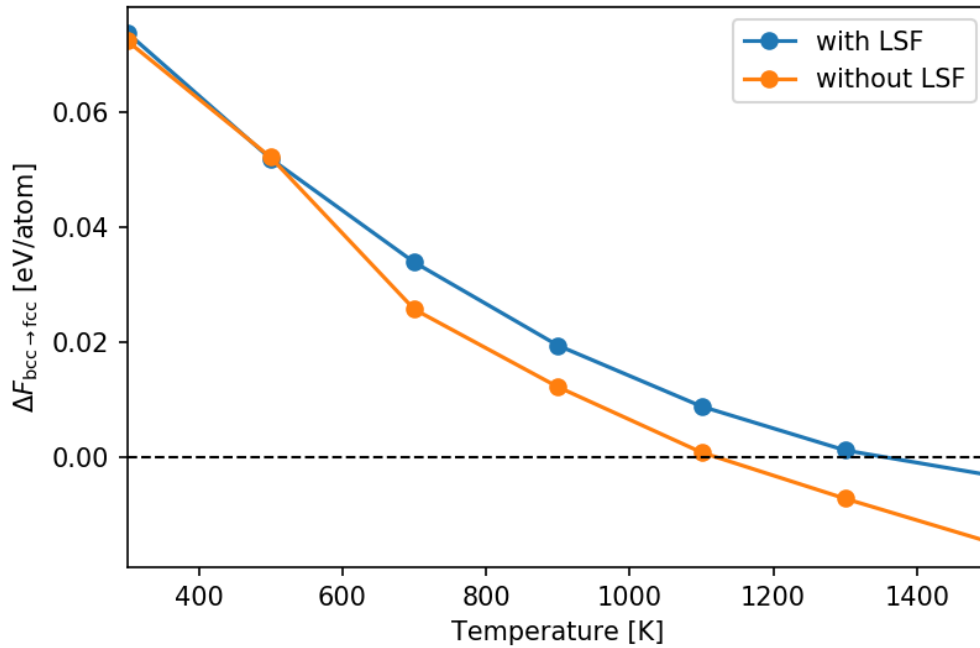
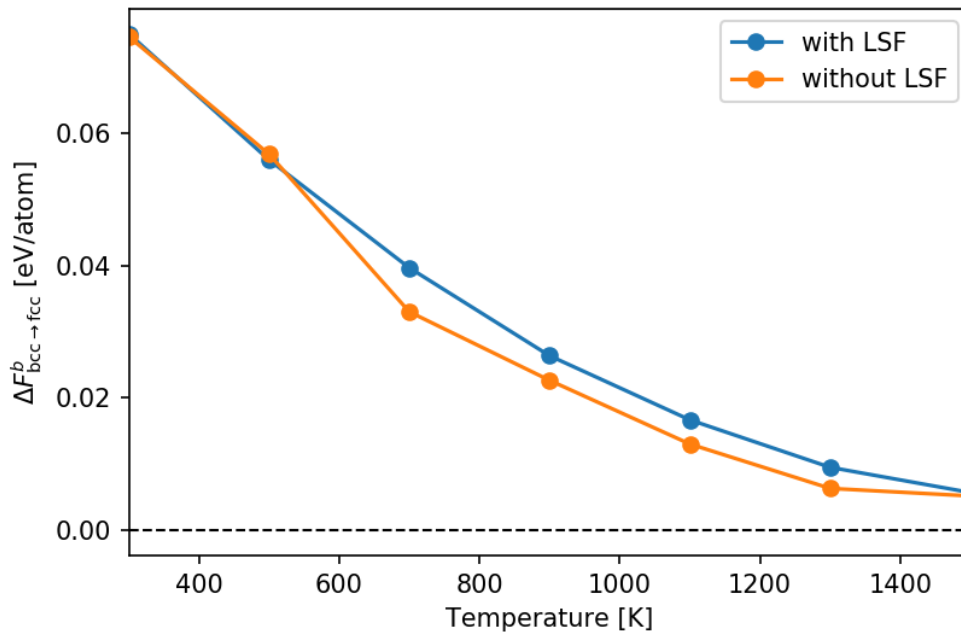
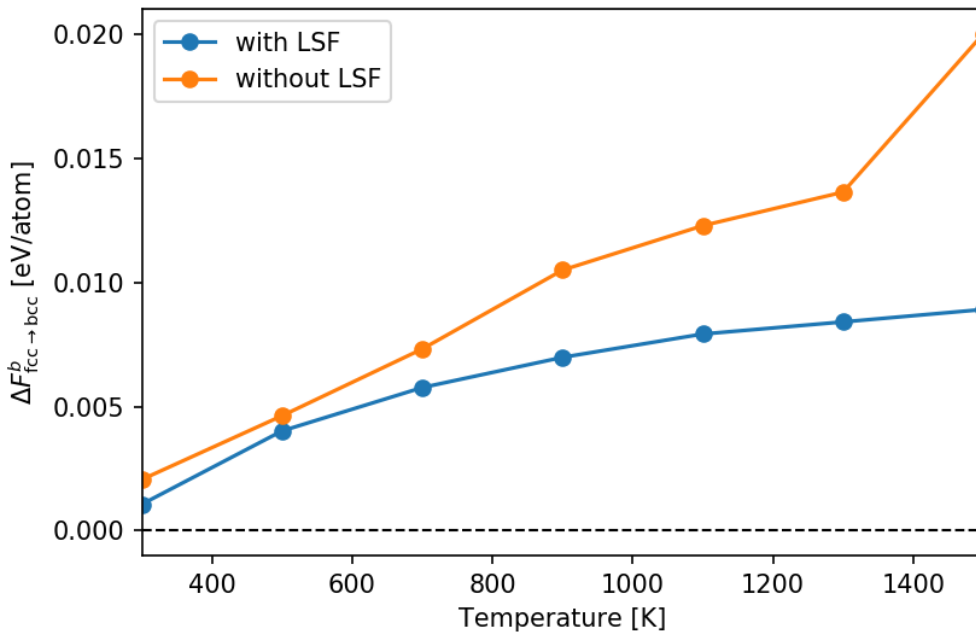


Figure 5.12: The magnetic free-energy difference of bcc and fcc iron as a function of temperature.

while that from fcc to bcc increases, and this makes the fcc structure more and more stable with increasing temperature. Regarding the effect of LSF, the magnetic free-energy difference between bcc and fcc iron is increased by LSF, and as a consequence, the phase-transition temperature is increased by around 200 K, as shown in Fig. 5.12. In Fig. 5.13a, we plot the magnetic free-energy barrier from fcc to bcc iron, which is the magnetic free-energy difference between the saddle point and the bcc lattice. The magnetic free-energy barrier from bcc to fcc iron is plotted in Fig. 5.13b. LSF increases the barrier from bcc to fcc iron while it decreases the barrier from fcc to bcc iron. We thus draw a conclusion that LSF favors bcc iron compared to fcc iron both thermodynamically and kinetically.



(a) From bcc to fcc iron.



(b) From fcc to bcc iron.

Figure 5.13: Magnetic free-energy barrier as a function of temperature.

## 5.4 $\alpha$ (bcc) - $\gamma$ (fcc) - $\delta$ (bcc) phase transitions

The  $\alpha$  (bcc) -  $\gamma$  (fcc) -  $\delta$  (bcc) phase transitions make iron quite unique among all elements in the periodic table and attract many theoretical calculations [53, 74, 81, 83, 88, 97]. The physics behind the  $\alpha$  (bcc) -  $\gamma$  (fcc) phase transition is more or less clear, and all theories attribute its driving force to be the magnetic (electronic) free-energy difference, namely, fcc iron has lower magnetic free energy than bcc iron at the  $\alpha$ - $\gamma$  phase-transition temperature. The main controversy lies in the microscopic origin of the  $\gamma$  (fcc) -  $\delta$  (bcc) phase transition, and there are basically two different arguments. The first argument states that the main driving force is the vibrational free-energy difference [83, 88, 97]. This argument is justified by the following considerations:

- Geometrically,  $\gamma$  iron has a close-packed fcc structure whereas  $\delta$  iron has an open bcc structure. As the atoms in bcc lattice have more space to vibrate than those in fcc lattice, bcc iron has more vibrational entropy and lower vibrational free energy than fcc iron.

In contrast, the second argument states that the driving force of this phase transition is not vibrational but magnetic (electronic) free-energy difference and that fcc iron has a higher magnetic free energy than bcc iron at the  $\gamma$ - $\delta$  phase-transition temperature [53, 68]. This argument is justified by the following considerations:

- In first-principles calculations, bcc iron has higher phonon free energy than fcc iron, which means that the vibrational free-energy difference does not support  $\gamma$ - $\delta$  phase transition and the first argument is not valid [68].
- bcc iron has more magnetic entropy and lower magnetic free energy than fcc iron at high temperature [53, 68] as the former has higher magnetic moment in Heisenberg models derived from DFT [68].

The first argument is based on a pure geometrical consideration and has already been shown to be valid for a large group of non-magnetic materials [117]. In order to check its validity for iron, special consideration should be devoted to magnon-phonon coupling which is shown to strongly impact vibrational properties of iron in both theories [51, 73, 83] and experiment [90]. Körmann [68] argued that the vibrational free-energy difference does not support the  $\gamma$ - $\delta$  phase transition based on the phonon calculations with the harmonic approximation, which



did not take into account magnon-coupling and might be problematic for iron. For the calculations of the magnetic (electronic) free-energy difference, the results of Hasegawa *et al.* [53] and Körmann [68] show that it supports the  $\alpha$ - $\gamma$  phase transition at low temperature and the  $\gamma$ - $\delta$  phase transition at high temperature. We note that both works contain strong approximations. Hasegawa *et al.* [53] employed a single-band tight binding model which may not describe the electronic structure properly, and Körmann [68] based his calculations on a Heisenberg Hamiltonian that neglects temperature dependence of the magnetic moment [7, 110, 111] and may oversimplify the complexity of exchange interactions in iron [79]. Indeed, in a more accurate calculation with DFT+DMFT [81], only the  $\alpha$ - $\gamma$  phase transition is reproduced whereas the  $\gamma$ - $\delta$  phase transition cannot be driven by the electronic (magnetic) excitations alone.

In our work, we first calculate the electronic (magnetic) contribution by performing a thermodynamic integration for the magnetic degrees of freedom from bcc to fcc iron. After that we calculate the vibrational contribution and treat the effect of spin fluctuations on atomic vibrations with the spin-space averaging scheme [70] as this method has been proven valid for calculations of magnon-phonon coupling in iron [73]. We finally obtain the total free-energy difference by summing up the two contributions, and will show that the combined effect of the two contributions leads to  $\alpha$  (bcc) -  $\gamma$  (fcc) -  $\delta$  (bcc) in iron.

Our calculation of the electronic contribution can be viewed as an extension of the work of Hasegawa and Pettifor [54]. Their calculation was based on a single d-band tight binding model and the assumption of the random spin environment that was treated by the coherent potential approximation. In our work, we use a full d-band tight binding model in order to better describe the electronic structure of iron and take into account the effect of short-range magnetic order by sampling explicitly the spin space. More specifically, we perform a thermodynamic integration from bcc to fcc iron, in which we fix the atomic positions and only consider spin fluctuations. The electronic free-energy difference  $\Delta F_{\text{bcc} \rightarrow \text{fcc}}^{\text{elec}}$  is evaluated accordingly,

$$\Delta F_{\text{bcc} \rightarrow \text{fcc}}^{\text{elec}}(T) = \int_0^1 d\lambda \langle U_{\text{pot}}(\{\mathbf{r}_i^{\text{fcc}}\}) - U_{\text{pot}}(\{\mathbf{r}_i^{\text{bcc}}\}) \rangle_\lambda, \quad (5.13)$$

where  $\lambda$  is the switching parameter going from zero to one, and the integrand is defined as a ensemble average with respect to the magnetic partition function

$$Z_\lambda = \int \prod_i d\mathbf{h}_i \exp \left\{ -\beta \left[ (1 - \lambda) U_{\text{pot}}(\{\mathbf{r}_i^{\text{bcc}}, \mathbf{h}_i\}) + \lambda U_{\text{pot}}(\{\mathbf{r}_i^{\text{bcc}}, \mathbf{h}_i\}) \right] \right\}. \quad (5.14)$$

The temperature  $T$  is the magnetic temperature indicating magnetic excitations. At 0 K, the electronic free-energy difference  $\Delta F_{\text{bcc} \rightarrow \text{fcc}}^{\text{elec}}$  corresponds to the ground-state energy difference between bcc and fcc iron, and at finite temperature, it contains the effect of magnetic excitations including both transverse and longitudinal spin fluctuations.

We plot in Fig. 5.14 the electronic free-energy difference as function of temperature. The spin fluctuations favor fcc iron compared to bcc iron and are sufficient to drive the  $\alpha - \gamma$  phase transformation even if we neglect the vibrational contribution. This observation is in agreement with the conclusion in [54], and both their and our works indicate that the spin fluctuations play a crucial role in the  $\alpha - \gamma$  phase transition in iron. We obtain in Fig. 5.14 a  $\alpha - \gamma$  transition temperature of around 1400 K, which is overestimated compared to the experimental value of around 1185 K. One reason for the overestimation here is due to the missing of the vibrational contribution which tends to stabilize fcc iron compared to bcc iron at low temperature, as will be shown later.

Another interesting point we can see in Fig. 5.14 is that the electronic contribution has a energy scale of several ten milli-electron volts and plays a dominant role in the low-temperature range and becomes less important in the high-temperature range. In the temperature range from 1400 K to 1700 K where the  $\gamma$  (fcc) -  $\delta$  (bcc) phase transition happens, the electronic free-energy difference is less than 6 meV/atom. We can understand the decrease of the influence of the electronic contribution with increasing temperature by looking at the electronic density of states at finite magnetic temperature. We plot in Fig. 5.15 the histograms of the electronic density of states (DOS) at magnetic temperature of 100 K, 700 K, and 1500 K. The spin fluctuations smear out the electronic DOS of bcc iron and make its electronic DOS closer to that of fcc iron with increasing temperature. This observation is in line with the deduction based on experiments that the electronic contribution is small in the  $\gamma$  (fcc) -  $\delta$  (bcc) phase transition [100].

We next calculate the vibrational contribution to  $\alpha$  (bcc) -  $\gamma$  (fcc) -  $\delta$  (bcc) phase transitions. We first employ the spin-space averaging scheme [70] to calculate

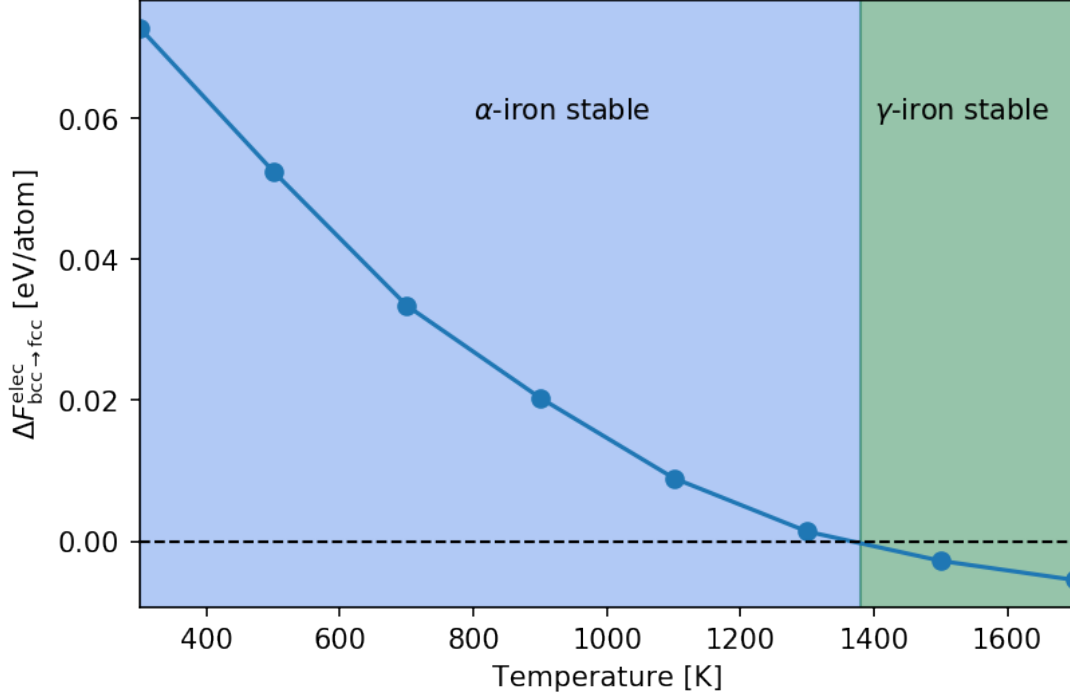


Figure 5.14: Calculated electronic free-energy difference between  $\alpha$  (bcc) and  $\gamma$  (fcc) iron.

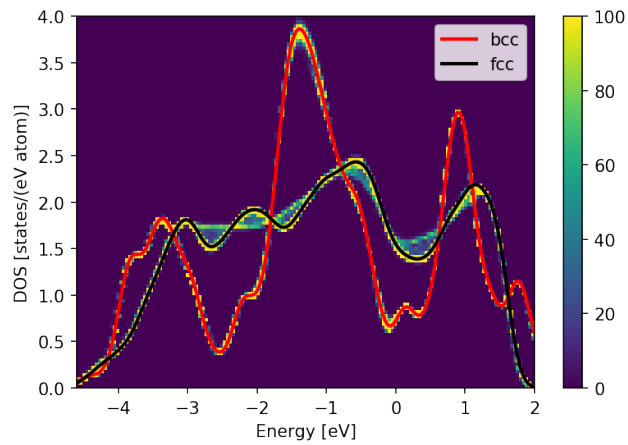
the phonon normal modes at finite magnetic temperature, and the thermal expansion is taken into account via experimental values [13]. The finite-temperature phonon density of states  $g(\varepsilon, T)$  are then approximated as the histogram of the SSA phonon normal modes. The vibrational entropy difference between bcc and fcc iron is calculated according to

$$\Delta S_{\text{bcc} \rightarrow \text{fcc}}^{\text{vib}}(T) = \int_0^{\infty} [g_{\text{fcc}}(\varepsilon, T) - g_{\text{bcc}}(\varepsilon, T)] S_i(\varepsilon, T) d\varepsilon, \quad (5.15)$$

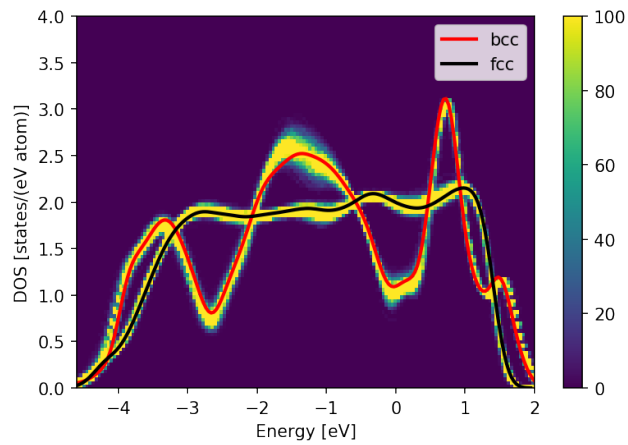
and the vibrational free-energy difference between bcc and fcc iron is calculated according to

$$\Delta F_{\text{bcc} \rightarrow \text{fcc}}^{\text{vib}}(T) = \int_0^{\infty} [g_{\text{fcc}}(\varepsilon, T) - g_{\text{bcc}}(\varepsilon, T)] F_i(\varepsilon, T) d\varepsilon, \quad (5.16)$$

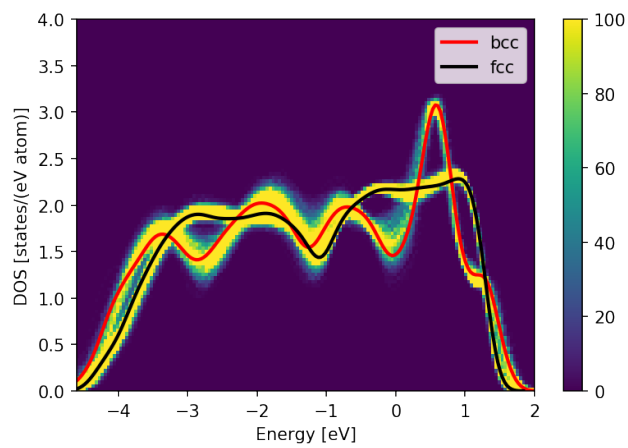
where  $g_{\text{bcc}}(\varepsilon, T)$  and  $g_{\text{fcc}}(\varepsilon, T)$  are the phonon density of states of bcc and fcc iron at magnetic temperature  $T$  within the SSA approximation, and  $S_i(\varepsilon, T)$  and  $F_i(\varepsilon, T)$  are the vibrational entropy and the vibrational free energy of the single harmonic



(a) 100 K



(b) 700 K



(c) 1500 K

Figure 5.15: The two-dimensional histograms of electronic density of states of bcc and fcc iron at different magnetic temperatures. 1000 magnetic configurations are employed at each temperature.

oscillator of frequency  $\omega = \varepsilon/\hbar$  at temperature  $T$  and given as Eq. (2.60) and Eq. (2.59).

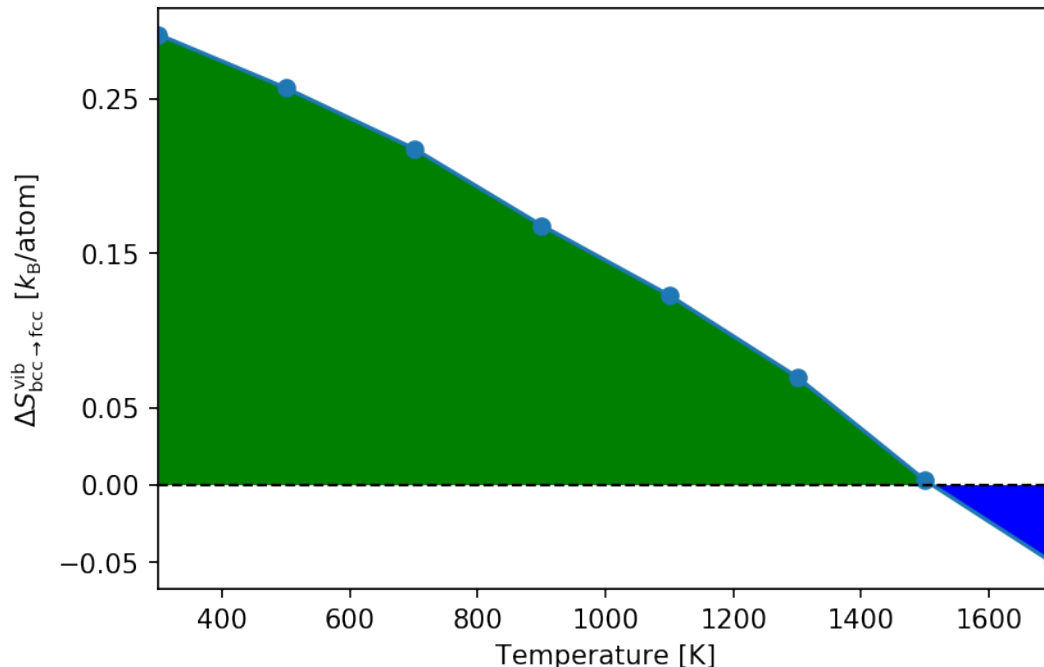


Figure 5.16: Calculated vibrational-entropy difference between fcc and bcc phases of iron as function of temperature.

In Fig. 5.16, we plot the vibrational-entropy difference between the bcc and fcc phases of iron. We see that there is a sign change at around 1500 K. It means that at temperature below 1500 K, the vibrational entropy tends to stabilize fcc while at higher temperature, it tends to stabilize bcc. This result is in an excellent qualitative agreement with the estimation based on experiments, which gives a sign-change temperature of around 1400 K [100].

We plot the vibrational free-energy difference as function of temperature in Fig. 5.17. With increasing temperature, the vibrational free-energy difference first decreases in the low-temperature range, and starts to increase at around 700 K. At first glance, it looks that this is not in agreement with the vibrational-entropy difference in Fig. 5.16 as the negative of the first derivative of free energy with respect to temperature is entropy,  $S = -\partial F/\partial T$ . However, this relation does not hold between  $\Delta S_{bcc \rightarrow fcc}^{vib}(T)$  given as Eq. (5.15) and  $\Delta F_{bcc \rightarrow fcc}^{vib}(T)$  given as Eq.

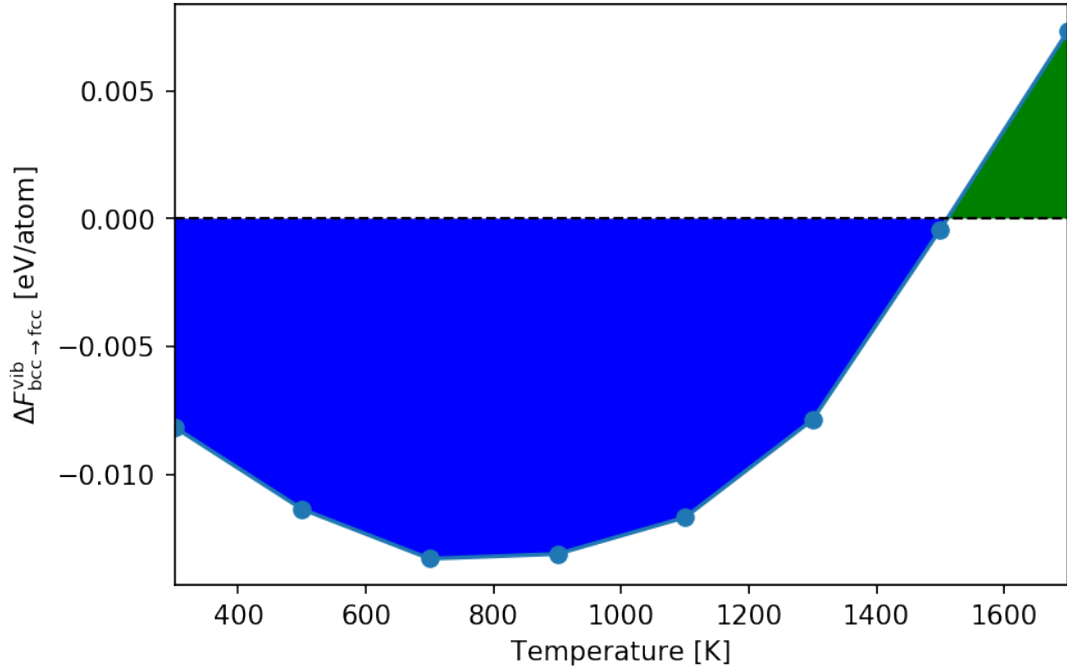
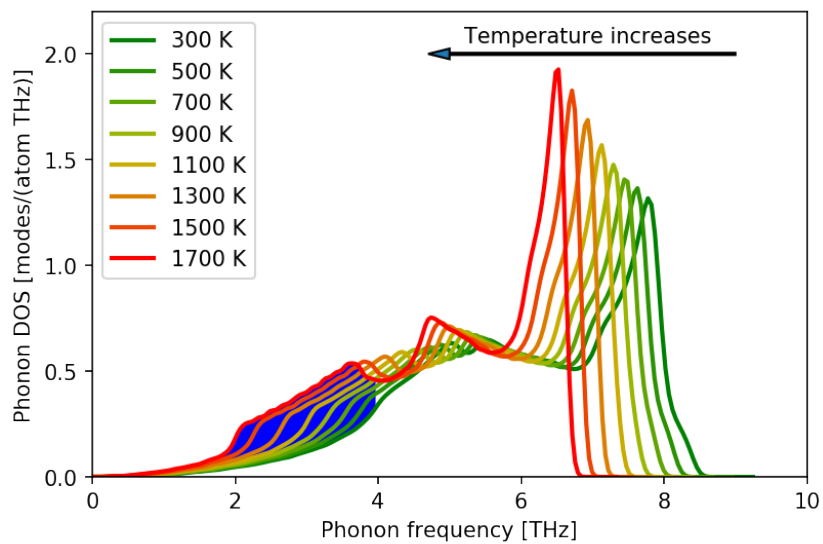


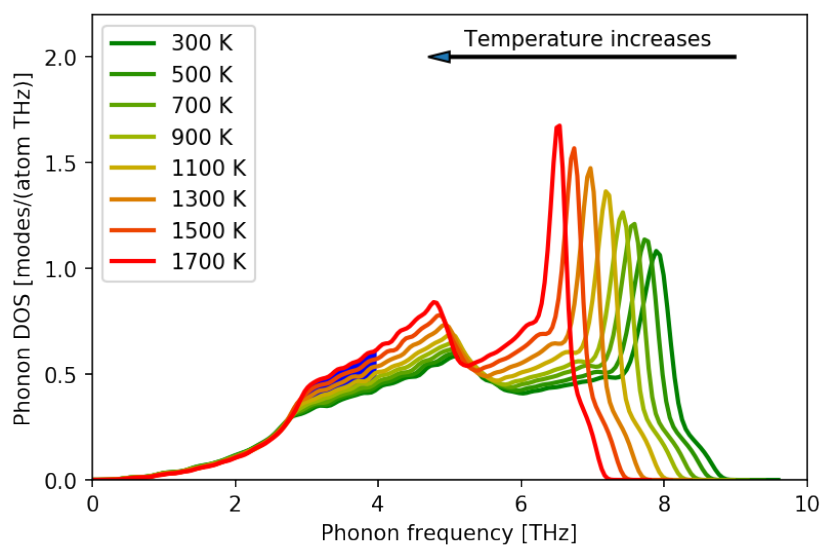
Figure 5.17: Calculated vibrational free-energy difference between fcc and bcc phases of iron as function of temperature.

(5.16) simply because we use the SSA approximation to calculate temperature-dependent phonon modes and a different phonon partition function is involved at different temperatures. We now return to the discussion of the magnetic free-energy difference. It changes from a negative value to a positive value with increasing temperature, and this means that the vibrational contribution tends to stabilize fcc iron at temperature below 1500 K and tends to stabilize bcc iron at temperature above 1500 K.

The interesting change of the vibrational free-energy difference is a consequence of the magnetic effect on atomic vibrations and can be understood by investigating the phonon density of states (DOS) at finite magnetic temperature. We plot in Fig. 5.18 the phonon DOS of bcc and fcc iron at different magnetic temperature. As indicated by the shaded region in Fig. 5.18, there is stronger softening of the low-frequency phonon modes in bcc iron than those in fcc iron. As a consequence of this and as shown in Fig. 5.19, fcc iron has more low-frequency phonon modes than bcc iron at low temperature, while bcc iron has more low-frequency phonon modes at high temperature. It is the reason for the change of the vibrational

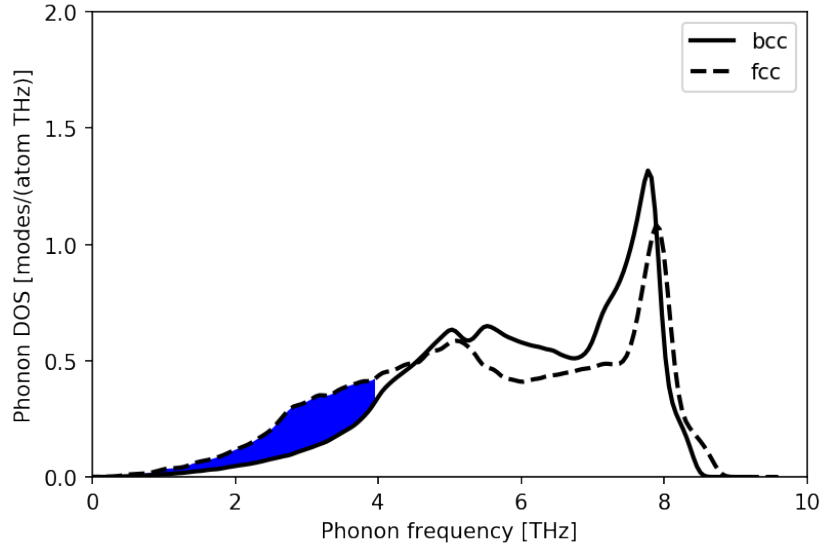


(a) bcc iron

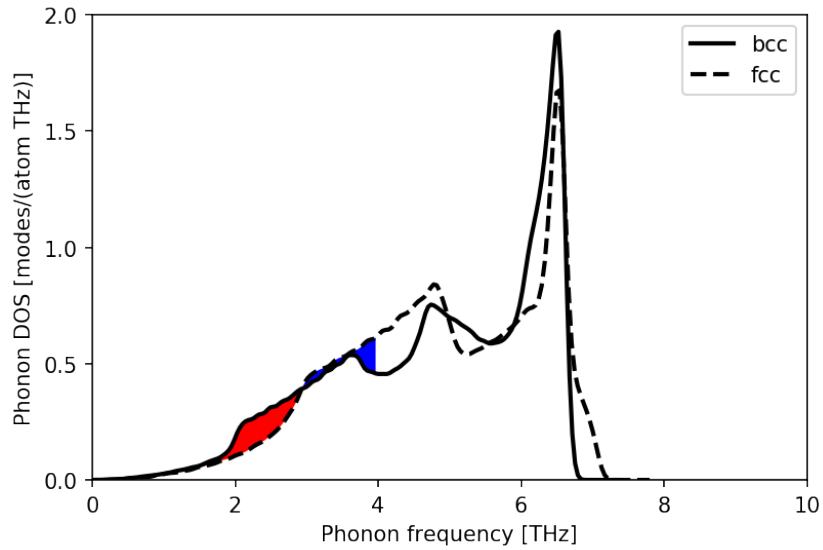


(b) fcc iron

Figure 5.18: Phonon density of states (DOS) of bcc and fcc iron at finite magnetic temperature. The shaded area indicates the gain of low-frequency (less than 4 THz) phonon modes from 300 K to 1700 K.



(a) 300 K



(b) 1700 K

Figure 5.19: Phonon density of states (DOS) of bcc and fcc iron at magnetic temperature of 300 K and 1700 K. The green (red) shaded region indicates low-frequency (less than 4 THz) phonon modes at which fcc iron has higher (lower) phonon DOS.

free-energy difference with temperature. This result can also be interpreted in a simple and naive way: at high temperature where the magnetic ordering is lost



and doesn't play an important role, the geometrical argument about the atomic vibrations holds that the more open bcc structure has softer phonon modes than the more close-packed fcc structure. In contrast, at low temperature where there is strong magnetic ordering, the ferromagnetic ordering significantly changes the energy landscape of bcc iron and hardens the low-frequency phonon modes to be higher than those of fcc iron.

We next sum up the electronic contribution (calculated through Eq. (5.13) and shown in Fig. 5.14) and the vibrational contribution (calculated through Eq. (5.16) and shown in Fig. 5.17) to the free-energy difference between bcc and fcc iron,

$$\Delta F^{\text{tot}}(T) = \Delta F^{\text{elec}}(T) + \Delta F^{\text{vib}}(T), \quad (5.17)$$

We plot in Fig. 5.20 our calculated free energy difference together with CALPHAD data for comparison [1]. A positive value  $\Delta F^{\text{tot}}(T) > 0$  means that the

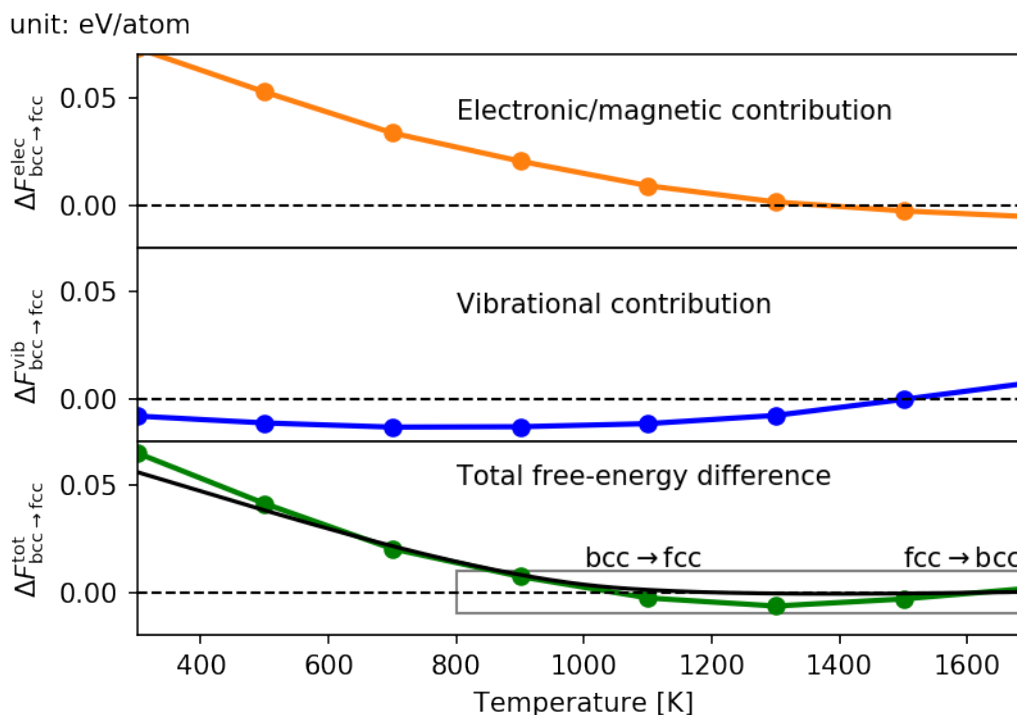


Figure 5.20: The electronic, vibrational and total free-energy differences between bcc and fcc iron plotted as function of temperature (shown as colored dots) in comparison with CALPHAD data [1] (shown as black line).

fcc structure is more stable than the bcc structure at temperature  $T$  whereas a

negative value  $\Delta F^{\text{tot}}(T) < 0$  means that the bcc structure is more stable than the fcc structure at temperature  $T$ . We also plot in Fig. 5.20 separately the electronic and vibrational contributions in Fig. 5.20 for the sake of discussion. At low-temperature region ( $T < 900$  K), the gain of the exchange energy due to the ferromagnetic ordering significantly lowers the internal energy in bcc iron, and the electronic contribution plays a dominant role in determining the total free-energy difference. At high-temperature region ( $T > 900$  K), the electronic contribution decreases to the same energy scale with that of the vibrational contribution, and the competition between the two contributions leads to the  $\alpha$  (bcc) -  $\gamma$  (fcc) -  $\delta$  (bcc) phase transitions. The absolute free-energy difference is in overall good agreement with the CALPHAD data [1] in the whole temperature range. As these phase transitions happen at an energy scale of 1 meV, we do not expect a quantitatively perfect agreement, and at some temperatures our calculated results might be several times larger than the CALPHAD data, as shown in the zoomed plot in Fig. 5.21. We obtain a  $\alpha$  (bcc) -  $\gamma$  (fcc) phase-transition temperature of around 1050 K and a  $\gamma$  (fcc) -  $\delta$  (bcc) phase-transition temperature of around 1600 K, which is in a qualitatively good agreement with the experimental values, around 1189 K for  $\alpha$  -  $\gamma$  and 1662 K  $\gamma$  -  $\delta$  phase transitions [13].

In conclusion, we showed that the magnetic excitations alone can only drive the  $\alpha$  (bcc) -  $\gamma$  (fcc) phase transition and cannot drive  $\gamma$  (fcc) -  $\delta$  (bcc) phase transition, and the latter is mainly driven by the vibrational excitations. Therefore, our work supports the second argument listed in the beginning of this section. Our conclusion is in line with the deduction based on DLM ab initio molecular dynamics [7], DFT+DFMT [81, 83] and experiment [100] but disagrees with the results of simpler models [54, 68].

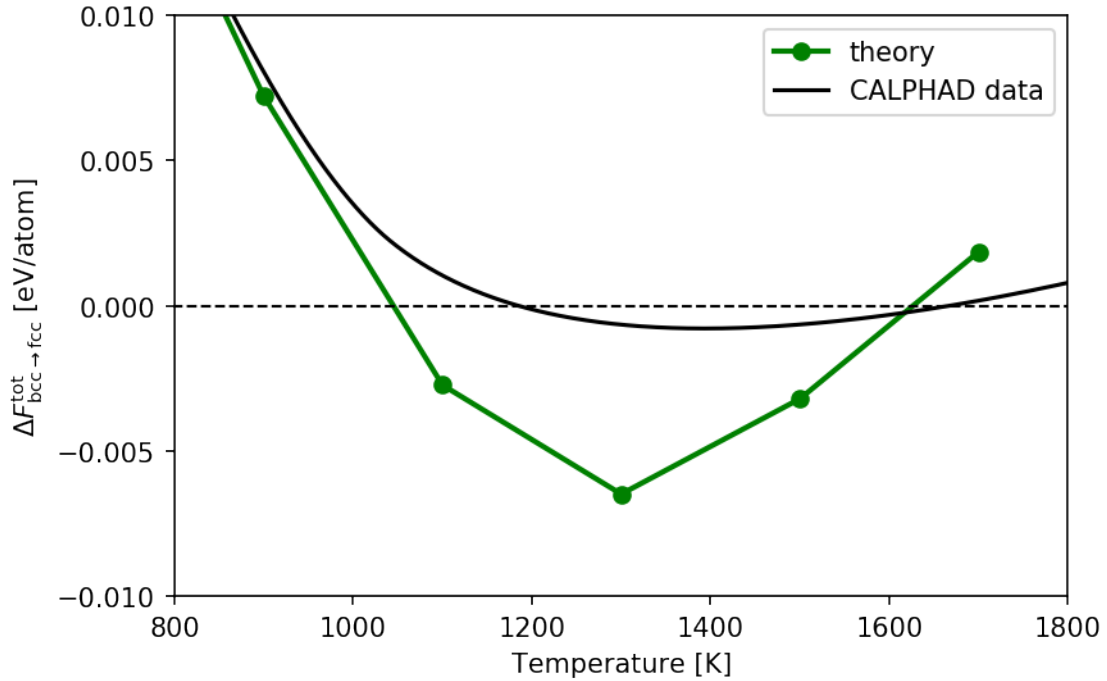


Figure 5.21: The zoomed plot of the grey box in Fig. 5.20.

## 5.5 Summary and conclusion

In the beginning of this chapter, we list three issues we aim to investigate with our methods proposed in the last two chapters. Here are our conclusions.

Regarding the interplay between spin fluctuations and atomic vibrations, we first calculate the effect of spin-fluctuations on phonons using the spin-space averaging scheme and find that the temperature-dependent phonons we obtained are in a surprisingly good agreement with experimental data in the whole temperature range. This gives us the confidence that our model captures the essence of the magnon-phonon coupling in magnetic transition metals even though it is much simpler than density-functional theory or dynamical mean-field theory. We then investigate the effect of atomic vibrations by measuring the magnetization curves for a  $3 \times 3 \times 3$  bcc supercell of iron with fixed and unfixed atomic positions and find that the atomic vibrations have a drastic effect on the collapse of long-range magnetic order. We note that the finite-size effects are to be expected in this calculation and leaves it an open question if this argument still holds for a larger supercell.

Regarding the effect of longitudinal spin fluctuations (LSF), we first evaluate its effect on the magnetic phase transition of iron and find that it pushes upwards the magnetization curve of bcc iron as it excites the magnitude of atomic magnetic moments to higher values. We then perform a thermodynamic integration for the magnetic degrees of freedom along the Bain path and find that LSF favors bcc iron compared to fcc iron both thermodynamically and kinetically though the overall spin fluctuations (transverse plus longitudinal) tends to stabilize fcc iron.

We finally investigate with our methods the microscopic origin of the  $\alpha$  (bcc) -  $\gamma$  (fcc) -  $\delta$  (bcc) phase transitions in iron. We obtain the vibrational free-energy difference between bcc and fcc iron which changes its sign and slope with increasing temperature, in good agreement with the deduction based on experiment that the atomic vibrations tend to stabilize fcc iron at low temperature while at high temperature they tend to stabilize bcc iron [100]. Regarding the electronic contribution, it plays a dominant role at low-temperature range ( $T < 900$  K) where it is much larger than the vibrational contribution and bcc iron is stabilized by the large exchange-energy gain of the ferromagnetic ordering. In the high temperature range ( $T > 900$  K), it decreases to the same energy scale with that of the vibrational contribution due to the loss of ferromagnetic ordering in bcc iron, and the competition between the two contributions leads to  $\alpha$  (bcc) -  $\gamma$  (fcc) -  $\delta$  (bcc) phase transitions in iron. In this temperature range, the electronic contribution decreases from a positive to a negative value while the vibrational contribution increases from a negative to a positive value, and their competition gives a  $\alpha$  (bcc) -  $\gamma$  (fcc) phase-transition temperature of around 1050 K and a  $\gamma$  (fcc) -  $\delta$  (bcc) phase-transition temperature of around 1600 K.

# Chapter 6

## Machine learning for magnetic materials

### 6.1 Introduction

Artificial intelligence (AI) has been referred to as the “fourth industrial revolution” [3]. As the core of AI, the application of machine learning has gone beyond industry and drives a new way for researchers to extract physical laws or knowledge from experiments or simulations [6]. In computational materials science, a well-known problem is to construct the structure-energy relationship, i.e., to calculate the potential energy for a given atomic or magnetic configuration. Machine-learning is playing an increasing role in this problem as the trained machine-learning models can save orders of magnitudes in computational cost of electronic-structure models (ESM) such as DFT, tight-binding, or bond-order potentials, and make it possible to perform large-scale simulations [12, 14, 52]. For non-magnetic materials, there have already been many machine-learning models available, e.g., Gaussian approximation potentials [12], neural-network potentials [14, 52] and moment tensor potentials [114]. However, for magnetic materials, the machine-learning models are still in infancy. As a first step to develop machine-learning approaches for magnetic materials, we propose in this work a neural-network potential for magnetic systems with homogeneous atomic environment. Furthermore, we employ a perturbation approach to correct the error in the thermodynamic calculations with the machine-learning model.

## 6.2 Methodology

### 6.2.1 Neural-network potential

Our neural-network architecture is based upon the one proposed by Behler and Parrinello [14], in which the total potential energy is represented as a sum of atomic contributions  $E_i$ ,

$$E_{\text{MLM}} = \sum_i E_i. \quad (6.1)$$

This neural-network architecture makes use of the locality and translational invariance of the atomic interactions and is transferable or extensible with respect to the size of the supercell. In practice, one may train the neural-network potential with a small supercell and then apply it to perform large-scale simulations.

In our case, the input of the neural networks are spins instead of atomic positions, and the features should represent the symmetry of the spin subspace. If there is no spin-orbit coupling, the spin subspace has global rotational invariance, and this symmetry restriction can be fulfilled by the spin clusters [29]. We choose low-order spin clusters as features, and high-order spin clusters are expected to be generated through neural networks. We show schematically in Fig. 6.1 our neural-network architecture for a system containing four spins. The input are spin vectors  $\mathbf{s}_i$ , which are first transformed into a set of spin clusters  $\{F_i\}$ . These spin clusters describe the magnetic local environment and are the input for the neural networks. The same neural network is employed at different sites, and its output is the atomic contribution to the total energy.

### 6.2.2 Perturbation expansion

In this work, we aim at calculating finite-temperature thermodynamic properties of magnetic materials. For a specific observable  $O$ , its thermal average may be evaluated according to the energy surface of an electronic-structure model  $E_{\text{ESM}}$ ,

$$\langle O_{\text{ESM}} \rangle_{\text{ESM}} = \frac{1}{Z_{\text{ESM}}} \int \prod_i d\mathbf{s}_i \exp[-\beta E_{\text{ESM}}(\{\mathbf{s}_i\})] O^{\text{ESM}}(\{\mathbf{s}_i\}), \quad (6.2)$$

which is accurate but numerically expensive to calculate due to the computational cost of ESM. We use the subscript "ESM" to denote the dependence on the potential energy of the electronic-structure model (ESM). Note that the observable

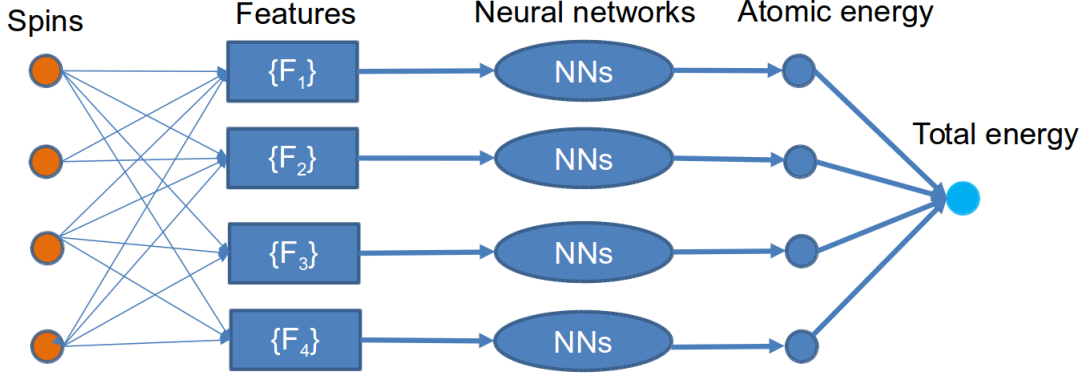


Figure 6.1: Neural-network architecture. Input layer: spin orientations of all atoms. Output layer: total energy as a sum of atomic energies.

itself may depend on the potential energy, and the simplest example is the potential energy itself. We use  $\langle \cdot \rangle_{\text{ESM}}$  to denote the thermal average evaluated according to the canonical distribution of the electronic-structure model,

$$\rho^{\text{ESM}}(\{\mathbf{s}_i\}) = \frac{E_{\text{ESM}}(\{\mathbf{s}_i\})}{Z_{\text{ESM}}}. \quad (6.3)$$

Likewise, the thermal average of this observable can also be evaluated according to the energy surface of a machine-learning model (MLM),

$$\langle O_{\text{MLM}} \rangle_{\text{MLM}} = \frac{1}{Z_{\text{MLM}}} \int \prod_i d\mathbf{s}_i \exp[-\beta E_{\text{MLM}}(\{\mathbf{s}_i\})] O_{\text{MLM}}(\{\mathbf{s}_i\}). \quad (6.4)$$

which is numerically cheap but deviates from Eq. (6.2) because the machine-learning model is fitted to specific samples of the electronic-structure model (ESM) and cannot reproduce its whole energy surface. The deviation between Eq. (6.2) and Eq. (6.4) might be corrected by a perturbation approach, as shown below.

Suppose that we have already trained a machine-learning model,  $E_{\text{MLM}}$ , to reproduce the energy surface of an electronic-structure model, we next perform a

Taylor expansion around it. We first expand the partition function,

$$\begin{aligned}
Z_{\text{ESM}} &= \int \prod_i d\mathbf{s}_i \exp \{-\beta E_{\text{ESM}}(\{\mathbf{s}_i\})\} \\
&= \int \prod_i d\mathbf{s}_i \exp \{-\beta [E_{\text{MLM}}(\{\mathbf{s}_i\}) + \Delta E(\{\mathbf{s}_i\})]\} \\
&= \int \prod_i d\mathbf{s}_i \exp \{-\beta E_{\text{MLM}}(\{\mathbf{s}_i\})\} \cdot \left\{ 1 + [-\beta \Delta E(\{\mathbf{s}_i\})] + \frac{1}{2} [-\beta \Delta E(\{\mathbf{s}_i\})]^2 + \dots \right\},
\end{aligned} \tag{6.5}$$

where we introduced the energy difference  $\Delta E(\{\mathbf{s}_i\}) = E_{\text{ESM}}(\{\mathbf{s}_i\}) - E_{\text{MLM}}(\{\mathbf{s}_i\})$ . We denote  $\frac{-\Delta E}{k_{\text{B}}T}$  as  $\chi$ , and for simplicity, we omit in the following formulas the configurational-variable dependence ( $\{\mathbf{s}_i\}$ ) of  $E$ ,  $\Delta E$ ,  $\chi$ , and  $O$ . We then reformulate Eq. (6.5) as

$$\begin{aligned}
Z_{\text{ESM}} &= \int \prod_i d\mathbf{s}_i \exp(-\beta E_{\text{MLM}}) \cdot \left( 1 + \chi + \frac{1}{2} \chi^2 + \dots \right) \\
&= Z_{\text{MLM}} (1 + \langle \chi \rangle_{\text{MLM}} + \frac{1}{2} \langle \chi^2 \rangle_{\text{MLM}} + \dots).
\end{aligned} \tag{6.6}$$

We next expand the numerator in Eq. 6.2,

$$\begin{aligned}
&\int \prod_i d\mathbf{s}_i \exp(-\beta E_{\text{ESM}}) O_{\text{ESM}} = \\
&\int \prod_i d\mathbf{s}_i \exp[-\beta E_{\text{MLM}}] \cdot \left[ 1 + \chi + \frac{1}{2} \chi^2 + \dots \right] \\
&\cdot \left[ O_{\text{MLM}} + \frac{\partial O_{\text{ESM}}}{\partial E_{\text{ESM}}} \Delta E + \frac{1}{2} \frac{\partial^2 O_{\text{ESM}}}{\partial E_{\text{ESM}}^2} (\Delta E)^2 + \dots \right].
\end{aligned} \tag{6.7}$$

We then insert Eq. 6.6 and Eq. 6.7 into Eq. 6.2 and employ the Taylor expansion for  $\frac{1}{1+x}$ . If we only keep the zeroth-order term of  $\chi$ , we obtain

$$\langle O_{\text{ESM}} \rangle_{\text{ESM}}^{(0)} = \langle O_{\text{MLM}} \rangle_{\text{MLM}}. \tag{6.8}$$

The zeroth-order approximation is nothing but to directly take the thermal average with respect to the machine-learning potential.

The first-order approximation gives

$$\begin{aligned}
\langle O_{\text{ESM}} \rangle_{\text{ESM}}^{(1)} &= \langle O_{\text{ESM}} \rangle_{\text{ESM}}^{(0)} + \left\langle \frac{\partial O_{\text{ESM}}}{\partial E_{\text{ESM}}} \Delta E \right\rangle_{\text{MLM}} + \langle O_{\text{MLM}} \chi \rangle_{\text{MLM}} - \langle O_{\text{MLM}} \rangle_{\text{MLM}} \langle \chi \rangle_{\text{MLM}} \\
&\equiv \langle O_{\text{ESM}} \rangle_{\text{ESM}}^{(0)} + \left\langle \frac{\partial O_{\text{ESM}}}{\partial E_{\text{ESM}}} \Delta E \right\rangle_{\text{MLM}} + \text{cov}(O_{\text{MLM}}, \chi),
\end{aligned} \tag{6.9}$$



where  $\text{cov}(O_{\text{MLM}}, \chi)$  is the covariance between  $O_{\text{MLM}}$  and  $\chi$ .

The second-order approximation gives

$$\begin{aligned}
\langle O \rangle_{\text{ESM}}^{(2)} &\approx \langle O_{\text{ESM}} \rangle_{\text{ESM}}^{(1)} + \frac{1}{2} \left\langle \frac{\partial^2 O_{\text{ESM}}}{\partial E_{\text{ESM}}^2} (\Delta E)^2 \right\rangle_{\text{MLM}} \\
&\quad + \left\langle \frac{\partial O_{\text{ESM}}}{\partial E_{\text{ESM}}} \Delta E \chi \right\rangle_{\text{MLM}} - \left\langle \frac{\partial O_{\text{ESM}}}{\partial E_{\text{ESM}}} \Delta E \right\rangle_{\text{MLM}} \langle \chi \rangle_{\text{MLM}} \\
&\quad + \langle \chi \rangle_{\text{MLM}} (\langle O_{\text{MLM}} \rangle_{\text{MLM}} \langle \chi \rangle_{\text{MLM}} - \langle O_{\text{MLM}} \chi \rangle_{\text{MLM}}) \\
&\quad + \frac{1}{2} (\langle O_{\text{MLM}} \chi^2 \rangle_{\text{MLM}} - \langle O_{\text{MLM}} \rangle_{\text{MLM}} \langle \chi^2 \rangle_{\text{MLM}}) \\
&\equiv \langle O_{\text{ESM}} \rangle_{\text{ESM}}^{(1)} + \frac{1}{2} \left\langle \frac{\partial^2 O_{\text{ESM}}}{\partial E_{\text{ESM}}^2} (\Delta E)^2 \right\rangle_{\text{MLM}} + \text{cov} \left( \frac{\partial O_{\text{ESM}}}{\partial E_{\text{ESM}}} \Delta E, \chi \right) \\
&\quad - \langle \chi \rangle_{\text{MLM}} \text{cov}(O_{\text{MLM}}, \chi) + \frac{1}{2} \text{cov}(O_{\text{MLM}}, \chi^2)
\end{aligned} \tag{6.10}$$

We may continue the expansion to include higher-order terms.

We take two examples to show how to apply this method. In the first example, we aim at evaluating the thermal average of potential energy, and in the second example, we apply this approach to calculate the free-energy difference between MLM and ESM. We truncate the perturbation expansion to the second order in both examples.

For the potential energy, the second-order approximation is simply given as

$$\begin{aligned}
\langle E_{\text{ESM}} \rangle_{\text{ESM}}^{(2)} &= \langle E_{\text{MLM}} \rangle_{\text{MLM}} + \langle \Delta E \rangle_{\text{MLM}} + \text{cov}(E_{\text{MLM}}, \chi) \\
&\quad + \text{cov}(\Delta E, \chi) - \langle \chi \rangle_{\text{MLM}} \text{cov}(E_{\text{MLM}}, \chi) + \frac{1}{2} \text{cov}(E_{\text{MLM}}, \chi^2). \tag{6.11} \\
&\equiv \langle E_{\text{MLM}} \rangle_{\text{MLM}} + \langle \Delta E \rangle_{\text{MLM}} + \text{cov}(E_{\text{MLM}}, \chi) + \Delta_{\text{corr}}^{(2)}
\end{aligned}$$

We will check the convergence of each term in the next subsection.

We next apply this perturbation approach to thermodynamic integration in order to evaluate the free-energy difference between MLM and ESM. The free energy for the machine-learning potential  $F_{\text{MLM}}$  is computationally cheap to calculate, and the free-energy difference between the machine-learning model and the electronic-structure model can be evaluated formally with thermodynamic integration,

$$\begin{aligned}
F_{\text{ESM}} - F_{\text{MLM}} &= \int_0^1 d\lambda \langle E_{\text{ESM}} - E_{\text{MLM}} \rangle_{\lambda} \\
&\equiv \int_0^1 d\lambda \langle \Delta E \rangle_{\lambda},
\end{aligned} \tag{6.12}$$

where the thermal average on the right-hand side is defined as,

$$\langle \Delta E \rangle_\lambda = \frac{1}{Z_\lambda} \int \prod_i d\mathbf{s}_i (E_{\text{ESM}} - E_{\text{MLM}}) e^{-\beta E_\lambda(\{\mathbf{s}_i\})}. \quad (6.13)$$

The subscript  $\lambda$  represents that the thermal average is evaluated with respect to the energy surface of

$$\begin{aligned} E_\lambda &= (1 - \lambda)E_{\text{MLM}} + \lambda E_{\text{ESM}} \\ &= E_{\text{MLM}} + \lambda \Delta E, \end{aligned} \quad (6.14)$$

and  $\chi$  in Eq. (6.8), (6.9), and (6.10) should be interpreted as  $\chi = -\beta\lambda\Delta E$ .

In this case, the observable is  $O_{\text{ESM}} = E_{\text{ESM}} - E_{\text{MLM}} \equiv \Delta E$ , and the corresponding zeroth-order terms  $O_{\text{MLM}}$  and  $\langle O_{\text{ESM}} \rangle_\lambda^{(0)}$  vanish.

If we include the first-order correction, we obtain

$$\langle \Delta E \rangle_\lambda \approx \langle \Delta E \rangle_{\text{MLM}}, \quad (6.15)$$

and

$$F_{\text{ESM}} - F_{\text{MLM}} \approx \langle \Delta E \rangle_{\text{MLM}}. \quad (6.16)$$

If we continue to include the second-order correction, we obtain

$$\langle \Delta E \rangle_\lambda \approx \langle \Delta E \rangle_{\text{MLM}} - \lambda\beta \text{var}(\Delta E), \quad (6.17)$$

and

$$F_{\text{ESM}} - F_{\text{MLM}} \approx \langle \Delta E \rangle_{\text{MLM}} - \frac{1}{2}\beta \text{var}(\Delta E). \quad (6.18)$$

The results Eq. (6.15) - (6.18) can also be understood from a different point of view. As the derivative of the free-energy difference,  $\langle \Delta E \rangle_\lambda$ , is a function of the switching parameter  $\lambda$ , we may perform a Taylor expansion of this quantity with respect to  $\lambda$ . The zeroth-order term is simply  $\langle \Delta E \rangle_{\text{MLM}}$ , and the first-order derivative is

$$\begin{aligned} \frac{\partial}{\partial \lambda} \langle \Delta E \rangle_\lambda &= -\beta (\langle \Delta E^2 \rangle_\lambda - \langle \Delta E \rangle_\lambda^2) \\ &\equiv -\beta \text{Var}(\Delta E)_\lambda. \end{aligned} \quad (6.19)$$

We therefore recover Eq. (6.15) - (6.18) by Taylor expanding  $\langle \Delta E \rangle_\lambda$  to the first order.

We notice that the first-order approximation, Eq. (6.16), offers an upper bound of the free-energy difference,

$$F_{\text{ESM}} - F_{\text{MLM}} \leq \langle \Delta E \rangle_{\text{MLM}}, \quad (6.20)$$

which is nothing but the Peierls-Feynman inequality [38, 104]. We may prove this inequality easily with Eq. 6.19 which states that the derivative of the free-energy difference,  $\langle \Delta E \rangle_\lambda$ , is a decreasing function of  $\lambda$ . The role of the negative second-order correction term in Eq. (6.18) is to reduce the upper bound (6.16) to a value that is closer to the exact free-energy difference.

### 6.3 Result

We choose the magnetic bond-order potential of iron [95] as an example ESM and the neural-network potential illustrated in Fig. 6.1 as an example MLM in order to test the methodology proposed in the last subsection. We generate the training data set with the magnetic bond-order potential of iron [95] for a  $5 \times 5 \times 5$  bcc supercell of iron containing 250 spins. Ideally, the samples in the training data set should uniformly cover the whole energy landscape and should be not correlated. In practice, we first run HMC with a classical Heisenberg model [89] at the Curie temperature of iron ( $T_C$ ),  $0.95 T_C$  and  $1.6 T_C$ , and then randomly choose 2800 samples from the HMC trajectories. The potential energies of the samples are calculated with the magnetic bond-order potential of iron and form the output values of the training data set. We choose pair-spin clusters  $\mathbf{s}_i \cdot \mathbf{s}_j$  and three-spin clusters  $(\mathbf{s}_i \cdot \mathbf{s}_j) \cdot (\mathbf{s}_i \cdot \mathbf{s}_j)$  as feature functions in our neural networks and include pairwise spin clusters up to six-nearest neighbours and the first-nearest neighbour three-spin cluster. As shown in 2.1, the activation function is required to introduce non-linearity into the neural network. In practice, we choose the exponential-linear-units [25] as the activation function. The loss function is chosen as the mean-squared error of the training and the predicted potential energies and we employ TensorFlow [4] to train our model. Our training procedure consists of two steps. We first perform a linear regression to get a good initial guess of the weights, which are then used as the initial parameters in the training of the neural network.

After we train the neural-network potential, we calculate the errors between the training and predicted potential energies of the samples in the training data set and plot them in Fig. 6.2. The absolute values of all errors are smaller than one meV per atom for almost all samples, and the root-mean-squared error is 0.25 meV/atom in the training data set. We first check the convergence of each correction terms in the second-order approximation for the thermal average of

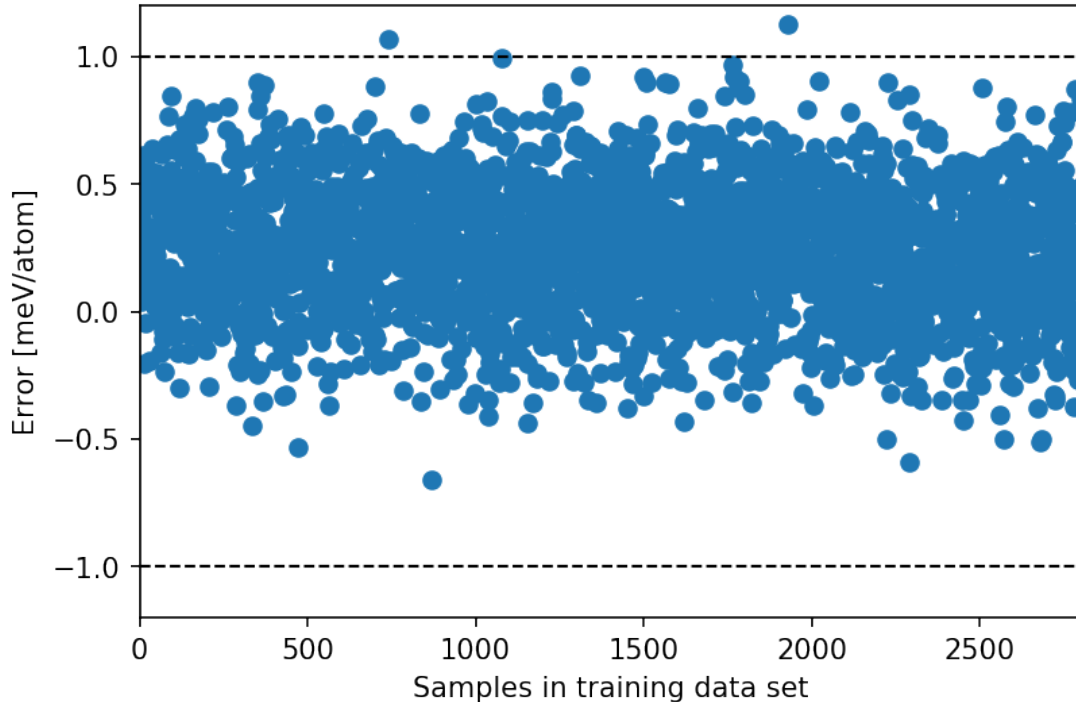


Figure 6.2: Errors between the training and predicted potential energies of the samples in the training data set.

potential energy, Eq. (6.11), and show the running averages in Fig. 6.3. In this calculation, we first generate a HMC trajectory with the neural-network potential at a given temperature, and then randomly choose one thousand uncorrelated samples from the trajectory. The computational cost of this phase is negligible due to the high efficiency of MLM. In the second phase, we calculate with the magnetic bond-order potential the potential energies of the chosen samples in order to evaluate the correction terms in Eq. (6.11),  $\langle \Delta E \rangle_{\text{MLM}}$ ,  $\text{cov}(E_{\text{MLM}}, \chi)$ , and  $\Delta_{\text{corr}}^{(2)}$ . The second phase dominates the computational cost due to the low efficiency of ESM. We see in Fig. 6.3 that the two first-order correction terms,  $\langle \Delta E \rangle_{\text{MLM}}$  and  $\text{cov}(E_{\text{MLM}}, \chi)$ , have different rate of convergence and different contribution to the correction. The convergence of  $\langle \Delta E \rangle_{\text{MLM}}$  is much faster than that of  $\text{cov}(E_{\text{MLM}}, \chi)$  whereas the contribution of the later is several times larger than that of the former. Both of them are converged within 1 meV/atom with 200 samples. The second-order correction term  $\Delta_{\text{corr}}^{(2)}$  is smaller than 0.5 meV/atom and negligible compared to the first-order correction term.

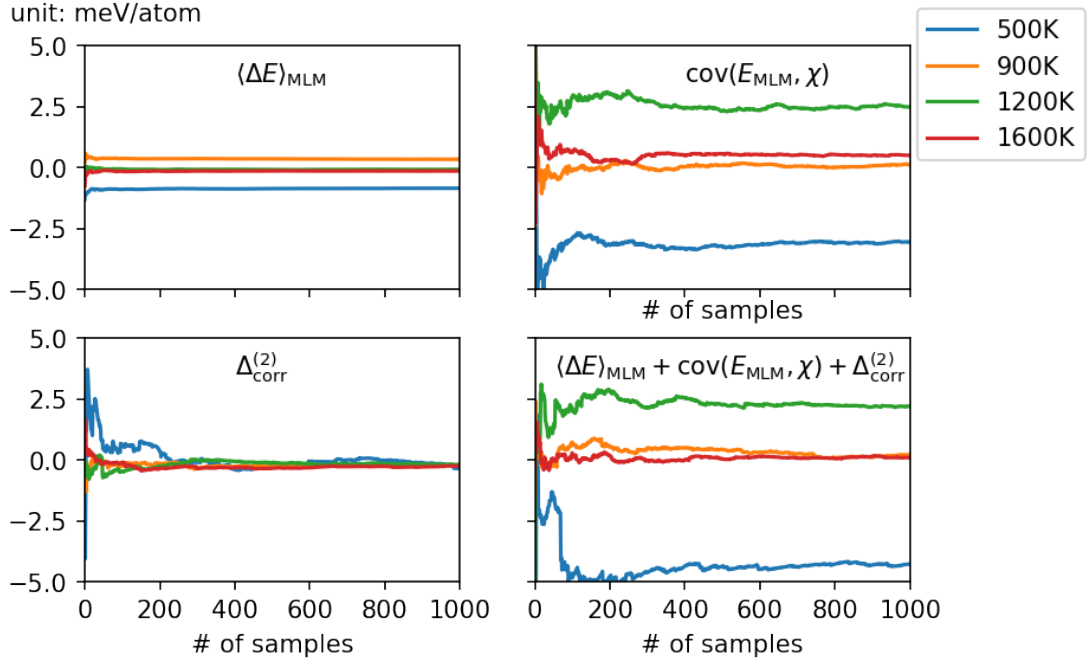


Figure 6.3: Running average of the correction terms in the second-order approximation for the thermal average of potential energy at 500 K, 900 K, 1200 K, and 1600 K.  $\langle \Delta E \rangle_{\text{MLM}}$  and  $\text{cov}(E_{\text{MLM}}, \chi)$  are the two first-order correction terms. The second-order correction terms are grouped into  $\Delta_{\text{corr}}^{(2)}$ .

We then calculate the errors of the zeroth-order, first-order, and second-order approximation of the thermal average of potential energy,  $\langle E_{\text{ESM}} \rangle_{\text{ESM}} - \langle E_{\text{ESM}} \rangle_{\text{ESM}}^{(i)}$ , with  $i = 0, 1, 2$ , and show the results in Fig. 6.4. The exact value  $\langle E_{\text{ESM}} \rangle_{\text{ESM}}$  is calculated

with the method in Chapter 4 and shown in Fig. 4.8. The zeroth-order approximation has an error larger than 1 meV/atom at some temperatures. The inclusion of the first-order correction reduces the error to be smaller than 1 meV/atom at all temperatures. The second-order correction further reduces the error and plays a less important role.

We next check the convergence of the two terms in the second-order approximation of the free-energy difference between ESM and MLM, Eq. (6.18), and plot the running averages in Fig. 6.5. Both the first-order and the second-order correction terms are well converged within 100 samples. The second-order correction

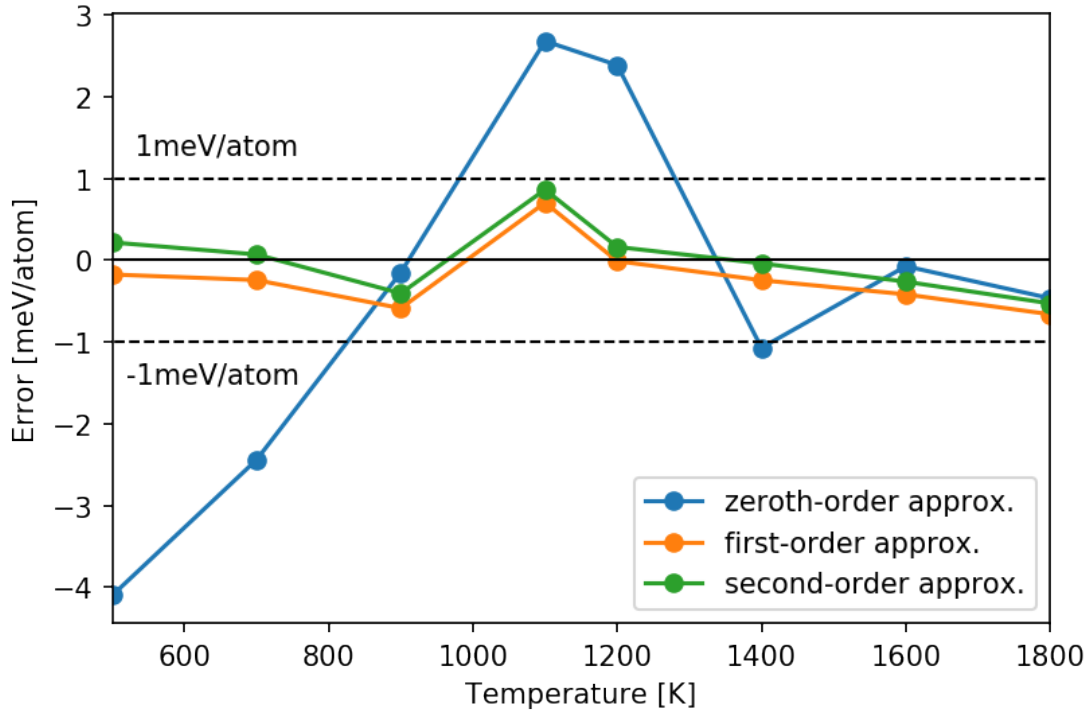


Figure 6.4: Error of thermal-average potential energies at different temperatures for the zeroth-order, first-order, and second-order approximation.

is smaller than 0.5 meV for all temperatures, which indicates that the MLM is well trained to reproduce the whole energy surface of the ESM and the first-order approximation is sufficient to achieve an accuracy of less than one meV for the estimation of the free-energy difference between ESM and MLM.

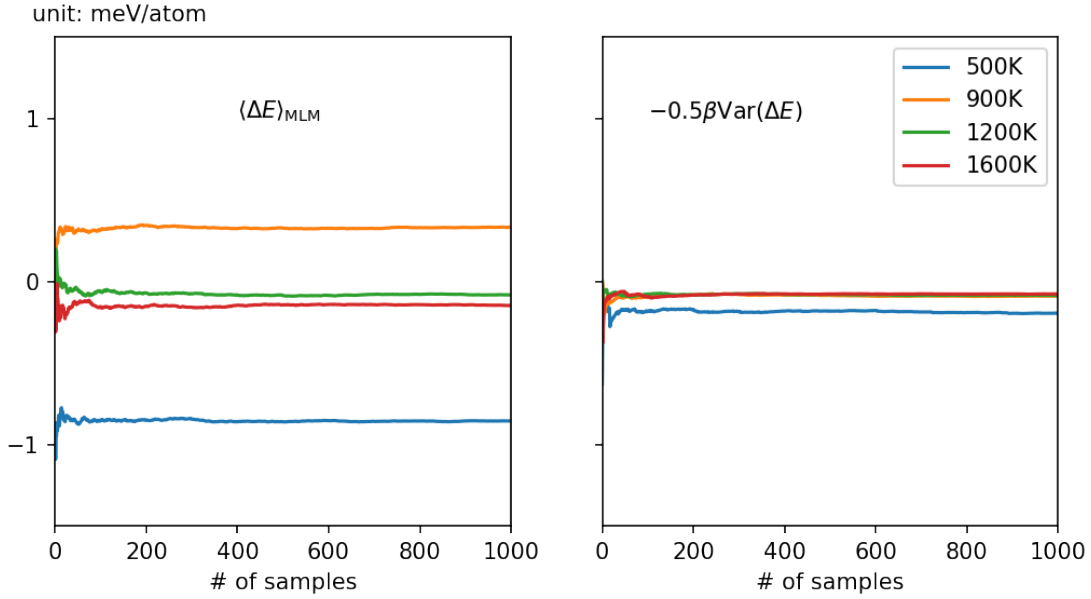


Figure 6.5: Running average of the first-order and second-order correction terms for the free-energy difference between MSM and ELM.

## 6.4 Conclusion

We develop a perturbation approach in order to accelerate ab-initio thermodynamics by using machine learning, and a neural-network potential for spin interactions, which is extensible with the size of the supercell and contains moderate number of parameters. We employ a two-step procedure to train the neural network with the linear regression in the first step to obtain a good initial guess of weights and a standard neural-network training in the second step. Our test with the magnetic bond-order potential shows that the fast converged first-order correction reduces the error of the thermal average to be within one meV in the whole temperature range.

# Chapter 7

## Conclusion and outlook

### 7.1 Conclusion

We propose a tight-binding model for atomistic simulations of magnetic transition metals at finite temperature. In this model, the transverse and longitudinal spin fluctuations are treated with the Hubbard-Stratonovich transformation and the static approximation, the atomic vibrations are treated with the conventional tight-binding, and these excitations are coupled via electronic structures. The original magnetic tight binding [11, 33, 102] is shown to be the magnetic ground-state solution of our model. Besides, we develop Hamiltonian Monte Carlo algorithms in order to efficiently sample the spin space. Our tests with the classical Heisenberg model and magnetic bond-order potential show that our algorithms have reasonably small dynamical critical exponent and fast decorrelation of Monte Carlo samples. In order to further accelerate the thermodynamic calculations of magnetic materials, we develop a machine-learning based perturbation approach. Good accuracy has been shown in our preliminary test with magnetic bond-order potentials.

As a benchmark test of our methods, the calculated magnon-phonon coupling in bcc iron is in excellent agreement with experimental data. We then apply our methods to investigate the effect of longitudinal spin fluctuations (LSF) on structural phase transitions of iron and find that LSF favors bcc iron compared to fcc iron both thermodynamically and kinetically though the overall spin fluctuations (transverse plus longitudinal) tends to stabilize fcc iron. More interestingly, we observe an interesting competition between the electronic (magnetic) and vibrational contributions to the free-energy difference between bcc and fcc iron, and



this leads to the unique temperature-induced  $\alpha$  (bcc) -  $\gamma$  (fcc) -  $\delta$  (bcc) phase transitions in iron. The calculated vibrational free-energy difference between bcc and fcc iron changes its sign at around 1500 K, which is in a good agreement with the deduction based on experiments. The calculated electronic contribution plays a dominant role at low-temperature range ( $T < 900$  K) and at high-temperature range ( $T > 900$  K) decreases to the same energy scale with that of the vibrational contribution due to the loss of ferromagnetic ordering in bcc iron. Their competition gives a  $\alpha$  (bcc) -  $\gamma$  (fcc) phase-transition temperature of around 1050 K and a  $\gamma$  (fcc) -  $\delta$  (bcc) phase-transition temperature of around 1600 K in our result, which are in a good agreement with experimental values.

## 7.2 Outlook

Our work offers a solid pillar towards large-scale simulations of magnetic transition metals, and it is not the end of the story. We list several interesting issues that may be explored in the future:

- In our model in chapter 3, we employed two key approximations: the tight-binding approximation and the static approximation. In the former, the hopping integral is parametrized as a function of distance and a pair-wise term is added to the potential energy to account for all remaining contributions. In the latter, we neglect the quantum fluctuations described by the imaginary time and simplify the partition function from a path integral to an ordinary integral. As the modelling of magnetic transition metals is fundamentally a many-body problem, these approximations are not avoidable in order to obtain a practical model for computer simulations. The question is: can we know the error bar of these approximations? Which materials-science problems are they applicable to?
- The algorithms we developed in chapter 4 are based on Hamiltonian Monte Carlo and designed to sample the spin space. We may extend these algorithms to sample both the spin space and atomic space, and may further include the volume degrees of freedom to deal with the grand-canonical ensemble. Actually, Hamiltonian Monte Carlo has gained great progress and

become a widely used approach in the community of Bayesian analysis [17–19, 47, 58, 98, 133], while it attracts the interest of the community of computational materials science only recently [106].

- In chapter 6, we proposed a preliminary machine-learning model for magnetic interactions, and treated the global rotational symmetry with spin clusters. The next step would be to find an approach to treat the permutation symmetry, and a further step would be to combine it with the machine-learning models for non-magnetic materials to get a full description of magnetic materials.

# Bibliography

- [1] The CALPHAD data were offered by Fritz Körmann who obtained them with the thermocalc program and the SGTE unary database.
- [2] [http://inac.cea.fr/l\\_sim/v\\_sim/](http://inac.cea.fr/l_sim/v_sim/).
- [3] <https://www.foreignaffairs.com/articles/2015-12-12/fourth-industrial-revolution>.
- [4] <https://www.tensorflow.org/>.
- [5] I. A. Abrikosov, A. V. Ponomareva, P. Steneteg, S. A. Barannikova, and B. Alling. Recent progress in simulations of the paramagnetic state of magnetic materials. *Current Opinion in Solid State and Materials Science*, 20(2):85 – 106, 2016.
- [6] A. Agrawal and A. Choudhary. Perspective: Materials informatics and big data: Realization of the fourth paradigm of science in materials science. *APL Materials*, 4(5):053208, 2016.
- [7] B. Alling, F. Körmann, B. Grabowski, A. Glensk, I. A. Abrikosov, and J. Neugebauer. Strong impact of lattice vibrations on electronic and magnetic properties of paramagnetic fe revealed by disordered local moments molecular dynamics. *Physical Review B*, 93:224411, 2016.
- [8] V. Ambegaokar and M. Troyer. Estimating errors reliably in monte carlo simulations of the ehrenfest model. *American Journal of Physics*, 78(2):150–157, 2010.
- [9] V. P. Antropov, M. I. Katsnelson, B. N. Harmon, M. van Schilfgaarde, and D. Kusnezov. Spin dynamics in magnets: Equation of motion and finite temperature effects. *Physical Review B*, 54:1019–1035, 1996.

- [10] V. P. Antropov, M. I. Katsnelson, M. van Schilfgaarde, and B. N. Harmon. Ab initio spin dynamics in magnets. *Physical Review Letters*, 75:729–732, 1995.
- [11] C. Barreteau, D. Spanjaard, and M. C. Desjonquères. An efficient magnetic tight-binding method for transition metals and alloys. *Comptes Rendus Physique*, 17(3):406 – 429, 2016.
- [12] A. P. Bartók, M. C. Payne, R. Kondor, and G. Csányi. Gaussian approximation potentials: The accuracy of quantum mechanics, without the electrons. *Physical Review Letters*, 104:136403, 2010.
- [13] Z. S. Basinski, W. Hume-Rothery, and A. L. Sutton. The lattice expansion of iron. *Proceedings of the Royal Society of London. Series A. Mathematical and Physical Sciences*, 229(1179):459–467, 1955.
- [14] J. Behler and M. Parrinello. Generalized neural-network representation of high-dimensional potential-energy surfaces. *Physical Review Letters*, 98:146401, 2007.
- [15] A. S. Belozarov and V. I. Anisimov. Coulomb interaction parameters in bcc iron: an LDA+DMFT study. *Journal of Physics: Condensed Matter*, 26(37):375601, 2014.
- [16] Y. Bengio, P. Lamblin, D. Popovici, and H. Larochelle. Greedy layer-wise training of deep networks. In *Proceedings of the 19th International Conference on Neural Information Processing Systems, NIPS’06*, pages 153–160, Cambridge, MA, USA, 2006. MIT Press.
- [17] A. Beskos, N. S. Pillai, G. O. Roberts, J. M. Sanz-Serna, and A. M. Stuart. Optimal tuning of the hybrid Monte Carlo algorithm. *Bernoulli*, 19(5A):1501–1534, 2013.
- [18] M. Betancourt. A Conceptual Introduction to Hamiltonian Monte Carlo. *ArXiv e-prints*, 2017.
- [19] M. Betancourt, S. Byrne, S. Livingstone, and M. Girolami. The geometric foundations of Hamiltonian Monte Carlo. *Bernoulli*, 23(4A):2257–2298, 2017.

- [20] F. R. Brown and T. J. Woch. Overrelaxed heat-bath and metropolis algorithms for accelerating pure gauge Monte Carlo calculations. *Physical Review Letters*, 58:2394–2396, 1987.
- [21] M. Čák, T. Hammerschmidt, and R. Drautz. Comparison of analytic and numerical bond-order potentials for w and mo. *Journal of Physics: Condensed Matter*, 25(26):265002, 2013.
- [22] M. Čák, T. Hammerschmidt, J. Rogal, V. Vitek, and R. Drautz. Analytic bond-order potentials for the bcc refractory metals Nb, Ta, Mo and W. *Journal of Physics: Condensed Matter*, 26(19):195501, 2014.
- [23] H. Capellmann. The magnetism of iron and other 3-d transition metals. *Journal of Magnetism and Magnetic Materials*, 28(3):250 – 260, 1982.
- [24] C. Chipot and A. Pohorille, editors. *Free Energy Calculations: Theory and Applications in Chemistry and Biology*, volume 86 of *Springer Series in Chemical Physics*. Springer-Verlag, Berlin, 2007.
- [25] D. A. Clevert, T. Unterthiner, and S. Hochreiter. Fast and accurate deep network learning by exponential linear units (elus). *CoRR*, abs/1511.07289, 2015.
- [26] M. Creutz. Overrelaxation and Monte Carlo simulation. *Physical Review D*, 36:515–519, 1987.
- [27] F. Cyrot-Lackmann. On the electronic structure of liquid transitional metals. *Advances in Physics*, 16(63):393–400, 1967.
- [28] F. Dietermann, L. M. Sandratskii, and M. Fähnle. On the energetics of transversal and longitudinal fluctuations of atomic magnetic moments. *Journal of Magnetism and Magnetic Materials*, 324(18):2693 – 2695, 2012.
- [29] R. Drautz and M. Fähnle. Spin-cluster expansion: Parametrization of the general adiabatic magnetic energy surface with ab initio accuracy. *Physical Review B*, 69:104404, 2004.
- [30] R. Drautz and M. Fähnle. Parametrization of the magnetic energy at the atomic level. *Physical Review B*, 72:212405, Dec 2005.

- [31] R. Drautz, T. Hammerschmidt, M. Čák, and D. G. Pettifor. Bond-order potentials: derivation and parameterization for refractory elements. *Modelling and Simulation in Materials Science and Engineering*, 23(7):074004, 2015.
- [32] R. Drautz and D. G. Pettifor. Valence-dependent analytic bond-order potential for transition metals. *Physical Review B*, 74:174117, 2006.
- [33] R. Drautz and D. G. Pettifor. Valence-dependent analytic bond-order potential for magnetic transition metals. *Physical Review B*, 84:214114, 2011.
- [34] S. Duane, A. D. Kennedy, B. J. Pendleton, and D. Roweth. Hybrid Monte Carlo. *Physics Letters B*, 195(2):216 – 222, 1987.
- [35] S. L. Dudarev and P. M. Derlet. A 'magnetic' interatomic potential for molecular dynamics simulations. *Journal of Physics: Condensed Matter*, 17(44):7097, 2005.
- [36] A. I. Duff, T. Davey, D. Korbmacher, A. Glensk, B. Grabowski, J. Neugebauer, and M. W. Finnis. Improved method of calculating ab initio high-temperature thermodynamic properties with application to ZrC. *Physical Review B*, 91:214311, 2015.
- [37] M. Eisenbach, D. M. Nicholson, A. Rusanu, and G. Brown. First principles calculation of finite temperature magnetism in Fe and Fe<sub>3</sub>C. *Journal of Applied Physics*, 109(7):07E138, 2011.
- [38] R. P. Feynman. Slow electrons in a polar crystal. *Physical Review*, 97:660–665, 1955.
- [39] M. W. Finnis. *Interatomic Forces in Condensed Matter*. Oxford series on materials modelling, 1. Oxford University Press, 2003.
- [40] M. W. Finnis, A. T. Paxton, M. Methfessel, and M. van Schilfhaarde. Crystal structures of zirconia from first principles and self-consistent tight binding. *Physical Review Letters*, 81:5149–5152, 1998.
- [41] M. W. Finnis and J. E. Sinclair. A simple empirical N-body potential for transition metals. *Philosophical Magazine A*, 50(1):45–55, 1984.

- [42] M. E. Ford, R. Drautz, T. Hammerschmidt, and D. G. Pettifor. Convergence of an analytic bond-order potential for collinear magnetism in Fe. *Modelling and Simulation in Materials Science and Engineering*, 22(3):034005, 2014.
- [43] M. E. Ford, R. Drautz, T. Hammerschmidt, and D. G. Pettifor. Convergence of an analytic bond-order potential for collinear magnetism in fe. *Modelling and Simulation in Materials Science and Engineering*, 22(3):034005, 2014.
- [44] M. E. Ford, D. G. Pettifor, and R. Drautz. Non-collinear magnetism with analytic bond-order potentials. *Journal of Physics: Condensed Matter*, 27(8):086002, 2015.
- [45] A. Georges, G. Kotliar, W. Krauth, and M. J. Rozenberg. Dynamical mean-field theory of strongly correlated fermion systems and the limit of infinite dimensions. *Rev. Mod. Phys.*, 68:13–125, 1996.
- [46] T. L. Gilbert. A phenomenological theory of damping in ferromagnetic materials. *IEEE Transactions on Magnetics*, 40(6):3443–3449, 2004.
- [47] M. Girolami and B. Calderhead. Riemann manifold langevin and Hamiltonian Monte Carlo methods. *Journal of the Royal Statistical Society: Series B (Statistical Methodology)*, 73(2):123–214, 2011.
- [48] B. Grabowski, L. Ismer, T. Hickel, and J. Neugebauer. Ab initio up to the melting point: anharmonicity and vacancies in aluminum. *Physical Review B*, 79:134106, 2009.
- [49] B. L. Gyorffy, A. J. Pindor, J. Staunton, G. M. Stocks, and H. Winter. A first-principles theory of ferromagnetic phase transitions in metals. *Journal of Physics F: Metal Physics*, 15(6):1337, 1985.
- [50] T. Hammerschmidt, B. Seiser, M. E. Ford, A. N. Ladines, S. Schreiber, N. Wang, J. Jenke, Y. Lysogorskiy, C. Teijeiro, M. Mrovec, M. Cak, E. R. Margine, D. G. Pettifor, and R. Drautz. BOPfox program for tight-binding and analytic bond-order potential calculations. *Computer Physics Communications*, 235:221 – 233, 2019.

- [51] Q. Han, T. Birol, and K. Haule. Phonon softening due to melting of the ferromagnetic order in elemental iron. *Physical Review Letters*, 120:187203, 2018.
- [52] C. M. Handley and P. L. A. Popelier. Potential energy surfaces fitted by artificial neural networks. *The Journal of Physical Chemistry A*, 114(10):3371–3383, 2010.
- [53] H. Hasegawa. Single-site spin fluctuation theory of itinerant-electron systems with narrow bands. ii. iron and nickel. *Journal of the Physical Society of Japan*, 49(3):963–971, 1980.
- [54] H. Hasegawa and D. G. Pettifor. Microscopic theory of the temperature-pressure phase diagram of iron. *Physical Review Letters*, 50:130–133, 1983.
- [55] O. Hellman, P. Steneteg, I. A. Abrikosov, and S. I. Simak. Temperature dependent effective potential method for accurate free energy calculations of solids. *Physical Review B*, 87:104111, 2013.
- [56] G. E. Hinton, S. Osindero, and Y. Teh. A fast learning algorithm for deep belief nets. *Neural Computation*, 18(7):1527–1554, 2006.
- [57] D. Hobbs, G. Kresse, and J. Hafner. Fully unconstrained noncollinear magnetism within the projector augmented-wave method. *Physical Review B*, 62:11556–11570, 2000.
- [58] M. D. Hoffman and A. Gelman. The no-u-turn sampler: Adaptively setting path lengths in Hamiltonian Monte Carlo. *J. Mach. Learn. Res.*, 15(1):1593–1623, 2014.
- [59] P. Hohenberg and W. Kohn. Inhomogeneous electron gas. *Physical Review*, 136:B864–B871, 1964.
- [60] C. Holm and W. Janke. Critical exponents of the classical three-dimensional heisenberg model: A single-cluster monte carlo study. *Physical Review B*, 48:936–950, 1993.
- [61] J. Hubbard. Calculation of partition functions. *Physical Review Letters*, 3:77–78, 1959.



- [62] J. Hubbard. The magnetism of iron. *Physical Review B*, 19:2626–2636, 1979.
- [63] P. A. Igoshev, A. V. Efremov, A. I. Poteryaev, A. A. Katanin, and V. I. Anisimov. Magnetic fluctuations and effective magnetic moments in  $\gamma$ -iron due to electronic structure peculiarities. *Physical Review B*, 88:155120, 2013.
- [64] Y. Ikeda, A. Seko, A. Togo, and I. Tanaka. Phonon softening in paramagnetic bcc Fe and its relationship to the pressure-induced phase transition. *Physical Review B*, 90:134106, 2014.
- [65] R. O. Jones and O. Gunnarsson. The density functional formalism, its applications and prospects. *Rev. Mod. Phys.*, 61:689–746, 1989.
- [66] M. I. Katsnelson and A. I. Lichtenstein. First-principles calculations of magnetic interactions in correlated systems. *Physical Review B*, 61:8906–8912, 2000.
- [67] W. Kohn and L. J. Sham. Self-consistent equations including exchange and correlation effects. *Physical Review*, 140:A1133–A1138, 1965.
- [68] F. Körmann. *Magnetic systems studied by first-principles thermodynamics*. PhD thesis, Universität Paderborn, 2011.
- [69] F. Körmann, A. Dick, B. Grabowski, B. Hallstedt, T. Hickel, and J. Neugebauer. Free energy of bcc iron: Integrated ab initio derivation of vibrational, electronic, and magnetic contributions. *Physical Review B*, 78:033102, 2008.
- [70] F. Körmann, A. Dick, B. Grabowski, T. Hickel, and J. Neugebauer. Atomic forces at finite magnetic temperatures: Phonons in paramagnetic iron. *Physical Review B*, 85:125104, 2012.
- [71] F. Körmann, A. Dick, T. Hickel, and J. Neugebauer. Rescaled Monte Carlo approach for magnetic systems: Ab initio thermodynamics of bcc iron. *Physical Review B*, 81:134425, 2010.
- [72] F. Körmann, A. Dick, T. Hickel, and J. Neugebauer. Role of spin quantization in determining the thermodynamic properties of magnetic transition metals. *Physical Review B*, 83:165114, 2011.

- [73] F. Körmann, B. Grabowski, B. Dutta, T. Hickel, L. Mauger, B. Fultz, and J. Neugebauer. Temperature dependent magnon-phonon coupling in bcc Fe from theory and experiment. *Physical Review Letters*, 113:165503, 2014.
- [74] F. Körmann, T. Hickel, and J. Neugebauer. Influence of magnetic excitations on the phase stability of metals and steels. *Current Opinion in Solid State and Materials Science*, 20(2):77 – 84, 2016.
- [75] G. Kotliar, S. Y. Savrasov, K. Haule, V. S. Oudovenko, O. Parcollet, and C. A. Marianetti. Electronic structure calculations with dynamical mean-field theory. *Rev. Mod. Phys.*, 78:865–951, 2006.
- [76] M. Krech, A. Bunker, and D. P. Landau. Fast spin dynamics algorithms for classical spin systems. *Computer Physics Communications*, 111(1):1 – 13, 1998.
- [77] J. Kubler, K. H. Hock, J. Sticht, and A. R. Williams. Density functional theory of non-collinear magnetism. *Journal of Physics F: Metal Physics*, 18(3):469, 1988.
- [78] Ph. Kurz, F. Förster, L. Nordström, G. Bihlmayer, and S. Blügel. Ab initio treatment of noncollinear magnets with the full-potential linearized augmented plane wave method. *Physical Review B*, 69:024415, 2004.
- [79] Y. O. Kvashnin, R. Cardias, A. Szilva, I. Di Marco, M. I. Katsnelson, A. I. Lichtenstein, L. Nordström, A. B. Klautau, and O. Eriksson. Microscopic origin of Heisenberg and non-Heisenberg exchange interactions in ferromagnetic bcc Fe. *Physical Review Letters*, 116:217202, 2016.
- [80] D. Landau and K. Binder. *A Guide to Monte Carlo Simulations in Statistical Physics*. Cambridge University Press, New York, NY, USA, 2005.
- [81] I. Leonov, A. I. Poteryaev, V. I. Anisimov, and D. Vollhardt. Electronic correlations at the  $\alpha$ – $\gamma$  structural phase transition in paramagnetic iron. *Physical Review Letters*, 106:106405, 2011.
- [82] I. Leonov, A. I. Poteryaev, V. I. Anisimov, and D. Vollhardt. Calculated phonon spectra of paramagnetic iron at the  $\alpha$ - $\gamma$  phase transition. *Physical Review B*, 85:020401, 2012.

- [83] I. Leonov, A. I. Poteryaev, Yu. N. Gornostyrev, A. I. Lichtenstein, M. I. Katsnelson, V. I. Anisimov, and D. Vollhardt. Electronic correlations determine the phase stability of iron up to the melting temperature. *Scientific Reports*, 4, 2014.
- [84] A. I. Lichtenstein, M. I. Katsnelson, and G. Kotliar. Finite-temperature magnetism of transition metals: an ab initio dynamical mean-field theory. *Physical Review Letters*, 87:067205, 2001.
- [85] P. Ma and S. L. Dudarev. Langevin spin dynamics. *Physical Review B*, 83:134418, 2011.
- [86] P. Ma and S. L. Dudarev. Longitudinal magnetic fluctuations in langevin spin dynamics. *Physical Review B*, 86:054416, 2012.
- [87] P. Ma and S. L. Dudarev. Constrained density functional for noncollinear magnetism. *Physical Review B*, 91:054420, 2015.
- [88] P. Ma, S. L. Dudarev, and J. S. Wróbel. Dynamic simulation of structural phase transitions in magnetic iron. *Physical Review B*, 96:094418, 2017.
- [89] P. Ma, C. H. Woo, and S. L. Dudarev. Large-scale simulation of the spin-lattice dynamics in ferromagnetic iron. *Physical Review B*, 78:024434, 2008.
- [90] L. Mauger, M. S. Lucas, J. A. Muñoz, S. J. Tracy, M. Kresch, Y. Xiao, P. Chow, and B. Fultz. Nonharmonic phonons in  $\alpha$ -iron at high temperatures. *Physical Review B*, 90:064303, 2014.
- [91] R. I. McLachlan, K. Modin, and O. Verdier. Symplectic integrators for spin systems. *Physical Review E*, 89:061301, 2014.
- [92] M. Methfessel and A. T. Paxton. High-precision sampling for brillouin-zone integration in metals. *Physical Review B*, 40:3616–3621, 1989.
- [93] N. Metropolis, A. W. Rosenbluth, M. N. Rosenbluth, A. H. Teller, and E. Teller. Equation of state calculations by fast computing machines. *The Journal of Chemical Physics*, 21(6):1087–1092, 1953.
- [94] T. Moriya. *Spin fluctuations in itinerant electron magnetism*. Springer series in solid-state sciences. Springer-Verlag, 1985.

- [95] M. Mrovec, D. Nguyen-Manh, C. Elsässer, and P. Gumbsch. Magnetic bond-order potential for iron. *Physical Review Letters*, 106:246402, 2011.
- [96] S. Mukherjee and R.E. Cohen. Tight-binding based non-collinear spin model and magnetic correlations in iron. *Journal of Computer-Aided Materials Design*, 2001.
- [97] M. Müller, P. Erhart, and K. Albe. Analytic bond-order potential for bcc and fcc iron — comparison with established embedded-atom method potentials. *Journal of Physics: Condensed Matter*, 19(32):326220, 2007.
- [98] R. M. Neal. MCMC using Hamiltonian dynamics. In S. Brooks, A. Gelman, G. L. Jones, and X. Meng, editors, *Handbook of Markov Chain Monte Carlo*, chapter 5, pages 113–162. Chapman & Hall/CRC, 2011.
- [99] J. Neugebauer and T. Hickel. Density functional theory in materials science. *Wiley Interdisciplinary Reviews: Computational Molecular Science*, 3(5):438–448, 2013.
- [100] J. Neuhaus, M. Leitner, K. Nicolaus, W. Petry, B. Hennion, and A. Hiess. Role of vibrational entropy in the stabilization of the high-temperature phases of iron. *Physical Review B*, 89:184302, 2014.
- [101] I. P. Omelyan, I. M. Mryglod, and R. Folk. Algorithm for molecular dynamics simulations of spin liquids. *Physical Review Letters*, 86:898–901, 2001.
- [102] A. T. Paxton and M. W. Finnis. Magnetic tight binding and the iron-chromium enthalpy anomaly. *Physical Review B*, 77:024428, 2008.
- [103] P. Peczak and D. P. Landau. Monte Carlo study of critical relaxation in the 3d heisenberg model. *Journal of Applied Physics*, 67(9):5427–5429, 1990.
- [104] R. Peierls. On a minimum property of the free energy. *Physical Review*, 54:918–919, 1938.
- [105] J. E. Peralta, G. E. Scuseria, and M. J. Frisch. Noncollinear magnetism in density functional calculations. *Physical Review B*, 75:125119, 2007.

- [106] S. Prokhorenko, K. Kalke, Y. Nahas, and L. Bellaiche. Large scale hybrid Monte Carlo simulations for structure and property prediction. *npj Computational Materials*, 4(1):80, 2018.
- [107] C. X. Quintela, F. Rivadulla, and J. Rivas. Thermoelectric properties of stoichiometric and hole-doped crn. *Applied Physics Letters*, 94(15):152103, 2009.
- [108] S. Reich, J. Maultzsch, C. Thomsen, and P. Ordejón. Tight-binding description of graphene. *Physical Review B*, 66:035412, 2002.
- [109] V. Rosato, M. Guillope, and B. Legrand. Thermodynamical and structural properties of f.c.c. transition metals using a simple tight-binding model. *Philosophical Magazine A*, 59(2):321–336, 1989.
- [110] N. M. Rosengaard and B. Johansson. Finite-temperature study of itinerant ferromagnetism in Fe, Co, and Ni. *Physical Review B*, 55:14975–14986, 1997.
- [111] A. V. Ruban, S. Khmelevskiy, P. Mohn, and B. Johansson. Temperature-induced longitudinal spin fluctuations in Fe and Ni. *Physical Review B*, 75:054402, 2007.
- [112] A. V. Ruban and O. E. Peil. Impact of thermal atomic displacements on the curie temperature of 3d transition metals. *Physical Review B*, 97:174426, 2018.
- [113] O. F. Sankey and D. J. Niklewski. Ab initio multicenter tight-binding model for molecular-dynamics simulations and other applications in covalent systems. *Physical Review B*, 40:3979–3995, 1989.
- [114] A. Shapeev. Moment tensor potentials: A class of systematically improvable interatomic potentials. *Multiscale Model. Simul.*, 14(3):1153–1173, 2016.
- [115] P. A. Sharma, J. S. Ahn, N. Hur, S. Park, S. B. Kim, S. Lee, J.G. Park, S. Guha, and S. W. Cheong. Thermal conductivity of geometrically frustrated, ferroelectric YMnO<sub>3</sub>: Extraordinary spin-phonon interactions. *Physical Review Letters*, 93:177202, 2004.

- [116] J. C. Slater. The ferromagnetism of nickel. *Physical Review*, 49:537–545, 1936.
- [117] P. Souvatzis, O. Eriksson, M. I. Katsnelson, and S. P. Rudin. Entropy driven stabilization of energetically unstable crystal structures explained from first principles theory. *Physical Review Letters*, 100:095901, 2008.
- [118] J. B. Staunton, L. Szunyogh, A. Buruzs, B. L. Gyorffy, S. Ostanin, and L. Udvardi. Temperature dependence of magnetic anisotropy: An ab initio approach. *Physical Review B*, 74:144411, 2006.
- [119] P. Steneteg, B. Alling, and I. A. Abrikosov. Equation of state of paramagnetic CrN from ab initio molecular dynamics. *Physical Review B*, 85:144404, 2012.
- [120] I. Stockem, A. Bergman, A. Glensk, T. Hickel, F. Körmann, B. Grabowski, J. Neugebauer, and B. Alling. Anomalous phonon lifetime shortening in paramagnetic CrN caused by spin-lattice coupling: A combined spin and ab initio molecular dynamics study. *Physical Review Letters*, 121:125902, 2018.
- [121] G. M. Stocks, B. Ujfalussy, X. Wang, D. M. C. Nicholson, W. A. Shelton, Y. Wang, A. Canning, and B. L. Györffy. Towards a constrained local moment model for first principles spin dynamics. *Philosophical Magazine B*, 78(5-6):665–673, 1998.
- [122] R. L. Stratonovich. On a Method of Calculating Quantum Distribution Functions. *Soviet Physics Doklady*, 1957.
- [123] M. Suzuki. Static and dynamic finite-size scaling theory based on the renormalization group approach. *Progress of Theoretical Physics*, 58(4):1142–1150, 1977.
- [124] R. H. Swendsen and J. Wang. Nonuniversal critical dynamics in Monte Carlo simulations. *Physical Review Letters*, 58:86–88, 1987.
- [125] W. C. Swope, H. C. Andersen, P. H. Berens, and K. R. Wilson. A computer simulation method for the calculation of equilibrium constants for the formation of physical clusters of molecules: Application to small water clusters. *The Journal of Chemical Physics*, 76(1):637–649, 1982.

- [126] P. Tome, D. Logvinovich, J. Hejtmnek, M. H. Aguirre, and A. Weidenkaff. Magnetic influence on thermoelectric properties of  $\text{CrO}_{0.1}\text{N}_{0.9}$ . *Acta Materialia*, 59(3):1134 – 1140, 2011.
- [127] J. Tranchida, S. J. Plimpton, P. Thibaudeau, and A. P. Thompson. Massively parallel symplectic algorithm for coupled magnetic spin dynamics and molecular dynamics. *Journal of Computational Physics*, 372:406 – 425, 2018.
- [128] M. E. Tuckerman. *Statistical Mechanics: Theory and Molecular Simulation*. Oxford graduate texts. Oxford University Press, 2011.
- [129] B. Újfalussy, X. Wang, D. M. C. Nicholson, W. A. Shelton, G. M. Stocks, Y. Wang, and B. L. Gyorffy. Constrained density functional theory for first principles spin dynamics. *Journal of Applied Physics*, 85(8):4824–4826, 1999.
- [130] U. von Barth and L. Hedin. A local exchange-correlation potential for the spin polarized case. i. *Journal of Physics C: Solid State Physics*, 5(13):1629–1642, 1972.
- [131] F. Wang and D. P. Landau. Efficient, multiple-range random walk algorithm to calculate the density of states. *Physical Review Letters*, 86:2050–2053, 2001.
- [132] N. Wang, T. Hammerschmidt, J. Rogal, and R. Drautz. Accelerating spin-space sampling by auxiliary spin dynamics and temperature-dependent spin-cluster expansion. *Phys. Rev. B*, 99:094402, Mar 2019.
- [133] Z. Wang, S. Mohamed, and N. De Freitas. Adaptive Hamiltonian and Riemann manifold Monte Carlo samplers. In *Proceedings of the 30th International Conference on International Conference on Machine Learning - Volume 28*, ICML’13, pages III–1462–III–1470. JMLR.org, 2013.
- [134] A. Waske, B. Dutta, N. Teichert, B. Weise, N. Shayanfar, A. Becker, A. Hütten, and T. Hickel. Coupling phenomena in magnetocaloric materials. *Energy Technology*, 6(8):1429–1447, 2018.
- [135] U. Wolff. Collective Monte Carlo updating for spin systems. *Physical Review Letters*, 62:361–364, 1989.

- [136] A. D. B. Woods, B. N. Brockhouse, R. H. March, A. T. Stewart, and R. Bowers. Crystal dynamics of sodium at 90° K. *Physical Review*, 128:1112–1120, 1962.



# Curricula Vitae

**Name:** Ning Wang

**Gender:** Male

**Date of Birth:** 05/02/1990

**Place of Birth:** Shandong, China

**Nationality:** Chinese

**Email:** wangning2nwpu@gmail.com

## Education

- 2005 - 2008, Feicheng No. 1 High school, Shandong, China
- 2008 - 2011: the Honors College, Northwestern Polytechnical University, China
- 2011 - 2014: the School of Materials Science and Engineering, Northwestern Polytechnical University, China
- 2016 - 2019: the IMPRS-SurMat doctoral program, the Interdisciplinary Centre for Advanced Materials Simulation (ICAMS), Ruhr-Universität Bochum